TU Delft

Delft University of Technology

Collective dynamics and jamming in biological systems

van Drongelen, Ruben

DOI
10.4233/uuid:2748fa8b-8728-4931-8de1-2307322ef40c

Publication date
2018

Document Version
Final published version

Citation (APA)
van Drongelen, R. (2018). *Collective dynamics and jamming in biological systems*. [Dissertation (TU Delft), Delft University of Technology]. https://doi.org/10.4233/uuid:2748fa8b-8728-4931-8de1-2307322ef40c

Important note
To cite this publication, please use the final published version (if applicable).
Please check the document version above.

Copyright
Other than for strictly personal use, it is not permitted to download, forward or distribute the text or part of it, without the consent of the author(s) and/or copyright holder(s), unless the work is under an open content license such as Creative Commons.

Takedown policy
Please contact us and provide details if you believe this document breaches copyrights.
We will remove access to the work immediately and investigate your claim.

This work is downloaded from Delft University of Technology.
For technical reasons the number of authors shown on this cover page is limited to a maximum of 10.

Collective dynamics and jamming in biological systems

Collective dynamics and jamming in biological systems

Proefschrift

ter verkrijging van de graad van doctor
aan de Technische Universiteit Delft,
op gezag van de Rector Magnificus prof. ir. T.H.J.J. van der Hagen,
voorzitter van het College voor Promoties,
in het openbaar te verdedigen op maandag 2 juli 2018 om 15:00 uur

door

Ruben VAN DRONGELEN

Master of Science in Physics,
Universiteit Leiden, Nederland
geboren te Vlissingen, Nederland.

Dit proefschrift is goedgekeurd door de

promotor: prof. dr. A.M. Dogterom
copromotor: dr. T. Idema

Samenstelling promotiecommissie:

Rector Magnificus,	voorzitter
prof. dr. A.M. Dogterom,	Technische Universiteit Delft
dr. T. Idema,	Technische Universiteit Delft

Onafhankelijke leden:

Dr. S. Henkes	University of Aberdeen
Prof. dr. J. H. Snoeijer	Universiteit Twente
Prof. dr. R. H. H. G. van Roij	Universiteit Utrecht
Prof. dr. Y. M. Blanter	Technische Universiteit Delft
Dr. S. M. Depken	Technische Universiteit Delft

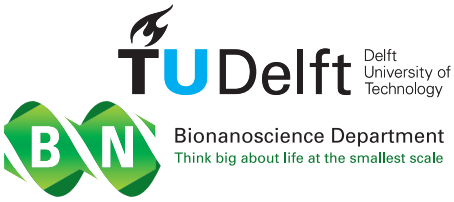

Keywords: collective dynamics; swarming; high density; jamming

Printed by: Gildeprint

Front & Back: 'Collective behaviour of toy penguins', photo by T. Idema

Copyright © 2018 by R. van Drongelen

Casimir PhD Series, Delft-Leiden 2018-28

ISBN 978-90-8593-354-0

An electronic version of this dissertation is available at
http://repository.tudelft.nl/.

Contents

1

Introduction

The whole is greater than the sum of its parts.

Aristotle

1.1. Collective behaviour in nature

One of the biggest challenges in physics is to describe living systems. Although living organisms have to abide by the laws of physics, generally, their behaviour is very different from ordinary lifeless matter. For example, organisms have the ability to move or to grow, whereas a lifeless object will not start moving without external influences. Organisms that can move often aggregate into colonies. We have all seen examples in nature of flocks of birds that fly and turn collectively, fish that swim in massive schools, and herds of mammals that migrate across the savannah. Not only these macroscopic animals move collectively, micro-organisms also aggregate to increase their chances of survival. Colonies of bacteria and slime moulds can consist of an enormous number of individuals. These colonies then behave collectively as if they were a single organism. Other examples of cells working together to benefit the collective are tissues. Cells in muscle tissue contract collectively to produce force. All of these systems are examples in the field of active matter, where the goal is to systematically describe the behaviour of large collections of active particles.

At first glance, the cells in a colony may appear to be similar to the molecules in a liquid. Both systems consist of a large number of constituents, and these constituents can flow in streams or vortices, but fundamentally these systems are different. The molecules' motion is of thermal origin, whereas the cells move by consuming chemical energy. This difference seems like a small detail, but the consumption of energy has large implications. As a consequence, energy is not conserved[1]. It is a

[1] Energy is not conserved on the level of the particle/individual. If we account for all the energetic processes happening inside the individual, energy will be conserved

1

violation of the first law of thermodynamics, and therefore we cannot describe the system macroscopically in the same way as thermal equilibrium systems. Thermal systems have the remarkable property that they can be described by a relatively small number of quantities, given that a complete description of a thermal system would require the positions and momenta of all particles in it. These thermodynamic properties, called the thermodynamic state variables, include for example: internal energy, entropy, temperature, pressure, volume. When the particles generate movement by consuming energy themselves, the thermodynamic relations between these state variables no longer hold and therefore, we cannot describe active systems with the theory of thermodynamics. At this time, a general theory of active matter does not exist.

Nature is full of captivating displays of collective phenomena. In figure 1.1, we show examples of collective behaviour in various environments, from micrometer-sized amoebae to elephants. We see a great diversity in behaviour of the groups. Even among the same species the group behaviour can be drastically different. For example fish can swim in ordered schools that migrate, but they can also form a vortex where the fish all swim in circles [1]. A similar transition has been observed in the social amoeba *Dictyostelium discoideum*. When the amoebae are starving, they aggregate into massive colonies on the order of 10^5 cells. The cells in such an aggregate crawl around a common centre [2]. The same aggregate can also migrate as if it is a single organism. The similarity in behaviour between otherwise unrelated systems like fish and amoebae raises some natural questions: are there general rules that apply to these systems? Can we divide all these living systems into a small number of classes? Can we define quantities similar to the thermodynamic state variables for a macroscopic description of the system? Another defining feature of these collectives is that the behaviour of the group is completely different from the behaviour of an individual in isolation. The whole is much more than just the sum of its parts. Can we quantify the benefits of aggregation? The non-linearity in these systems is the reason why we refer to them as complex systems. The emergent patterns in colonies are hard to predict from the interactions between individuals. So how do the individuals themselves know what to do when no individual actually has any idea what the group as a whole is doing? In other words, how are these groups managing themselves?

1.1.1. Modelling of active matter

In this thesis, I report my study on self-propelling particles systems using numerical methods, that is, computer simulations. With the computer simulations I realize particle systems. I use the data generated by the simulations to infer general principles and features of collective dynamics in organisms from a bottom up approach. The models in self-propelling particle studies are based simple and/or logical inter-

[1] Figure downloaded from https://commons.wikimedia.org/wiki/File:Elephant_herd_(5912064891).jpg
[2] Figure downloaded from https://pixabay.com/nl/goudvis-vis-vijver-huisdier-17944/
[3] Figure from Zitterbart et al. [3]
[4] Figure downloaded from https://de.wikipedia.org/wiki/Dictyostelium#/media/File:Dictyostelium_Late_Aggregation_1.JPG

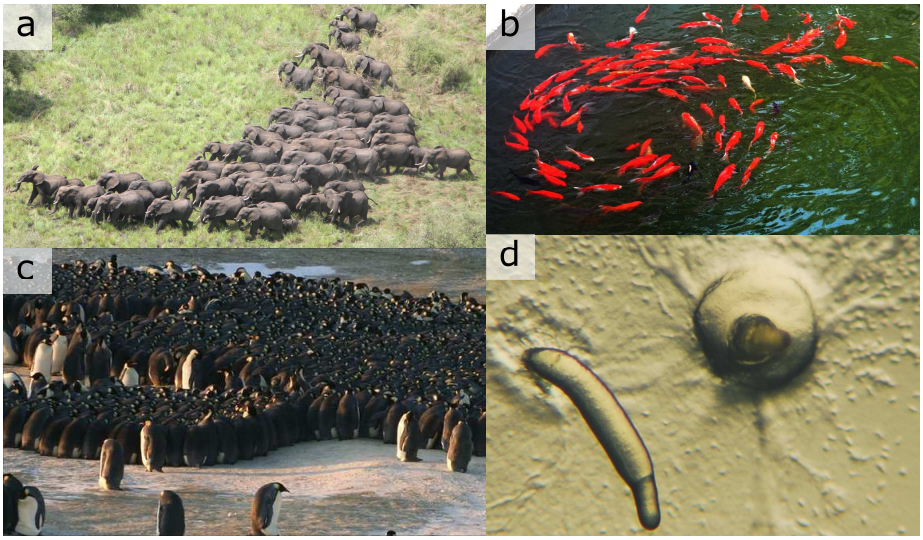

Figure 1.1: Various examples of collective behaviour in biological systems. a) Migrating herd of elephants[2]. b) School of fish swimming in circles[3]. c) Penguins huddling[4]. d) Two colonies of *Dictyostelium discoideum*, one migrating (left) and one rotating (right)[5].

actions between individuals. Generally, the group behaviour generated by each of these models is amazingly diverse. This diversity means these models are applicable to multiple biological systems and it is also an indication that behind different types of collective behaviour, the interactions between individuals might have the same origin.

Two pioneers in modelling collective dynamics are Reynolds [4], who simulated boids and Vicsek et al. [5], after whom the famous Vicsek model is named. The Vicsek model considers self-propelling agents with biologically motivated interactions in a square box with double periodic boundary conditions. The agents are point-like, so they cannot collide. Instead, they interact by aligning locally. An individual finds the orientation of all other agents within a cut-off distance and aligns with those. On top of the alignment, there is a noise term that prevents perfect alignment. The interactions in the Vicsek model produce groups that move coherently, groups in which all individuals move randomly with little correlation, and groups in which the individuals move in circles around a common centre, depending on the number density and the magnitude of orientational noise. The diversity in group behaviour is impressive for such a minimal model and therefore it became popular among physicists. Researchers developed many extensions of the original model for specific systems or added interactions for an even wider range of collective behaviour. Notable articles are Grégoire and Chaté [6], who added cohesion between individuals, Couzin et al. [7], who studied the effect of an attractive potential, Chaté et al. [8], who discuss the effect of polarity of the individuals and the fluid the particles are immersed in, and Henkes et al. [9], who studied finite sized particles in a confined

area. In this thesis, we focus on finite sized particles with short-range interactions only, and no confinement. We will find a wide variety of collective behaviour in very crowded environments and explore the limits of how crowded it can get before colonies start running into problems. I will explain what these problems are and what their physical origin is in more detail in the section about high-density physics (section 1.1.2).

Before diving into the high-density physics, I want to discuss what order parameters are and how researchers use these parameters to quantify the systems they try to model. We need an objective way to characterize many-particle systems. Probably the most famous and also one of the simplest example of a many-particle systems is the Ising model. The Ising model is a mathematical model usually applied in the context of magnetic dipoles of atoms. These atoms, and in fact every elementary particle, have an intrinsic property called 'spin' and particles with a non-zero spin have a magnetic moment associated with them. In the traditional 2D Ising model, the atoms are arranged in a square lattice and they either point up (spin up) or down (spin down). In figure 1.2b I show the magnetisation and the atoms' corresponding configurations in the Ising model. The inset on the left has the spins all pointing up, and therefore, the object is strongly magnetic. However, when spins randomly point up or down, like in the inset on the right-hand side, the spins tend to cancel each other and the magnetisation will be low. So one way to characterise this system is by the mean magnetisation, which is simply the fraction of spins down, subtracted from the fraction of spins up. The resulting number expresses the order within the system without specifying the orientation of every single spin in it. Order parameters are used for distinguishing systems with macroscopically different properties. In the case of the Ising model, a mean magnetisation of zero means the object is not magnetic, and a non-zero magnetisation means the object is magnetic. The point where order parameters change from a non-zero value to zero is typically associated with a phase transition, i.e. a transition between a magnetic phase and non-magnetic phase in the previous example. The density is also an example of an order parameter. It distinguishes ice from, liquid water and water vapour even though these consist of the same molecules. The density as an order parameter behaves differently from the mean magnetisation and the Vicsek order parameter which we will use. I will discuss this difference in section 1.1.2.

In the Vicsek model, instead of just pointing up or down, the particles have a self-propulsion direction, which can point in any direction in the plane. Generalising the order parameter for this case is fairly straightforward. We simply take the absolute value of the sum of all the vectors and normalise by the number of particles. The Vicsek order parameter, ϕ, is then given by

$$\phi = \frac{1}{N}\left|\sum_{i=1}^{N}\hat{\psi}_i\right|, \tag{1.1}$$

for a system of N particles, where the orientation of a particle i is the unit vector $\hat{\psi}_i$. A highly ordered group of particles has an order parameter close to one. In the ordered state, the group of particles has a preferred direction to move in, i.e. symmetry is broken. A high order parameter therefore indicates migration. A low order

parameter means that the group of particles is stationary. Quite often, one needs to measure multiple order parameters to fully classify a system. For example, the Vicsek order parameter does not distinguish between a system of random orientations and the vortex state even though they are obviously very different. To distinguish between these two states, we could measure the vorticity or angular momentum. In this thesis, we mainly use the Vicsek order parameter.

1.1.2. High density physics

Besides active matter, a second field in physics that concerns itself with many-particle systems is the field of granular materials. The difference with thermal systems is that thermal motion of the particles in granular materials is negligible. Familiar examples of such systems are grains of sand, rice or rocks on a steep slope of a mountain. Depending on the situation, these systems exhibit liquid or solid behaviour. To illustrate these properties, consider the salt in a salt shaker. If we turn it upside-down, initially maybe a little bit of salt will flow out, but the majority will be stuck. Although the grains are smaller than the holes of the shaker, they are not flowing out. The absence of flow is a property of a solid, while a liquid would flow through the holes easily. Of course, the salt is supposed to flow out. As its name implies, we need to shake the shaker for that to happen. Now the salt is flowing, which is a property of liquids. For the salt shaker, the shaking is quite a dramatic external influence. However, even small distortions may cause a transition from a stationary, solid state to a liquid state. Rock slides and avalanches are examples of systems that can be triggered to flow by a relatively small distortion.

The solid state in granular systems is called the jammed phase and the transition between the jammed phase and the flowing phase is known as the jamming transition. Phase transitions mark a sudden change of the properties of a system. The phase transition we are all familiar with is the melting of ice into water, or evaporating water into water vapour. In all three phases the water molecules are the same, but their arrangement is different. The different ordering of the molecules makes that ice, water and vapour have different densities. As long as the temperature is between 0°C and 100°C (at atmospheric pressure), water will have a density of roughly 1000 kg/m^3. When the temperature drops below the freezing point, its density changes discontinuously to about 917 kg/m^3 (see figure 1.2a). Transitions with discontinuities associated to them are first order phase transitions. The Ising model discussed before also has a phase transition. In the Ising model neighbouring spins align, because this is energetically favourable. The state with the lowest energy would be when all spins point in the same direction. Thermal energy however introduces noise such that spins sometimes spontaneously flip and point in the wrong direction. It turns out that the order parameter in the Ising model changes continuously from the ordered phase (non-zero mean magnetisation) to the disordered phase (vanishing mean magnetisation) with increasing temperature (see figure 1.2b). Interestingly, completely different systems can be described by the same equations. For example, the Ising model can represent magnetic spins, as well as a gas on a lattice. For the latter, a ‘spin up’ translates to the presence of a particle and a ‘spin down’ translates to the absence of a particle. When different

1

physical systems can be described by the same equations and identical parameters like critical exponents, they are said to be part of the same universality class. The analysis of phase transitions and an order parameter are therefore extremely useful tools for classifying systems into universality classes.

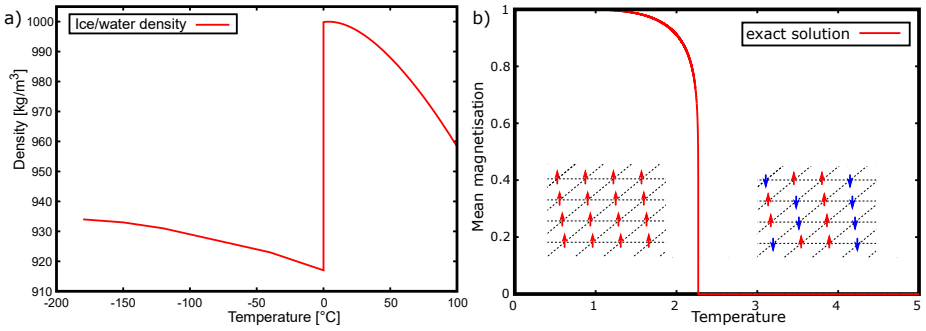

Figure 1.2: Two different types of phase transitions. a) The density changes discontinuously with temperature at the critical temperature $T = 0°C$ [5]. This is a first-order phase transition. b) The mean magnetization in the Ising model decreases continuously until it vanishes at the critical temperature. The phase transition in the Ising model is of second order. The insets show two (parts of) realisations of the system with blue arrows representing down and red arrows representing spin up.

Granular soft materials gained a lot of interest over the last two decades due to the existence of an unknown type of phase transition. When gradually increasing the density in a granular medium, the medium changes from liquid-like to solid-like. For frictionless spherical particles, this transition occurs at more or less the same critical density, called point J. In three dimensions, point J corresponds to a density of $\phi_J \approx 0.64$, and in two dimensions we have $\phi_J \approx 0.84$. Density is not the only factor determining the state of the system. The state also depends on internal motion due to temperature, and external forces. In 1998, Liu and Nagel [10] were the first to sketch a qualitative phase diagram of jammed and unjammed states and the transitions between them (see figure 1.3a). Point J discussed above is located on the density axis. This sketch implies that there are two additional ways to transition between the jammed and unjammed state. Systems at high temperature are more resilient to jamming due to the internal vibrations. Furthermore, externally applying forces to the system can cause the particles to flow at densities where it would normally be jammed. Three years after the introduction of the sketch in figure 1.3a, Van Trappe et al. [11] showed that the shape of the different jamming-unjamming transitions is actually convex (figure 1.3b. Since then, many have investigated granular phase transitions by looking into the effects of density [12, 13], temperature [14], and shear forces [15, 16] on packings of granular particles, but the exact nature of the transitions along each of the axes in figure 1.3 is still up for debate. The jamming transition was also found in confluent tissues in both experiments [17], and

[5] Data obtained from https://commons.wikimedia.org/wiki/File:Density_of_ice_and_water_(en).svg

simulations [18, 19], where a tissue was modelled as as a Voronoi tessellation.

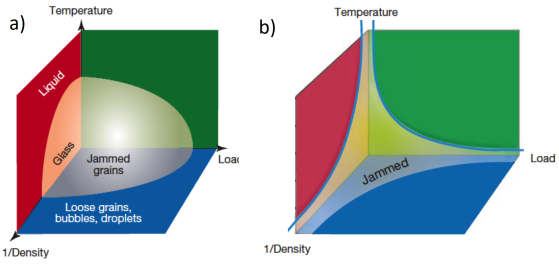

Figure 1.3: Sketches of the three dimensional phase diagram from (a) Liu and Nagel [10] and (b) Van Trappe et al. [11]. From a jammed state, systems can unjam by moving along the density axis, temperature axis, or load axis.

Dense active systems, like granular materials, also often consist of roughly identical individuals or particles and therefore combining models from both fields is a logical step. As an example of self-propelling, almost identical agents, we consider a colony of emperor penguins. The Antarctic is a hostile environment with temperatures dropping to below -60°C and strong winds. To survive, the penguins form a tight colony to preserve their heat as much as possible. With coordinated movements, they take turns being on the outside [3]. Without rearrangements, penguins on the outside would still freeze to death, and ironically, penguins in the middle would overheat. In general, organisms find benefits in aggregates. At the same time though, they cannot form overly tight aggregates because colonies need to be dynamic to survive. Models combining aspects from both granular physics and active matter therefore show an interesting interplay between jamming at high density and dynamics due to activity. There are many possible combinations to combine active and dense matter. For example one could consider finite size self-propelled particles without alignment [20–23], or alignment with the instantaneous velocity [9, 24], or alignment with nearest neighbours [25], or even a combination of Vicsek alignment and velocity alignment [26]. In this thesis I will mainly focus on the alignment interactions from the Vicsek model and the finite size effects of soft circular particles.

1.1.3. Over-damped environment

Our goal is to develop a general model that can describe collective behaviour from the bottom up, where we assume simple rules between neighbours for individual behaviour. Our main focus however, will be the collective dynamics on small scales, like cells in tissues or unicellular organisms on a substrate. Physics on these small scales works a little bit different than we are used to at our scales. Let us consider a large boat navigating on the water. When the boat stops propelling itself, it will very slowly come to a halt. The boat's inertia will carry it, possibly even for tens of kilometres. In terms of equations we can write

$$m\vec{a} = -\vec{F}_{\text{drag}}. \tag{1.2}$$

The left-hand side, depending on the mass m and acceleration $\vec{a}$, is the inertial term. The right-hand side is the drag force. For a spherical particle of radius R in a fluid of viscosity η, the drag force is given by $\vec{F}_{\text{drag}} = 6\pi\eta R\vec{v}$, where $\vec{v}$ is the velocity of the

particle. Loaded ships have a very large mass, and therefore their acceleration (or rather deceleration) is small. The situation is completely different for small particles moving through water. Their mass is relatively small and so their acceleration is enormous. When bacteria stop swimming they come to an instantaneous halt. The ship and the bacteria move in the same water with the same viscosity, but for the large object the water has little effect, and for the small object the water feels like honey. This difference can be captured by a dimensionless number, the Reynolds number.

The Reynolds number, Re, is the ratio between the inertial force and viscous drag force. From the Navier-Stokes equations, one can derive that the Reynolds number is given by $\mathrm{Re} = \rho v R/\eta$, where ρ is the density of the displaced fluid, and R and v the characteristic size and speed of the particle. Then, for a particle subjected to body forces, the equation of motion is

$$m\vec{a} = -\vec{F}_{\mathrm{drag}} + \vec{F}_{\mathrm{body}}. \tag{1.3}$$

When $\mathrm{Re} << 1$, inertial forces are insignificant in the equation of motion. Where container ships ($\mathrm{Re} \sim 10^8$) require many kilometres to stop, a swimming bacterium ($\mathrm{Re} \sim 10^{-5}$) stops immediately when it stops propelling itself. When we consider collective behaviour at low Reynolds number, the inertial term on the left-hand side can be neglected and we can rewrite equation 1.3 to

$$\begin{aligned} \vec{F}_{\mathrm{drag}} &= \vec{F}_{\mathrm{body}} \\ \vec{v} &= \frac{1}{6\pi\eta R}\vec{F}_{\mathrm{body}} \qquad (3D). \end{aligned} \tag{1.4}$$

In this thesis we will consider objects in two dimensions, in which case the numerical factor of the drag force changes. The equations of motion that we will use are expressions from Landau and Lifshitz [27]:

$$\vec{v} = \frac{3}{32\pi\eta R}\vec{F}_{\mathrm{body}} \qquad (2D). \tag{1.5}$$

For its rotational counterpart we use

$$T = 4\pi\eta_R R^2 \omega, \tag{1.6}$$

$$\omega = \frac{1}{4\pi\eta_R R^2} T \tag{1.7}$$

where T is the net torque on the object of size R, η_R is the rotational viscosity of the fluid, and ω is the rotational velocity of the object.

In chapter 2 we will find very diverse behaviour by combining the main ideas from the Vicsek model with the finite size effect of circular particles. The model consists of self-propelled particles that align when they are close to each other. In chapter 3 we explore our system of self-propelled particles from the side of granular materials, i.e. we study questions like: Under which conditions colonies jam, and which conditions are necessary to unjam? Next, we will try to make the model more

physical by eliminating the Vicsek alignment interaction. Originally being applied to flocks of birds, the alignment rule is somewhat artificial. Birds have the ability to look at each other and may decide to fly in the same direction as their neighbours. On the small scales we are considering, this alignment rule may not be very realistic. Hence, in chapter 4 we investigate whether alignment is possible through mechanical interactions. We will show that elliptical particles align by bumping into each other. Chapter 5 is my first attempt to find the jamming-unjamming transition for circular, self-propelled, particles with the Vicsek alignment term. Analogous to studies of passive matter, we use a computational method composed of shearing our system of active particles to probe properties like elasticity and viscosity. Unfortunately, unexpected properties of self-propelled particles did not allow us to construct the jamming-unjamming phase diagram. Finally, chapter 6 is a bit unrelated to the previous chapters. We show that the patterns and shapes of cells in insect embryos can be explained by our model that consists of only simple mechanical interactions between cells and their membranes.

References

[1] D. S. Calovi, U. Lopez, S. Ngo, C. Sire, H. Chaté, and G. Theraulaz, *Swarming, schooling, milling: phase diagram of a data-driven fish school model,* New J. Phys. **16**, 015026 (2014).

[2] W.-J. Rappel, A. Nicol, A. Sarkissian, H. Levine, and W. F. Loomis, *Self-organized Vortex State in Two-Dimensional Dictyostelium Dynamics,* Phys. Rev. Lett. **83**, 1247 (1999).

[3] D. P. Zitterbart, B. Wienecke, J. P. Butler, and B. Fabry, *Coordinated movements prevent jamming in an Emperor penguin huddle.* PloS one **6**, e20260 (2011).

[4] C. W. Reynolds, *Flocks, herds and schools: A distributed behavioral model,* ACM SIGGRAPH Computer Graphics **21**, 25 (1987).

[5] T. Vicsek, A. Czirók, E. Ben-Jacob, I. Cohen, and O. Shochet, *Novel type of phase transition in a system of self-driven particles,* Phys. Rev. Lett. **75**, 1226 (1995).

[6] G. Grégoire, H. Chaté, and Y. Tu, *Moving and staying together without a leader,* Phys. D **181**, 157 (2003).

[7] I. Couzin, J. Krause, N. Franks, and S. Levin, *Effective leadership and decision-making in animal groups on the move,* Nature **433 (7025)**, 513 (2005), publisher: Nature Publishing Group.

[8] H. Chaté, F. Ginelli, G. Grégoire, F. Peruani, and F. Raynaud, *Modeling collective motion: variations on the Vicsek model,* Eur. Phys. J. B **64**, 451 (2008).

[9] S. Henkes, Y. Fily, and M. C. Marchetti, *Active jamming: Self-propelled soft particles at high density,* Phys. Rev. E **84**, 040301 (2011).

[10] A. J. Liu and S. R. Nagel, *Nonlinear dynamics: Jamming is not just cool any more,* Nature **396**, 21 (1998).

[11] V. Trappe, V. Prasad, L. Cipelletti, P. N. Segre, and D. A. Weitz, *Jamming phase diagram for attractive particles,* Nature **411**, 772 (2001).

[12] C. S. O'Hern, S. A. Langer, A. J. Liu, and S. R. Nagel, *Random packings of frictionless particles,* Phys. Rev. Lett. **88**, 075507 (2002).

[13] D. S. Bolintineanu, G. S. Grest, J. B. Lechman, and L. E. Silbert, *Diffusion in jammed particle packs,* Phys. Rev. Lett. **115**, 088002 (2015).

[14] Z. Zhang, N. Xu, D. T. N. Chen, P. Yunker, A. M. Alsayed, K. B. Aptowicz, P. Habdas, A. J. Liu, S. R. Nagel, and A. G. Yodh, *Thermal vestige of the zero-temperature jamming transition,* Nature **459**, 230 (2009).

[15] B. P. Tighe, E. Woldhuis, J. J. C. Remmers, W. van Saarloos, and M. van Hecke, *Model for the scaling of stresses and fluctuations in flows near jamming,* Phys. Rev. Lett **105**, 088303 (2010).

[16] D. Vågberg, P. Olsson, and S. Teitel, *Universality of jamming criticality in overdamped shear-driven frictionless disks,* Phys. Rev. Lett. **113**, 148002 (2014).

[17] T. E. Angelini, E. Hannezo, X. Trepat, M. Marquez, J. J. Fredberg, and D. A. Weitz, *Glass-like dynamics of collective cell migration,* Proc. Natl. Acad. Sci. U. S. A. **108**, 4714 (2011).

[18] D. Bi, J. H. Lopez, J. M. Schwarz, and M. L. Manning, *A density-independent rigidity transition in biological tissues,* Nat. Phys. **11**, 1074 (2015).

[19] D. Bi, X. Yang, M. C. Marchetti, and M. L. Manning, *Motility-driven glass and jamming transitions in biological tissues,* Phys. Rev. X **6**, 021011 (2016).

[20] Y. Fily, S. Henkes, and M. C. Marchetti, *Freezing and phase separation of self-propelled disks,* Soft Matter **10**, 2132 (2014).

[21] A. Wysocki, R. G. Winkler, and G. Gompper, *Cooperative motion of active brownian spheres in three-dimensional dense suspensions,* EuroPhys. Lett. **105**, 48004 (2014).

[22] E. Flenner, G. Szamel, and L. Berthier, *The nonequilibrium glassy dynamics of self-propelled particles,* Soft Matter **12**, 7136 (2016).

[23] J. Bialké, T. Speck, and H. Löwen, *Crystallization in a dense suspension of self-propelled particles,* Phys. Rev. Lett. **108**, 168301 (2012).

[24] R. Sknepnek and S. Henkes, *Active swarms on a sphere,* Phys. Rev. E **91**, 022306 (2015).

[25] R. van Drongelen, A. Pal, C. P. Goodrich, and T. Idema, *Collective dynamics of soft active particles,* Phys. Rev. E **91**, 032706 (2015).

[26] C. A. Weber, C. Bock, and E. Frey, *Defect-mediated phase transitions in active soft matter,* Phys. Rev. Lett. **112**, 168301 (2014).

[27] L. D. Landau and E. M. Lifshitz, *Fluid Mechanics* (Butterworth-Heinemann, Oxford, 1987).

2

Collective dynamics of soft active particles

Those who know, do.
Those who understand, teach.

Aristotle

We present a model of soft active particles that leads to a rich variety of collective behaviour found also in dense biological swarms of bacteria and other unicellular organisms. Our model uses only local interactions, such as Vicsek-type nearest neighbour alignment, short-range repulsion, and a local boundary term. Changing the relative strength of these interactions leads to migrating swarms, rotating swarms and jammed swarms, as well as swarms that exhibit run-and-tumble motion, alternating between migration and either rotating or jammed states. Interestingly, although a migrating swarm moves slower than an individual particle, the diffusion constant can be up to three orders of magnitude larger, suggesting that collective motion can be highly advantageous, for example, when searching for food.

This chapter has been published as R. van Drongelen, A. Pal, C. P. Goodrich, and T. Idema, Phys. Rev. E **91**, 032706 (2015).

1. Introduction

Collective migration is found throughout the living world. Examples range from shoals of fish and flocks of birds on the macroscopic level [1, 2] to microswimmers and individual cells at the micron scale [3–6]. At even smaller scales within the cell, myosin motors work collectively on actin filaments to achieve long-range alignment [7]. In such crowded environments, the simple behaviour of individuals results in complex, non-trivial dynamics of the group. No individual group member can dictate the collective group behaviour or even have anything close to complete information of the group's dynamics. Nonetheless, the emergent collective patterns have a huge impact on the individuals, and they often depend on them for their very survival. Therefore it is an obvious question to ask how the rules governing the behaviour of each individual relate to the resulting collective behaviour of the group.

In their seminal 1995 paper, Vicsek et al. [8] introduced a model for studying flock behaviour based on a few simple rules for each individual bird. In their model, the individuals are described as oriented point particles, which exhibit self-propulsion, nearest-neighbour interactions that result in particle alignment, and noise. Many variants of the original model have been studied in the last twenty years [9]. Parallel to the development of the Vicsek model, much progress has also been made in the field of granular media, which studies the collective behaviour of collections of large particles. In their famous 1998 Nature news and views, Liu and Nagel proposed that the observed behaviour of these systems can be summarized in a phase diagram. Systems will get jammed at high densities provided both their effective temperature and the applied load are low enough, with a sharp phase transition between the jammed and unjammed state [10].

In recent years, several groups have started combining ideas from both fields, studying the collective behaviour of finite-sized self-propelled particles. In their 2011 paper, Henkes et al. [11] showed that for a confined system, with low self-propulsion velocities (equivalent to low load and temperature), a sharp transition can also be found between a liquid and a solid state as a function of packing density. Models without confinement often use a long-range attraction to model collective dynamics. For example Grégoire et al. [4] and Mognetti et al. [12] combined the Vicsek model with a Lennard-Jones-like potential and found that this long-range attraction result in cohesive flocks. d'Orsogna et al. [13] and Nguyen et al. [14] mapped the phase space for swarms held together by a long-range Morse potential for two and three dimensions respectively. However, Rappel et al. [6] found that a long-range interaction is not a requirement for self-organization, neither in their simulations, nor in experiments (see also Wang and Kuspa [15]).

In this chapter we describe the results of our study of the collective dynamics of soft, finite sized, active particles with short-range orientational interactions, but without confinement. With no extra rules such a system would quickly fall apart. To prevent this from happening, we add a local boundary term to the model. This term directs particles at the boundary towards the cluster (i.e., particles want to move into the cluster, where the environment is usually more friendly). The density of our cluster is therefore not set by us as an adjustable parameter, but by the

system resulting from a balance between its effective surface tension and the bulk modulus of the cluster. We find that our system exhibits a range of different types of behaviour, depending on cluster size, the particles' self-propulsion speed, and the strength of the nearest-neighbour alignment term. The two dominant types of behaviour we find are collective migration and the formation of a rotational cluster with no net movement. Both are also frequently found throughout the living world. Famous examples of migrating systems are herds of mammals and aggregates of slime molds, while rotating clusters are well-known in schools of fish and the spiral of death formed by army ants. In fact, most of these systems display both types of behaviour, e.g. fish switch between migration and rotation (milling) [2, 16], and depending on environmental conditions slime molds [6, 17, 18] and bacteria [19–21] will migrate or rotate. For example the slime mold *Dictyostelium Discoideum* (or Dicty) will collectively migrate if food is scarce, and transitions to a vortex to form a fruiting body as a last resort [22]. Individuals in dense, biological swarms often cannot judge the volume of the swarm, but only observe their local environment. Therefore, we consider the local interaction rules we use in this work to be more realistic for describing the rules that individuals in actual swarms follow than models with long-range interactions.

2. Method

2.1. Local interaction model

We study the behaviour of a two-dimensional system of self-propelling, soft, circular particles on an infinite sheet. In particular, we focus on the effects of the number of particles, the self-propulsion force and the torque that aligns the particles with each other. To prevent crystallization, the particles have different radii, drawn from a rather narrow Gaussian distribution, $G(\mu = \bar{a}, \sigma = \bar{a}/10)$, such that $\bar{a}$ is the average particle radius. The particles interact only locally. All of them experience repulsive forces when overlapping (Hookian repulsion) and Vicsek-type alignment interactions that tend to rotate their orientation to the average of that of their neighbours. Additionally, particles that are on the boundary of a particle cluster push inward, resulting in the formation of a tightly packed disordered cluster. The slight polydispersity of particle diameters, and fluctuations in the strength and direction that each particle pushes in, will lead to rearrangements and eventually large scale motion.

We apply this model to densely packed biological systems in the limit of vanishing Reynolds number. We are therefore in the regime of over-damped motion, which means that inertia is unimportant. The equations of motion for a disk in such a highly viscous fluid are given by [23]:

$$\vec{F}_i = \frac{32}{3}\eta a_i \vec{v}_i \quad \equiv \alpha_i \zeta \vec{v}_i \tag{2.1}$$

and

$$T_i = 4\pi\eta_R a_i^2 \omega_i \equiv \alpha_i^2 \chi \omega_i, \tag{2.2}$$

with $\vec{F}_i$ and T_i the net force and torque acting on particle i, a_i the particle radius, and $\alpha_i = a_i/\bar{a}$ the normalized radius. The effective translational and rotational viscosity are η and η_R, respectively, and $\vec{v}_i$ and ω_i are the linear and angular velocity of the particle. To simplify our expressions, we define the rescaled viscosities $\zeta = (32/3)\eta\bar{a}$ and $\chi = 4\pi\eta_R\bar{a}^2$.

We denote the position of particle i by $\vec{x}_i$ and its orientation by $\hat{\psi}_i$. Particles are considered neighbours for the purpose of the orientation interaction if their centres are less than $2.7\bar{a}$ apart. With this cut-off distance, two touching particles with radius $a_i = 1.3\bar{a}$ will still be considered neighbours, but two small particles ($a_i = 0.7\bar{a}$) separated by a third small particle will not. Because the spread in the radius is $\sigma = \bar{a}/10$, the probability of finding even larger or smaller particles together is negligible.

Instead of an attraction or geometrical confinement, our model uses a local boundary term to prevent systems from falling apart. An individual looks at the positions of its neighbours to determine its position within the cluster. If particle i has no neighbours over an angle $\theta_{\text{out},i} \geq \pi$ we consider it to be on the boundary of the cluster and it exerts an additional torque and force (see figure 2.1 for relevant quantities). Particles with only one or two neighbours automatically satisfy this criterion. Let $\mathcal{N}_i$ denote the set of neighbours of particle i. The net force and torque on the particle are then given by

$$\begin{aligned}\vec{F}_i &= \vec{F}_{i,\text{self-propulsion}} + \vec{F}_{i,\text{boundary}} + \vec{F}_{i,\text{repulsion}} \\ &= \left[F_{\text{self}} + (\theta_{\text{out},i} - \pi)\, F_{\text{in}}\Theta(\theta_{\text{out},i} - \pi)\right]\hat{\psi}_i - k\sum_{j\in\mathcal{N}_i}\vec{d}_{ij}, \qquad (2.3)\end{aligned}$$

$$\begin{aligned}T_i &= T_{i,\text{boundary}} + T_{i,\text{noise}} + T_{i,\text{align}} \\ &= T_{\text{in}}\Delta\theta_i \cdot \Theta(\theta_{\text{out},i} - \pi) + T_{\text{noise}}\xi_i + \frac{T_{\text{align}}}{|\mathcal{N}_i|}\sum_{j\in\mathcal{N}_i}\Delta\psi_{ij}, \qquad (2.4)\end{aligned}$$

where $\Theta(\theta)$ is the Heaviside step function. In equation (2.3), the first two terms of the force are the self-propulsion and the boundary force, which act in the direction of orientation $\hat{\psi}_i$. The strength of these interactions is set by F_{self} and F_{in} respectively. The last force term is the repulsion between overlapping particles i and j, where the amount of overlap is given by $|\vec{d}_{ij}|$ (which of course is zero for non-overlapping particles). The strength of the repulsion force is set by the spring constant k. The first term of the torque in equation (2.4) turns particles on the boundary inwards. The torque is proportional to a parameter T_{in} times the angle between the orientation $\hat{\psi}_i$ and the exterior bisector of $\theta_{\text{out},i}$. The second term is responsible for the orientational noise a particle experiences. We pick ξ_i randomly from $\{-1, 1\}$ each timestep creating a torque of magnitude T_{noise}. The final term of the torque aligns particles to the average orientation of their neighbours, where T_{align} is the interaction strength, $|\mathcal{N}_i|$ is the number of neighbours, and $\Delta\psi_{ij}$ is the mismatch in orientation between particles i and j. The alignment is the only interaction which acts between particles (apart from the passive repulsion) and is therefore ultimately responsible for collectivity in Vicsek-type models. Note that, in analogy with the Vicsek model, we only include noise on the torque and not on

the force. With this noise term, the motion of a single particle becomes a random walk; a single noise term is thus sufficient to introduce an element of randomness in each particle's motion, and additional noise terms do not qualitatively change our results. Eliminating the noise on the torque (and hence the orientations) on the other hand does have a strong effect, as this noise term is required to obtain the rich behaviour we observe.

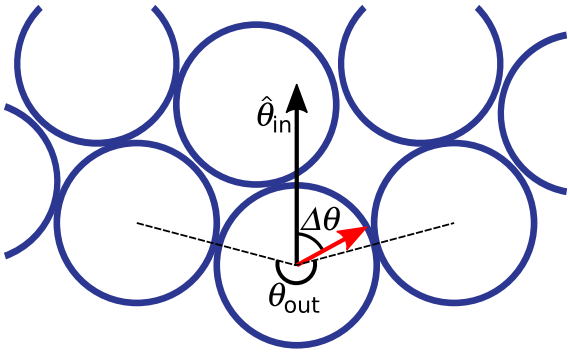

Figure 2.1: Visualisation of the boundary rule. The particle at the bottom finds no neighbours over an angle $\theta_{\text{out}} > \pi$. It therefore exerts a torque in order to align its orientation $\hat{\psi}_i$ (short arrow) to the exterior bisector of θ_{out}, which is denoted $\hat{\theta}_{\text{in}}$ (long arrow). The torque it exerts scales linearly with $\Delta\theta$, the angle between these two vectors. Simultaneously, the particle exerts an additional force in the direction of orientation, proportional to $\theta_{\text{out}} - \pi$.

2.2. Simulations

To characterize the behaviour of our system, we introduce dimensionless scaling parameters that represent the strengths of the various interactions. We define $\tau = \zeta/k$ as the characteristic timescale for two overlapping particles to separate due to their repulsive interaction. For any other interaction X we define a scaling parameter $\lambda_X = \tau/\tau_X$, where τ_X is the characteristic timescale of interaction X. The characteristic timescales and scaling parameters for all interactions in our model system are given in Table 2.1.

Interaction	Timescale	Dimensionless scaling parameter
Repulsion	$\tau = \zeta/k$	-
Alignment	$\tau_{\text{align}} = \chi/T_{\text{align}}$	$\lambda_a = \zeta T_{\text{align}}/k\chi$
Noise	$\tau_{\text{noise}} = 2\chi^2/T^2_{\text{noise}}\Delta t$	$\lambda_n = \zeta T^2_{\text{noise}}\Delta t/2k\chi^2$
Inward force	$\tau_{F_{\text{in}}} = \zeta\bar{a}/F_{\text{in}}$	$\lambda_{F_{\text{in}}} = F_{\text{in}}/k\bar{a}$
Inward torque	$\tau_{T_{\text{in}}} = \chi/T_{\text{in}}$	$\lambda_{T_{\text{in}}} = \zeta T_{\text{in}}/k\chi$
Active force / Self-propulsion	-	$\lambda_s = F_{\text{self}}/k\bar{a}$

Table 2.1: List of characteristic timescales and scaling parameters for all interactions in our simulations. For the inward force, we used the approximation that $2\arctan\left(\frac{x}{2\bar{a}}\right) \approx \frac{x}{\bar{a}}$. Since self-propulsion is an active process, it does not have a characteristic relaxation timescale.

In Table 2.1 we denote the duration of one simulation step by Δt. The self-propulsion has no characteristic timescale as it corresponds to an external rather than a restoring force. To arrive at a dimensionless parameter describing the

strength of the self-propulsion, we define $\lambda_s \equiv F_{\text{self}}/(k\bar{a})$, in analogy with the inward force exerted by boundary particles. We choose our unit of length by setting the average radius of the particles to unity, i.e. $\bar{a} = 1$. We set the force scale by choosing the repulsion coefficient $k = 1$. We fix our unit of time by letting the characteristic timescale of repulsion be unity: $\tau = \zeta/k = 1$. Furthermore, we may set $\chi = 1$, since we can set the strength of all torques individually [1].

A direct consequence of the nearest neighbour alignment and the presence of a non-negligible inwards torque, is that there will be some alignment mismatches, or defects, inside the cluster. The Poincaré-Hopf-theorem for vector fields dictates that a simply connected cluster must have at least one such defect. We find that these defects act as organizing centres for the particles. Therefore, multiple defects either quickly coalesce or cause the cluster to break up into smaller clusters, each with its own defect. To ensure that no more than one defect will exist, we initialize our simulations by placing the particles on a square lattice in a rectangular shape with a width of 10 particles, with a small deviation from the exact lattice points. Furthermore, we set the initial direction along the long edge of the rectangle, with a deviation up to $\pi/4$ radians. We then run our model for 10^8 steps for a total number of $N = 1$, $N = 100$, $N = 200$, $N = 400$, $N = 800$, $N = 1000$ or $N = 1600$ particles with alignment coefficients $0.1 \leq \lambda_a \leq 1$ and $0.04 \leq \lambda_s \leq 0.08$. We keep the other interactions constant for all simulations, at $\lambda_n = 0.03$, $\lambda_{F_{\text{in}}} = 0.3$ and $\lambda_{T_{\text{in}}} = 3$. By choosing these values we ensure that the noise never exceeds the alignment, the boundary force is small compared to the repulsion, and particles on the boundary will turn inwards for even the largest value of the alignment parameter λ_a.

We find four main types of behaviour. The cluster of particles can remain simply connected and migrate either randomly (type 1: migrating; see figure 2.2a), or in straight lines or arcs of constant curvature without internal rearrangements (type 2: jammed; see figure 2.2b). Alternatively, the cluster can change its topology by either breaking apart (type 3: breakup; not shown) or transforming into a doughnut shape with a hole in the middle (type 4: rotating; figure 2.2c). We can distinguish these types of behaviour by looking at the cluster's orientational order parameter, defined as

$$\phi \equiv \frac{1}{N}\left|\sum_{i=0}^{N} \hat{\psi}_i\right|. \tag{2.5}$$

A high value of the order parameter tells us that the cluster has a net migration direction. A low value of the order parameter means that the individual particle orientations effectively cancel and the cluster is either jammed or rotating in place. The latter two types of motion are easily distinguishable visually.

We save the average location of the particles, the location of the defect and the value of the order parameter every 128 steps. If the cluster breaks up, the order parameter will show a slight drop. We can verify the break up by plotting the location of the defect. If we find multiple defects, or we find that the average position does not follow the defect like a trailer follows a car, we conclude that the

[1] We need to set χ because Stokes' paradox does not allow us to relate the translational and rotational viscosities η and η_R [23].

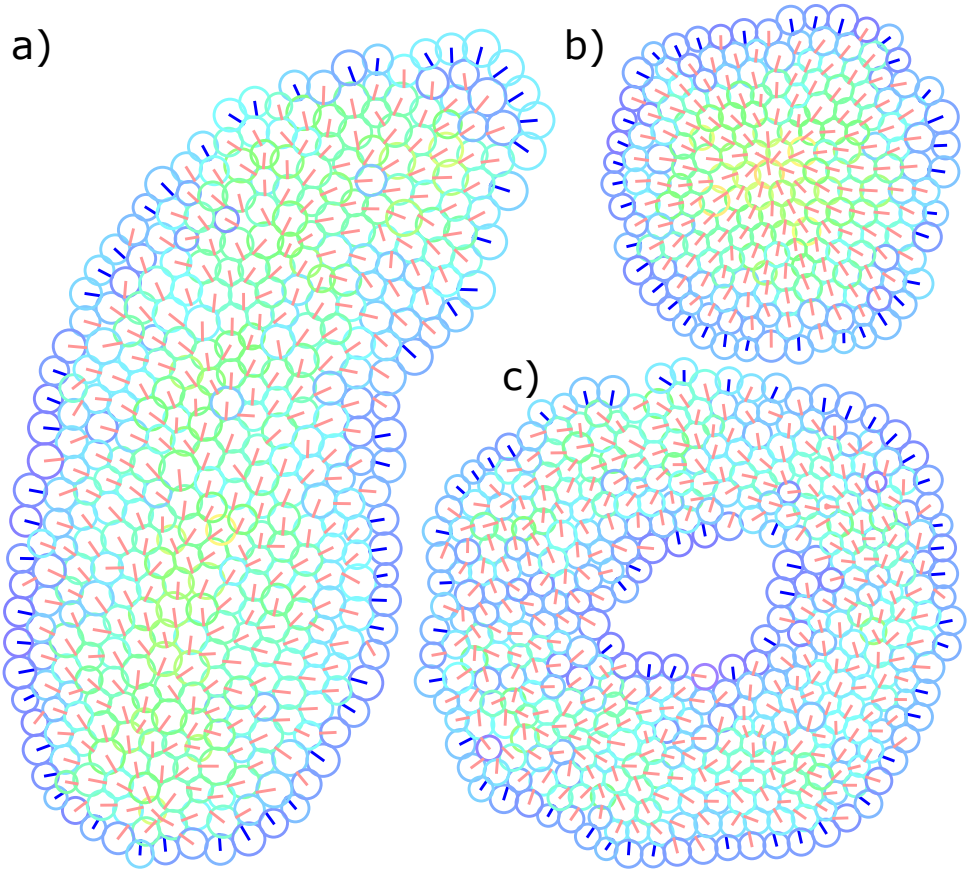

Figure 2.2: Typical snapshots for a) migrating $N = 400$, b) jammed $N = 200$ and c) rotating $N = 400$ clusters. The color code blue-green-yellow indicates the degree of overlap with neighbouring particles in increasing order. Each particle's orientation is shown by a line originating from the particle's center. This line is red for particles in bulk or blue for particles on the boundary exerting additional force and torque.

topology of the cluster has changed. We find the diffusion coefficient D of the cluster from the velocity autocorrelation function of the average location of the particles. To do so reliably, we discard the first 10^6 simulation steps to eliminate the effects of the transition from the initial configuration to the shape the cluster naturally takes when migrating.

2

3. Results and discussion

3.1. The order parameter characterizes behaviour

We ran ten simulations each for cluster sizes $N = 100$, $N = 200$, $N = 400$, $N = 800$, $N = 1000$ and $N = 1600$, seven values of the alignment strength λ_a, and five values of the self-propulsion, λ_s. We found rich state behaviour. A lack of alignment resulted in the cluster breaking up, whereas very strong alignment in combination with little activity resulted in a jammed system. In the jammed state, all particles are oriented towards the center of the cluster and there are very few rearrangements (see figure 2.2b). For intermediate values of the alignment strength, the cluster forms an elongated structure. This 'slug' has its orientational defect close to the leading edge, dictating more or less the direction of motion. The exact location of the defect is subject to random fluctuations, because of the noise on the particle orientations. Hence, the movement of the slug is a random walk. Finally, for high activity or weak alignment, the cluster eventually folds onto itself, creating a vortex state. In a vortex, all the particles revolve around a common center such that the net movement is cancelled out. The defect is removed by the creation of a hole in the middle.

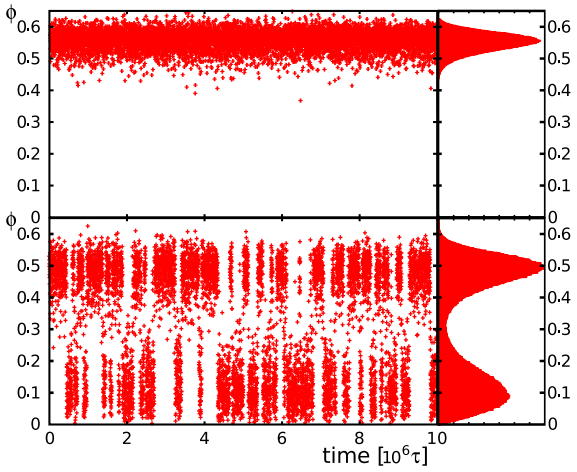

Figure 2.3: Evolution of the order parameter ϕ for $N = 400$, $\lambda_s = 0.07$ and $\lambda_a = 0.67$ (top), and $N = 400$, $\lambda_s = 0.07$ and $\lambda_a = 0.30$ (bottom) over time in units of τ. The histogram in the top panel has one peak at $\phi \sim 0.55$, which indicates that the cluster is in the migration state. The global behaviour of the cluster in the bottom panel constantly switches between migration (with $\phi \sim 0.5$) and rotation (with $\phi \sim 0.1$). The right hand panel shows the associated histogram with a bimodal distribution that represents two distinct types of behaviour.

We can distinguish between the different states using the order parameter (equation 2.5). figure 2.3 displays two examples of the evolution of the order parameter during the simulation, as well as their histograms. For the migration state (top panel), we find only one peak in the histogram. The migration state is characterized by an order parameter $\phi > 0.25$. In the rotation state, the histogram also has a

single peak, but at lower values of the order parameter, $\phi < 0.15$. The jammed state can have a peak at any value of ϕ, depending on the configuration it got stuck in. Since jammed states follow straight or circular paths (in contrast to the random walk of migrating clusters and stationary position of rotating clusters), distinguishing between jammed, rotating and migrating clusters is easy. At the boundaries between migrating and jamming, and between migrating and rotating, we find bistable or mixed states that perform a kind of run-and-tumble motion. The associated histogram of the order parameter ϕ has two peaks, as shown in the bottom panel of figure 2.3.

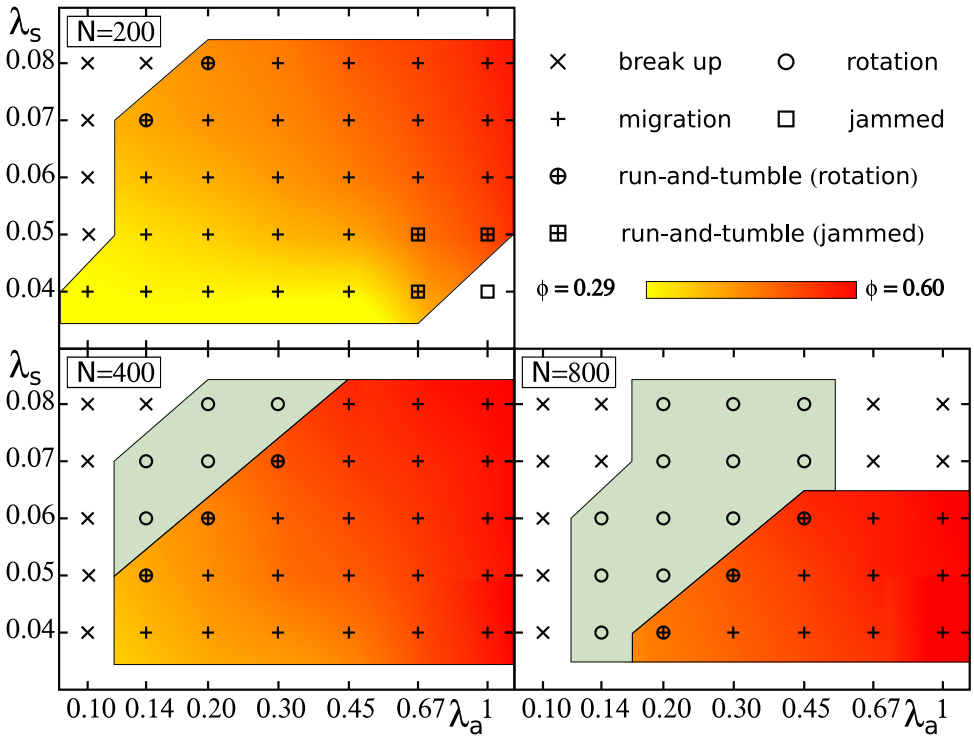

Figure 2.4: State diagrams of the global behaviour for 200, 400 and 800 particles with varying activity per particle λ_s, and alignment strength λ_a. The cluster may break up (×), migrate (+), form a vortex (◯) or jam with all particles facing the center of the cluster (□). Clusters may also perform run-and-tumble motion, a bistable state mixing two types of behaviour. These mixed states are denoted with the chimeric symbols ⊕ and ⊞ for migration with rotation and jamming, respectively. The degree of alignment is measured by the order parameter ϕ for migrating clusters. Yellow corresponds to low values of ϕ, red to high values of ϕ. The green area corresponds to purely rotating clusters. Lines are guides to the eye.

3.2. State diagram

We have captured the various types of behaviour in state diagrams (figure 2.4). For $N = 200$ particles, most of the state diagram is occupied by migrating colonies (+).

For low activity, the system jams like passive granular matter at high density (□). A strong alignment contributes positively towards jamming by preventing rearrangements (see figure 2.2b). For very weak alignment, the cluster is disordered and falls apart (×). By increasing the number of particles these states shift towards the bottom right, making room for another state between break up and migration. At high activity and weak alignment, a migrating cluster is likely to fold onto itself. This creates a vortex state (◯) where all particles circle around the topological defect, which can even be resolved by a gap in the middle (see figure 2.2c). Increasing the number of particles further ($N = 800$) continues the trend of shifting towards the bottom right. The break ups in the top right corner (high alignment and high self-propulsion) are caused by particles falling off the tail of a migrating cluster due to its strongly elongated structure. Boundary particles literally pinch off small pieces of the 3-4 particle wide tail until the main cluster reaches a stable size.

The most interesting points in the state diagrams are the points between pure migration and rotation, and between migration and jamming (⊕ and ⊞ respectively). We observed bistable states where both types of global behaviour are present. The resulting motion is a run-and-tumble. When the order parameter has a high value the cluster migrates. During migration the defect can move towards the middle of a cluster due to the noise on the individual orientations and enter the jammed state or the rotation state with a low order parameter. The same noise is responsible for undoing this process, and allow the cluster to resume migration, in a direction independent of the direction before it went into the state of low order. The bottom panel of figure 2.3 shows the evolution of the order parameter and the corresponding histogram for a bistable state between migration and rotation. The time between transitions increased dramatically when we increased the value of the alignment parameter. For $N = 800$ particles at $\lambda_a = 0.45$, the typical time the cluster spends in one of the two states was of the same order as our default simulation length ($10^7\tau$). The states last long because the transitions happen when the defect has moved from the boundary to the center by random fluctuations. A high alignment parameter limits the mobility of the defect within the cluster.

Note that figure 2.4 shows that the global behaviour changes with the number of particles. For example, an aggregating cluster can change from migration to run-and-tumble to pure rotation by collecting more particles on its way. No particle is aware of the size of the cluster. Consequently, even though the local interactions remain the same, the global behaviour can change dramatically.

We also constructed state diagrams for $N = 100$, $N = 1000$ and $N = 1600$ particles. The $N = 100$ diagram showed many signs of finite size effects. Clusters of only 100 particles have a large number of particles on the boundary. Statistical fluctuations on the order parameter became so large that characterizing the states was far from trivial. Unsurprisingly, the state diagram for $N = 1000$ looks very similar to $N = 800$. Also the state diagram of $N = 1600$ shows no surprises with only break ups and vortex states. Furthermore, we did some simulations with extreme values for the alignment and self-propulsion parameters for $N = 400$ in order to see where the transition lines are and how they move when changing the size of the cluster (figure 2.5). We retrieved the jammed state for a high value of

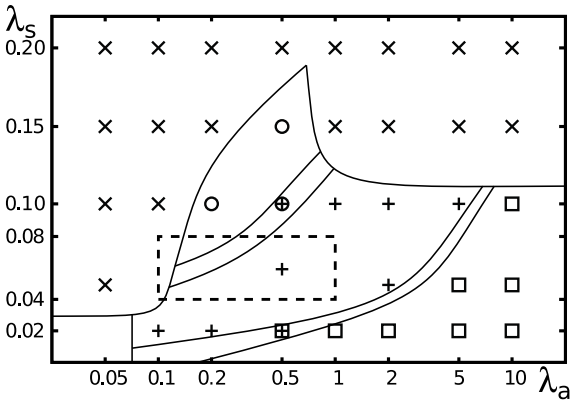

Figure 2.5: Zoomed out version of the $N = 400$ state diagram in figure 2.4. The dashed rectangle corresponds to the region shown in figure 2.4. Boundaries between states generally shift towards the bottom right corner with increasing particle number. Bistable states form a bridge between rotation and migration, and between migration and jammed.

the alignment or a low self-propulsion. We also find bistable states at higher values of λ_a and λ_s, which suggests that transitions are smooth and we can easily tune the parameters such that the amount of time the cluster spends in either state is equal. Finally, there is a small unlabelled region with low activity and low alignment, where the self-propulsion is too low to tear the boundary apart. At the same time, the alignment is too weak to overcome the noise, such that the particles rotate randomly while hardly moving.

3.3. Migrating collectively boosts the diffusion constant

A large fraction of our state diagrams is taken up by migrating clusters (+). These clusters perform random walks on the infinite plane. The movement of the cluster is guided by the location of the defect since most particles are pointing towards it. However, the clusters are very dynamic, and particles take turns being close to the defect. In the bulk, particles move towards the defect. At the defect, the pressure is higher than the surface tension provided by the boundary particles. This allows particles from the bulk to escape into the boundary at the leading edge. At the boundary, particles move towards the trailing end of the cluster since they are now pointing in a different direction than the cluster's net motion. Once they are close to the trailing end, the pressure in the bulk is lower and the particles can penetrate in to repeat the cycle.

We calculated the diffusion constant D of these migrating clusters using their velocity auto correlation function and their mean square displacement. We found a significant increase in the diffusion constant for clusters compared to single particles. In figure 2.6 we plot the diffusion constant for migrating clusters with $N = 1$ (lines), $N = 200$ (pluses), $N = 400$ (crosses) and $N = 800$ (triangles). Different colors represent different values of the strength of the self-propulsion force. We see that the diffusion constant is larger (up to three orders of magnitude for strong local alignment) than for a single particle. Hence, organisms in swarms may follow similar rules as described in our model to quickly explore large regions when looking for resources.

For single particles we verified that the diffusion constant scales quadratically

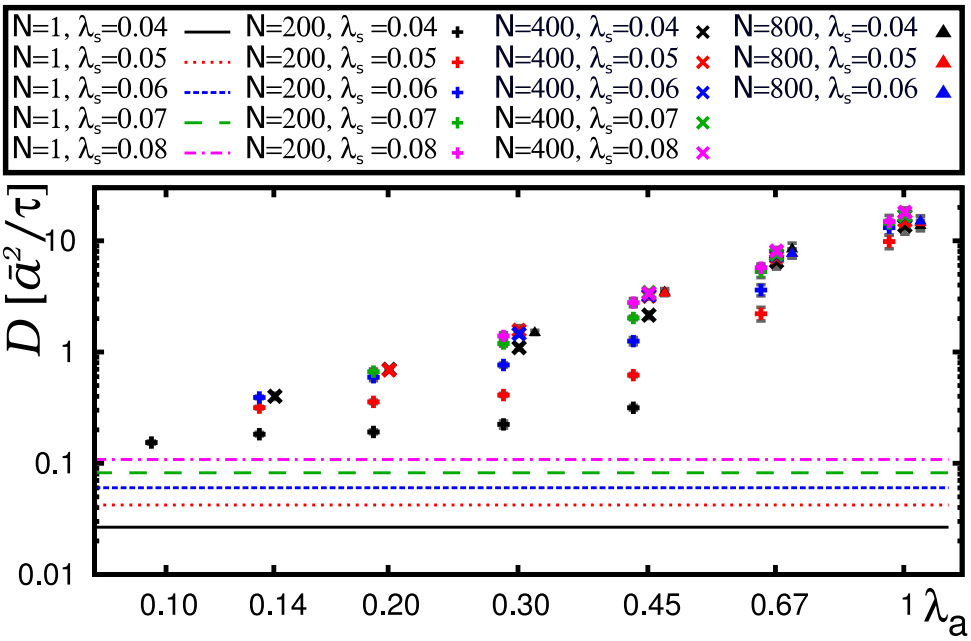

Figure 2.6: Diffusion constants of the center of mass in the migrating state with N particles, in units of $\bar{a}^2/\tau$, for different values of alignment strength λ_a. Lines correspond to $N = 1$, pluses to $N = 200$, crosses to $N = 400$ and triangles to $N = 800$ (plotted next to each other for clarity). Colours correspond to different values of the self-propulsion strength λ_s: black (solid line) $\lambda_s = 0.04$, blue (dotted line) $\lambda_s = 0.05$, red (short dashed line) $\lambda_s = 0.06$, pink (long dashed line) $\lambda_s = 0.07$, light green (dot-dashed line) $\lambda_s = 0.08$. Collective migration can increase the diffusion constant by up to three orders of magnitude.

with the self-propulsion strength, $D \propto \lambda_s^2$, whereas for large clusters the individual velocities hardly affect the diffusion constant. Similarly, we find that the persistence length ℓ_p increases with λ_s for small ($N = 1$ and $N = 200$) clusters, but slightly decreases with λ_s for larger ($N = 400$ and $N = 800$) clusters. In small clusters an increased activity causes the path length between turns (and thus the persistence length) to increase. In contrast, larger clusters will turn more quickly when they become more active. A possible explanation may be that a higher amount of activity pushes the defect forward, closer to the boundary. Consequently, the cluster changes its shape and becomes longer and narrower when λ_s increases. With fewer particles at the tip, displacements of the defect are less damped, resulting in more and sharper turns. Therefore, both the persistence length decreases, and the likelihood of the cluster entering the rotation state increases.

To appreciate the relation between the diffusion constant and the alignment strength, we work out the Green-Kubo relation in two dimensions [24]. Let $\vec{v}_c$ be the velocity of the centre of mass of the cluster, ℓ_p the persistence length of its path

and $\theta(t)$ the angle between $\vec{v}_c(0)$ and $\vec{v}_c(t)$. The diffusion constant is then given by

$$D = \frac{1}{2}\int_0^\infty \langle \vec{v}_c(0)\cdot\vec{v}_c(t)\rangle \,\mathrm{d}t = \frac{v_c^2}{2}\int_0^\infty \langle \cos\left(\theta(t)\right)\rangle \,\mathrm{d}t$$
$$= \frac{v_c^2}{2}\int_0^\infty e^{-\frac{v_c t}{\ell_p(\lambda_s,\lambda_a)}}\,\mathrm{d}t = \frac{1}{2}v_c\ell_p(\lambda_s,\lambda_a), \tag{2.6}$$

where we approximated that $\ell(t) \approx v_c t$, i.e., the length of the path travelled by the average position of the cluster can be approximated by the product of the average velocity v_c and the time interval. We see that a more persistent trajectory leads to a higher diffusion coefficient. The alignment counters the noise that is responsible for diffusion in the first place. The increased persistence makes clusters diffuse faster, even though the net speed of the cluster is less than the self-propulsion speed of a single particle - that is, clusters are slower than individuals because the particles are not all perfectly aligned. In fact, we can use the order parameter ϕ to derive the velocity of the cluster.

$$\vec{v}_c = \frac{1}{N}\sum_i^N \vec{v}_i = \frac{1}{N}\sum \frac{\vec{F}_i}{\alpha_i\zeta}$$
$$= \frac{\bar{a}}{N\tau}\left(\sum_i^N \frac{\lambda_s\hat{\psi}_i}{\alpha_i} + \sum_{i,j\neq i}^N \frac{\vec{d}_{ij}}{\alpha_i\bar{a}} + \sum_{i\in\text{boundary}} \frac{\lambda_{F_\text{in}}\hat{\psi}_i\left(\theta_{\text{out},i}-\pi\right)}{\alpha_i}\right). \tag{2.7}$$

The second term in equation 2.7 drops out since $d_{ij} = -d_{ji}$, if we neglect the effects of polydispersity on the velocity by setting $\alpha_i = 1$. The last term will also be small since the inward force by particles on opposing sides of the cluster tend to cancel out. We thus arrive at

$$|\vec{v}_c| = \frac{\bar{a}\lambda_s\phi}{\tau}. \tag{2.8}$$

Because a higher value of the alignment strength λ_a results in an increase of the order parameter, both the persistence length ℓ_p and the cluster velocity $\vec{v}_c$ increase with λ_a.

To verify that the assumptions made in deriving equations 2.6 and 2.8 are justified, we plot both relations in figure 2.7, together with our simulation data. The assumptions are that the speed of the cluster $|\vec{v}_c|$ is constant in time and that the polydispersity of the particles has little effect on the magnitude of the forces. The polydispersity merely serves as a way to prevent crystallization. From our simulations, we find that the diffusion constant D depends linearly on $\ell_p v_c$ with slope $\frac{1}{2}$ for all cluster sizes, consistent with equation 2.6. Towards higher values of $\ell_p v_c$, determining the persistence length and diffusion constant becomes harder as the simulation is finite. figure 2.7b shows that equation 2.8 holds for all cluster sizes.

3.4. Migrating and rotating states in biology

We have shown that simple, and from the perspective of the individual, sensible rules on local scales lead to various types of behaviour that are relevant for biological

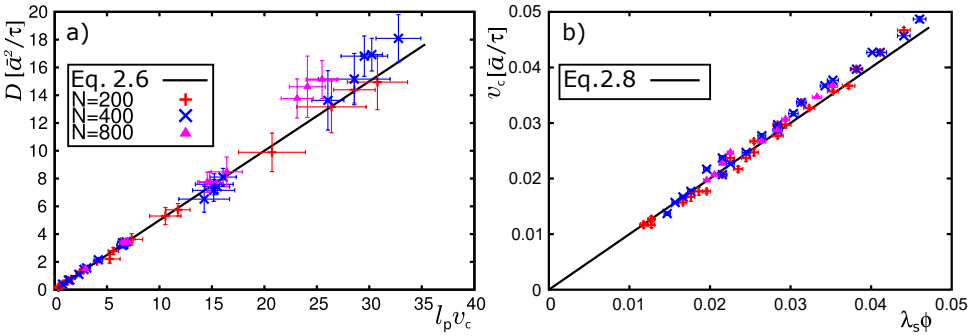

Figure 2.7: a) The diffusion coefficient of migrating clusters, in units of $\bar{a}^2/\tau$, as a function of $\ell_p v_c$, for $N = 200$ (red pluses), $N = 400$ (blue crosses) and $N = 800$ (magenta triangles) particles. The black line is the exact result from equation 2.6. b) The speed of migrating clusters with self-propulsion strength λ_s times order parameter ϕ. The black line is the exact relation from equation 2.8.

organisms. The fast collective migration state for example is useful when exploring large areas for food. This mechanism is used by both amoebae [22] and bacteria [21]. The rotation state is often observed as the onset of the formation of a fruiting body which are formed by am]ong others, the amoeba *Dictyostelium Discoideum* [22] and Myxobacteria [25]. Furthermore we found a state where the system can switch between collective migration and stationary rotation. The ratio of time spent in one of these two types of behaviour is quite sensitive to changes in activity or alignment strength. This sensitivity allows the system to easily switch between migration and rotation when the environment changes.

4. Conclusion

We have shown that finite, stable clusters of self-propelled soft particles can be formed with only local rules. The boundary rule that we introduced creates an effective surface tension for our clusters, which prevents their breakup. The rule also dictates the presence of at least one defect in each cluster. We found that these defects dominate the clusters' global dynamics. Elongated, slug-like migrating clusters exhibit enhanced motility with a diffusion constant that can be up to three orders of magnitude higher than that of an individual particle. The high diffusion constant demonstrates how clustering can be a good strategy for organisms in environments that are hostile or scarce in food. For larger clusters, there is a spontaneous transition to a topologically and dynamically different state: a doughnut-shaped rotating cluster with no net movement. Clusters can be brought from the moving to the stationary rotating state simply by growing in size, without the need for an additional decision mechanism.

The vortex and migration state, and the migration and jammed state are separated by bistable states where both types of behaviour are present. The average time the cluster spends in each state can be controlled by changing the strength of alignment between particles or the self-propulsion of the particles. Therefore, in con-

trast to the jamming transition, which occurs at a critical density, we find no single critical value for the strength of alignment nor for the self-propulsion. Instead, we find a gradual transition where both states (migration and rotation/jammed state) coexist. With our model the density of our clusters cannot be set a priori, so we could not verify the observation by Henkes et al. [11] who saw that the jamming transition is sharp when adjusting the density.

We found relations (equations 2.6 and 2.8) between the diffusion constant, the persistence length and our order parameter defined in equation 2.5. The data collapse in figure 2.7 proves that the assumptions we made to derive these relations are justified. Moreover, it shows that these relations hold independently of cluster size, providing a method to determine the values of the alignment and self-propulsion strength directly from experiments. Although our model is simple, it describes features found in biological swarms. Therefore, our results suggest that similar mechanisms based on local rules may be found in living systems, even if there are also more long-range (e.g. signaling-based) biological decision making processes present.

References

[1] E. Shaw, *Schooling Fishes,* Am. Sci. **66**, 166 (1978).

[2] D. S. Calovi, U. Lopez, S. Ngo, C. Sire, H. Chaté, and G. Theraulaz, *Swarming, schooling, milling: phase diagram of a data-driven fish school model,* New J. Phys. **16**, 015026 (2014).

[3] D. A. Kessler and H. Levine, *Pattern formation in Dictyostelium via the dynamics of cooperative biological entities,* Phys. Rev. E **48**, 4801 (1993).

[4] G. Grégoire, H. Chaté, and Y. Tu, *Moving and staying together without a leader,* Phys. D **181**, 157 (2003).

[5] S. Nagano, *Diffusion-Assisted Aggregation and Synchronization in Dictyostelium discoideum,* Phys. Rev. Lett. **80**, 4826 (1998).

[6] W.-J. Rappel, A. Nicol, A. Sarkissian, H. Levine, and W. F. Loomis, *Self-organized Vortex State in Two-Dimensional Dictyostelium Dynamics,* Phys. Rev. Lett. **83**, 1247 (1999).

[7] T. Butt, T. Mufti, A. Humayun, P. B. Rosenthal, S. Khan, S. Khan, and J. E. Molloy, *Myosin motors drive long range alignment of actin filaments,* J. Biol. Chem. **285**, 4964 (2010).

[8] T. Vicsek, A. Czirók, E. Ben-Jacob, I. Cohen, and O. Shochet, *Novel type of phase transition in a system of self-driven particles,* Phys. Rev. Lett. **75**, 1226 (1995).

[9] T. Vicsek and A. Zafeiris, *Collective motion,* Phys. Rep. **517**, 71 (2012).

[10] A. J. Liu and S. R. Nagel, *Nonlinear dynamics: Jamming is not just cool any more,* Nature **396**, 21 (1998).

[11] S. Henkes, Y. Fily, and M. C. Marchetti, *Active jamming: Self-propelled soft particles at high density,* Phys. Rev. E **84**, 040301 (2011).

[12] B. M. Mognetti, A. Šarić, S. Angioletti-Uberti, A. Cacciuto, C. Valeriani, and D. Frenkel, *Living clusters and crystals from low-density suspensions of active colloids,* Phys. Rev. Lett. **111**, 245702 (2013).

[13] M. R. D'Orsogna, Y. L. Chuang, A. L. Bertozzi, and L. S. Chayes, *Self-propelled particles with soft-core interactions: Patterns, stability, and collapse,* Phys. Rev. Lett. **96**, 104302 (2006).

[14] N. H. P. Nguyen, E. Jankowski, and S. C. Glotzer, *Thermal and athermal three-dimensional swarms of self-propelled particles,* Phys. Rev. E **86**, 011136 (2012).

[15] B. Wang and A. Kuspa, *Dictyostelium development in the absence of cAMP,* Science **277**, 251 (1997).

[16] K. Tunstrøm, Y. Katz, C. C. Ioannou, C. Huepe, M. J. Lutz, and I. D. Couzin, *Collective states, multistability and transitional behavior in schooling fish.* PLoS Comput. Biol. **9**, e1002915 (2013).

[17] C. P. McCann, P. W. Kriebel, C. A. Parent, and W. Losert, *Cell speed, persistence and information transmission during signal relay and collective migration.* J. Cell Sci. **123**, 1724 (2010).

[18] B. Vasiev, F. Siegert, and C. J. Weller II, *A Hydrodynamic model for Dictyostelium discoideum Mound Formation,* J. Theor. Biol. **184**, 441 (1997).

[19] J. Saragosti, V. Calvez, N. Bournaveas, B. Perthame, A. Buguin, and P. Silberzan, *Directional persistence of chemotactic bacteria in a traveling concentration wave.* Proc. Natl. Acad. Sci. USA **108**, 16235 (2011).

[20] A. Czirók, E. Ben-Jacob, I. Cohen, and T. Vicsek, *Formation of complex bacterial colonies via self-generated vortices.* Phys. Rev. E **54**, 1791 (1996).

[21] M. Deforet, D. van Ditmarsch, C. Carmona-Fontaine, and J. B. Xavier, *Hyperswarming adaptations in a bacterium improve collective motility without enhancing single cell motility.* Soft Matter **10**, 2405 (2014).

[22] C. J. Weijer, *Dictyostelium morphogenesis.* Curr. Opin. Genetics Dev. **14**, 392 (2004).

[23] L. D. Landau and E. M. Lifshitz, *Fluid Mechanics* (Butterworth-Heinemann, Oxford, 1987).

[24] W. M. Visscher, *Self-Diffusion, the Green—Kubo Formulas, and the Long Tail of the Velocity-Autocorrelation Function,* Phys. Rev. A **7**, 5 (1973).

[25] J. A. Shapiro, *Bacteria as multicellular organisms,* Sci. Am. **258**, 82 (1988).

A. Deriving the dimensionless parameters for the simulation

Comparing interaction strengths is a priori ambiguous. For example, we cannot directly compare the repulsion strength, a force, with the alignment strength, a torque. Even comparing different forces with each other may not be trivial. The parameters that set the strength may have different dimensions. The repulsion strength is set by a spring constant k, which has a dimension of force over length. The self-propulsion force is simply set by a force, so comparing the values directly is meaningless. In this Appendix, we construct a framework that allows us to compare the values we feed to the simulation. We determine natural time scales for each interaction. The ratios between these time scales yield dimensionless numbers that indicate unambiguously the strength of each interaction.

As mentioned in the main text of this chapter, we consider an environment where the dynamics are over-damped. Therefore, the translational and rotational, equations of motion are replaced by their non-inertial counterparts. For disks in a two dimensional fluid, we get

$$\vec{F}_{\mathrm{res},i} = \frac{32}{3}\pi\eta a_i \dot{\vec{x}}_i \equiv \zeta\alpha_i\dot{\vec{x}}_i \qquad \text{and} \qquad T_{\mathrm{res},i} = 4\pi\eta_R a_i^2\dot{\psi}_i \equiv \chi\alpha_i^2\dot{\psi}_i \tag{2.9}$$

instead of

$$\vec{F}_{\mathrm{res},i} = m_i\ddot{\vec{x}}_i \qquad \text{and} \qquad T_{\mathrm{res},i} = I_i\ddot{\psi}_i.$$

We have defined rescaled viscosities $\zeta = 6\pi\eta\bar{a}$ and $\chi = \pi\eta_R\bar{a}^2$. We have six interactions in our model that contribute to the resultant force $\vec{F}_{\mathrm{res},i}$, and resultant torque $T_{\mathrm{res},i}$. These are the repulsion, self-propulsion, alignment, noise and a boundary tension, which consists of an inwards torque and an inwards force. We will first calculate the time scale of repulsion. Then, we determine the characteristic time scale of the other interactions and scale them relative to the characteristic time scale of repulsion. An advantage of this method is that it reduces the dimension of the parameter space by one.

A.1. Repulsion

First, let us calculate the characteristic time scale of the repulsive interaction. We find the time scale by solving the equations of motion in the absence of other interactions. We consider two particles i and j at positions x_i and x_j respectively. We take these particles to be of average size, i.e. $a_i = a_j = \bar{a}$, or $\alpha_i = \alpha_j = 1$. The repulsive force between them is $F_{\mathrm{rep}} = k(x_j - x_i - 2\bar{a})$. For simplicity we fix particle j and choose our coordinates such that particle j has position $x_j = 2\bar{a}$. Then, the equation of motion reduces to

$$\begin{aligned} F_{\mathrm{res},i} &= F_{\mathrm{rep},i} \\ \zeta\frac{\mathrm{d}x_i}{\mathrm{d}t} &= -kx_i \end{aligned} \tag{2.10}$$

and can be solved for x_i.

$$\begin{aligned} \frac{\mathrm{d}x_i}{x_i} &= -\frac{k\,\mathrm{d}t}{\zeta} \\ \ln(x_i) &= -\frac{k}{\zeta}t + c \\ x_i &= Ae^{-kt/\zeta}. \end{aligned} \tag{2.11}$$

We can now define a time scale $\tau = \frac{\zeta}{k}$, the time it takes to reduce the overlap by a factor e.

A.2. Alignment

Our simple interaction for the alignment allows us to calculate the characteristic time for alignment in a way almost identical to the calculation of the characteristic time for repulsion. Let us consider a particle i with orientation $\hat{\psi}$. This particle aligns with a local preferred orientation $\hat{\Psi}_i$. The direction $\hat{\Psi}_i$ can be calculated using

$$\hat{\Psi}_i = \frac{1}{\left|\sum_{j\in\mathcal{N}_i}\hat{\psi}_j\right|}\sum_{j\in\mathcal{N}_i}\hat{\psi}_j. \tag{2.12}$$

This looks rather nasty, because we have to normalise $\hat{\Psi}_i$. However, with equation 2.12 we simply calculate the average orientation of the set of neighbours, $\mathcal{N}_i$, of particle i. If we denote the angle between $\hat{\psi}_i$ and $\hat{\Psi}_i$ with $\Delta\psi_i$, we can write

$$T_i^{\text{align}} = T_{\text{align}}\Delta\psi_i, \tag{2.13}$$

where T_i^{align} is the torque on particle i due to the alignment, and T_{align} is a constant that sets the magnitude of the interaction. At this point it is convenient to choose coordinates such that the preferred orientation $\hat{\Psi}_i = \hat{x}$. If we now denote the angle that the orientation $\hat{\psi}_i$ makes with the x-axis with the (scalar) angle ψ_i, we can express the torque in terms of this angle. We get

$$\begin{aligned} T_{\text{res},i} &= T_i^{\text{align}} \\ \chi\frac{\mathrm{d}\psi_i}{\mathrm{d}t} &= -T_{\text{align}}\psi_i. \end{aligned} \tag{2.14}$$

Notice that this differential equation can be solved in exactly the same way as equation 2.10 for repulsion. Therefore, we can immediately write down the solution:

$$\psi_i = Be^{-T_{\text{align}}t/\chi}. \tag{2.15}$$

The natural time scale corresponding to this interaction is $\tau_a = \chi/T_{\text{align}}$. Finally, we define a dimensionless parameter as the ratio between the characteristic time scale of repulsion and alignment.

$$\lambda_a = \frac{\tau}{\tau_a} = \frac{\zeta T_{\text{align}}}{k\chi}. \tag{2.16}$$

A.3. Noise

We have implemented a noise term as a small torque of magnitude T_{noise} that is applied to each particle each time step. The torque can either be positive or negative, turning the particle counter-clockwise or clockwise with equal probability. The contribution to the torque can be expressed as

$$T_i^{\text{noise}}(t) = w_i(t) T_{\text{noise}}, \tag{2.17}$$

The $w_i(t)$ are drawn at random from the set $\{-1, +1\}$ for each particle i and at each time t. We have no correlations between particles, nor in time.

$$\langle w_i(t) w_j(t') \rangle = \delta_{ij} \delta(t' - t). \tag{2.18}$$

If we consider just a single particle, its orientation will change by a small amount $\Delta\psi$ each time step due to the random torque. The orientation one simulation step later points in almost the same direction. Notice that this description of the particle's orientation is analogous to the worm-like chain model. The orientation of particle i after n steps, $\hat{\psi}_i(n)$ corresponds to the tangent $\vec{t}(s)$ at position s along the polymer.

In contrast to the previous two interactions, the noise is not a restoring interaction. There is no natural time scale after which the torque weakens by a certain factor. Instead, we define the characteristic time scale for the noise to be the time it takes for a particle to 'forget' its orientation. To quantify the memory of its orientation, we use the concept of persistence length from the worm-like chain model. The persistence length ℓ_P of a polymer is defined using the autocorrelation function. The autocorrelation function is given by

$$e^{-s/\ell_P} = \left\langle \vec{t}(0) \cdot \vec{t}(s) \right\rangle .$$

Similarly, we can define a persistence time for the noise in our model:

$$e^{-n/n_P} = \left\langle \hat{\psi}_i(0) \cdot \hat{\psi}_i(n) \right\rangle , \tag{2.19}$$

where n_P is the number of simulation steps after which the orientation becomes uncorrelated. Let $\Delta\psi_n$ be the angle between $\hat{\psi}_i(0)$ and $\hat{\psi}_i(n)$. The total change in angle is of course a summation of all the changes during each simulation step. Then we can write

$$e^{-n/n_P} = \langle \cos(\Delta\psi_n) \rangle .$$

Now we use a Taylor-expansion on both sides for small n/n_P and small $\Delta\psi_n$. We can safely ignore terms beyond the second term of the expansion.

$$\begin{aligned} 1 - \frac{n}{n_P} &= \langle \cos(\Delta\psi_n) \rangle . \\ 1 - \frac{n}{n_P} &= \left\langle 1 - \frac{1}{2} (\Delta\psi_n)^2 \right\rangle \\ 1 - \frac{n}{n_P} &= 1 - \frac{1}{2} \left\langle (\Delta\psi_n)^2 \right\rangle \end{aligned}$$

The total change in angle after n steps is ofcourse just the sum of the changes each time step. Hence, we substitute $\Delta\psi_n = \sum_{m=1}^{n} w(m)\Delta\psi$.

$$\frac{n}{n_P} = \frac{1}{2}\left\langle \left(\Delta\psi \sum_{m=1}^{n} w(m)\right)^2 \right\rangle$$
$$\frac{n}{n_P} = \frac{\Delta\psi^2}{2}\left(\sum_{m=1}^{n}\langle w(m)^2\rangle + \sum_{m\neq l}^{n}\langle w(m)w(l)\rangle\right)$$

Recall that $w(m)$ is either -1 of $+1$, so the product with itself will always yield $w(m)^2 = 1$. The second term between the delimeters on the right hand side vanishes, because the noise is uncorrelated.

$$\frac{n}{n_P} = \frac{\Delta\psi^2}{2}n$$
$$n_P = \frac{2}{(\Delta\psi)^2}. \tag{2.20}$$

We can find $\Delta\psi$ in terms of the magnitude of the random torque, T_{noise} from the equation of motion (equation 2.9).

$$\Delta\psi = \frac{\Delta t T_{\text{noise}}}{\chi}, \tag{2.21}$$

where Δt denotes the duration of a single simulation step. Finally, we obtain a natural time scale for the noise:

$$\tau_{\text{noise}} = n_P \Delta t$$
$$\tau_{\text{noise}} = \frac{2\chi^2}{T_{\text{noise}}^2 \Delta t}. \tag{2.22}$$

The dimensionless parameter for the noise becomes

$$\lambda_n = \frac{\tau}{\tau_{\text{noise}}} = \frac{\zeta T_{\text{noise}}^2 \Delta t}{2k\chi^2}. \tag{2.23}$$

A.4. Inward force

To calculate the characteristic time scale of the inward force, we consider a configuration of particles like in figure 2.8. Particle i experiences an restoring force that brings it closer to the group. The force is

$$F_i^{\text{inward}} = F_{\text{in}}(\theta_{\text{out},i} - \theta_{\text{crit}}). \tag{2.24}$$

The magnitude of this interaction is set by F_{in}, $\theta_{\text{out},i}$ is the largest angle between consecutive neighbours, and $\theta_{\text{crit}} = \pi$. This choice is motivated by the observation

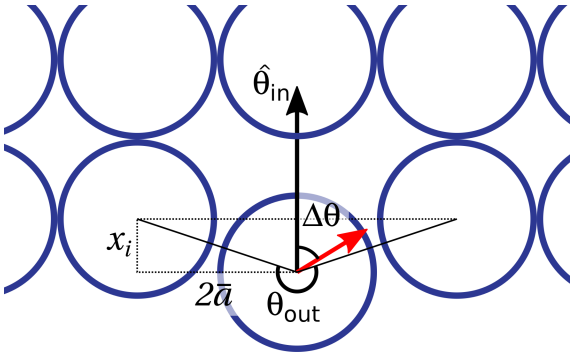

Figure 2.8: An artificial arrangement of particles to explain schematically the additional interactions for boundary particles, and how to calculate the corresponding characteristic time scales. The particle in the bottom middle will turn towards $\hat{\theta}_{\text{in}}$ with a torque proportional to $\Delta\theta$. The orientation of that particle corresponds to the red arrow. The particle's position with respect to the boundary (dotted line) is x_i. The horizontal distance to the neighbouring particles is twice the radius ($2\bar{a}$).

that when a particle has moved itself exactly between two other particles on the boundary ($\theta_{\text{out},i} = \pi$), it should stop forcing itself further into the colony. Suppose that particle i is a distance x_i from that stable position on the boundary. From figure 2.8, we find

$$\tan\left(\frac{1}{2}(\theta_{\text{out},i} - \theta_{\text{crit}})\right) = \frac{x_i}{2\bar{a}}. \tag{2.25}$$

The tangent function makes solving the equation of motion for x_i very complicated. Instead, to derive a characteristic time scale, we will solve it in the limit that the displacement x_i from the boundary is small. In this limit, we can use the small angle approximation.

$$\theta_{\text{out},i} - \theta_{\text{crit}} \approx -\frac{x_i}{\bar{a}}. \tag{2.26}$$

Solving the equation of motion (equation 2.9) now becomes trivial.

$$\begin{aligned} F_{\text{res},i} &= F_i^{\text{inward}} \\ \zeta\frac{\mathrm{d}x_i}{\mathrm{d}t} &= F_{\text{in}}(\theta_{\text{out},i} - \theta_{\text{crit}}) \\ \zeta\frac{\mathrm{d}x_i}{\mathrm{d}t} &= -\frac{F_{\text{in}}x_i}{\bar{a}} \\ \frac{\mathrm{d}x_i}{x_i} &= -\frac{F_{\text{in}}}{\zeta\bar{a}}\,\mathrm{d}t \\ x_i &= Ce^{-F_{\text{in}}t/\zeta\bar{a}} \end{aligned} \tag{2.27}$$

The characteristic time scale for the inward force is $\tau_{F_{\text{in}}} = \zeta\bar{a}/F_{\text{in}}$. Thus, we get for the dimensionless scaling parameter

$$\lambda_{F_{\text{in}}} = \frac{\tau}{\tau_{F_{\text{in}}}} = \frac{F_{\text{in}}}{k\bar{a}}. \tag{2.28}$$

A.5. Inward torque

The torque applied to a boundary particle i is given by

$$T_i^{\text{inward}} = T_{\text{in}}\Delta\theta. \tag{2.29}$$

Again, the magnitude of this interaction is T_{in}, and $\Delta\theta$ is the angle between $\hat{\theta}_{\text{in}}$ and the particle's orientation $\hat{\psi}_i$ (see also figure 2.8). The unit vector $\hat{\theta}_{\text{in}}$ is defined as the exterior bisector of angle θ_{out} and denotes the direction towards the inside of the colony. If we choose our axis such that $\hat{\theta}_{\text{in}}$ corresponds to the x-axis, we can represent $\Delta\theta$ simply with the scalar interpretation of particle i's orientation. That is, $\Delta\theta = -\psi_i$. If we now plug this into the equation of motion, we see that this interaction also acts as a spring-like interaction with spring constant T_{in}.

$$\begin{aligned} T_{\text{res},i} &= T_i^{\text{in}} \\ \chi \frac{\mathrm{d}\psi_i}{\mathrm{d}t} &= -T_{\text{in}}\psi_i. \\ \psi_i &= De^{-T_{\text{in}}t/\chi} \end{aligned} \tag{2.30}$$

For the characteristic time scale we have $\tau_{T_{\text{in}}} = \chi/T_{\text{in}}$, and therefore the dimensionless parameter becomes

$$\lambda_{T_{\text{in}}} = \frac{\tau}{\tau_{T_{\text{in}}}} = \frac{kT_{\text{in}}}{\zeta\chi}. \tag{2.31}$$

A.6. Self-propulsion force

So far, all the interactions in our model have a natural time scale. The self-propulsion force however does not. In fact, it does exactly the opposite of a restoring force. Self-propulsion drives the system away from equilibrium. Therefore we define the dimensionless parameter that sets the self-propulsion force similar to $\lambda_{F_{\text{in}}}$. We replace the inward force F_{in} by the self-propulsion force F_{self} to obtain

$$\lambda_{F_{\text{in}}} = \frac{F_{\text{self}}}{k\bar{a}}. \tag{2.32}$$

3

Active unjamming beyond the classical jamming density

Living matter evades the decay to equilibrium.

Erwin Schrödinger

Many biological systems form colonies at high density. Passive granular systems will be jammed at such densities, yet for the survival of biological systems it is crucial that they are dynamic. We construct a jamming phase diagram for a system of active, aligning particles, without long-range interactions and confinement. We vary the density, self-propulsion speed and the degree of alignment. Our simulations reveal that there exists an optimal degree of alignment, such that particles require a minimal force to unjam and therefore allow for rearrangements.

1. Introduction

In chapter 2, we developed a model to study the behaviour displayed by a many biological systems. Our model, a combination of a Vicsek type model of active particles and the finite size effects of granular materials, results in a wide variety of dynamical systems. We simulated colonies of up to 1600 particles, but typically, aggregates on small scales contain way more constituents. Unfortunately, current computing power does not allow us to perform simulations on that level. Furthermore, in chapter 2, we ensured that all particles stayed together as a group by providing a boundary term that turns agents towards the colony when they are at the boundary. However, with colonies of just 1600 particles, effects of the boundary will be pronounced in the bulk. We can mimic an infinite system by applying periodic boundary conditions and eliminate a boundary rule all together.

In this chapter we study the dynamics (or absence of dynamics) within bacterial colonies and tissues. The density in these systems is high which means that the bacteria or cells are in physical contact with each other. These systems often have such a high density that they risk becoming jammed. Nonetheless, the constituents rely heavily on rearrangements for their survival. These observations lead us to the following questions: how do colonies prevent jamming in the first place and what are the limits on the density in the colony and the forces that its members generate?

So far, the studies that use Vicsek alignment mostly focus on the (rich) dynamics. In this chapter we focus on the very thing that these active systems are trying to prevent: jamming. We classify jamming based on an internal diffusion coefficient that represents the ability to rearrange. We investigate the effect that self-propulsion and alignment have on the jamming transition, at densities well above the classical jamming density. Our simulations indicate that at high density, systems require both alignment with neighbours and orientational noise to unjam. Our results show that there exists an optimal competition between alignment and noise such that particles require a minimal self-propulsion force to unjam.

2. Model system

We placed N soft, self-propelled particles in a square with double periodic boundary conditions. The radii of the particles are drawn from a Gaussian distribution with mean $\mu = \bar{a}$ and standard deviation $\sigma = \bar{a}/10$. The variation in radii prevents artificial crystallisation effects. As mentioned in the introduction of this thesis 1, we model systems in the regime where viscous forces dominate over inertial forces, e.g. bacteria or other unicellular organisms and cell tissues. Therefore, the dynamics of the particles are over-damped and the equation of motion is given by Stokes' law:

$$\vec{F}_i = \zeta_i \vec{v}_i. \tag{3.1}$$

In equation 3.1, $\vec{F}_i$ denotes the total force exerted on particle i. This force results in an instantaneous velocity $\vec{v}_i$ of the particle. The proportionality constant ζ_i depends the viscosity η and the particle's radius a_i and is given by $\zeta_i = 6\pi\eta a_i$ or $\zeta_i = (32/3)\eta a_i$ in three and two dimensions respectively. The total force on the particle is the sum of steric repulsion forces with all particle j that generate overlap,

$\vec{F}_{\text{rep},j}$, and a self-propulsion force, $\vec{F}_{\text{sp}}$. We choose a simple harmonic repulsion, such that the force is proportional to, and in the direction of the linear overlap $\vec{d}_{ij}$. Hence, the total force becomes

$$\vec{F}_i = \sum_j \vec{F}_{\text{rep}} + \vec{F}_{\text{sp}} = \sum_j k\vec{d}_{ij} + F_{\text{sp}} \frac{a_i}{\bar{a}} \hat{\psi}_i, \tag{3.2}$$

$$\vec{F}_i = \sum_j k\vec{d}_{ij} + \lambda_s k a_i \hat{\psi}_i, \tag{3.3}$$

where k is the spring constant for the repulsive term and F_{sp} sets the magnitude of the self-propulsion force. Any particle i propels itself along an intrinsic unit vector $\hat{\psi}_i$, which we will refer to as the orientation of particle i. We choose the self-propulsion force to be proportional to the particle's size, such that the speed of differently sized particles would be the same in the absence of pairwise interactions. In equation 3.3 we use that we can rescale all forces by $k\bar{a}$, which follows naturally from the repulsion term. Next, we define the dimensionless parameter $\lambda_s = F_{\text{sp}}/k\bar{a}$ to set the strength of the self-propulsion in our simulations.

We adopt the rules for the orientation of our particles from the original Vicsek model. Two competing effects regulate the orientation of a particle. On the one hand, particles want to align with a local director, while on the other hand, they are subjected to an orientational noise. Note that this noise is not of a thermal origin, rather, it should be interpreted as an uncertainty in determining the direction of the local director. During each simulation step, the new orientation of particle i is calculated by

$$\hat{\psi}_i = \text{Rot}(\theta) \frac{\sum_{j \in \mathcal{N}_i} \hat{\psi}_j}{\left| \sum_{j \in \mathcal{N}_i} \hat{\psi}_j \right|}. \tag{3.4}$$

Here, $\text{Rot}(\theta)$ is the 2D rotation matrix, that rotates a vector by an angle θ. We draw the rotation angle θ from a uniform distribution between $-\lambda_n \pi$ and $\lambda_n \pi$, where we set λ_n between zero (low noise) and one (high noise). We define $\mathcal{N}_i$ to be the set of particles in the neighbourhood of particle i. A particle j is in the neighbourhood of particle i if the distance between i and j is smaller than $2.8\bar{a}$. We choose this distance such that two neighbouring large particles will still be considered neighbours, whereas two small particles separated by a third will not.

The Vicsek order parameter quantifies the competition between alignment and orientational noise. The order parameter is a characteristic of the colony as a whole and turns out to be a more intuitive measure of the competition between alignment and noise. It is defined as

$$\phi = \frac{1}{N} \left| \sum_{i=1}^{N} \hat{\psi}_i \right|. \tag{3.5}$$

The order parameter equals unity for perfect alignment between all particles and is close to zero when the direction of all particles are uncorrelated from those of their neighbours.

Note that the noise term is exclusively orientational. This noise term is an essential competing effect to the alignment for dynamics in the system. We choose not to include a noise term in the force equation to have a minimal system that displays the dynamics we want to study. We use the Vicsek alignment over a rotational analogue (equation 2.9 from chapter 2) of the force equation (equation 3.3), because the jamming transition naturally comes with a dramatic slow down of the dynamics and diverging time scales. The time scales concerning the dynamics near the jamming transition and the rotation of particles at high noise lie so far apart that we would require infeasibly many simulation steps to study this system. Instead, we choose to use an update mechanism for the orientation identical to the mechanism used in the original Vicsek model.

3. Results

We simulate $N = 1024$ particles in a box of size $L \times L$ (see figure 3.1 for two snapshots), where we calculate L from the imposed dimensionless packing fraction $\rho = \sum_{i=1}^{N} \pi a_i^2 / L^2$. All distances are in units of the average particle radius $\bar{a} = 1$ and we set the force scale by choosing $k = 1$ for our simulations. Our unit of time is set by the relaxation time of the repulsive interaction $\tau = \zeta/k = 1$. We adjust the number of simulation steps per unit time such that the displacement by the self-propulsion force is 1/1000th of the average particle radius, $\bar{a}$. Simulations run for a total of 10^8 steps. The parameters that we vary are the packing fraction (ρ), the self-propulsion speed of the particles (λ_s), and the size of the interval from which we draw a random angle that causes a mismatch in the alignment between particles (λ_n). In hindsight, making the number of simulation steps dependent on the value of λ_s is an odd choice as it affects the orientational noise. To correct this issue, we will refer to a rescaled noise parameter $\lambda_n' = \lambda_n/\sqrt{\Delta t}$, where Δt is the duration of a simulation step. We will also add follow-up results from Daniel McCusker, who carried out the simulations with a constant number of steps per unit time.

3.1. Classifying jammed and unjammed systems

With the classical jamming transition at $\rho_c = 0.843$ [1], we ran simulations at three different densities ($\rho \in \{0.845, 0.860, 0.900\}$). For the preliminary results using a simulation step that depends on λ_s, we varied the self propulsion force over two orders of magnitude ($\lambda_s \in \{0.003, 0.01, 0.03, 0.10, 0.30\}$) and we used six different values for the orientational noise ($\lambda_n \in \{0.01, 0.10, 0.30, 0.40, 0.50, 0.60, 1.00\}$). At $\lambda_n = 0$, the particles align perfectly without any noise, whereas at $\lambda_n = 1$, the particles reorient themselves in a random direction every single simulation step. Therefore, particles do not align and cannot move collectively. On top of that, the particles' trajectories have a vanishing persistence length compared to their radius. The definitive simulations use $\rho \in \{0.88, 0.92, 1.00\}$, $\lambda_s \in \{1 \times 10^{-4}, 2 \times 10^{-4}, 5 \times 10^{-4}, 1 \times 10^{-3}, 2 \times 10^{-3}, 5 \times 10^{-3}, 1 \times 10^{-2}\}$, and $\lambda_n \in \{0.2, 0.3, 0.4, 0.5, 0.6, 0.7, 0.8\}$ with a fixed duration of the simulation step $\Delta t = 0.1$.

We characterize solid-like or liquid-like behaviour by taking a direct measure of the motion in our system. Note however that a system with perfect alignment can

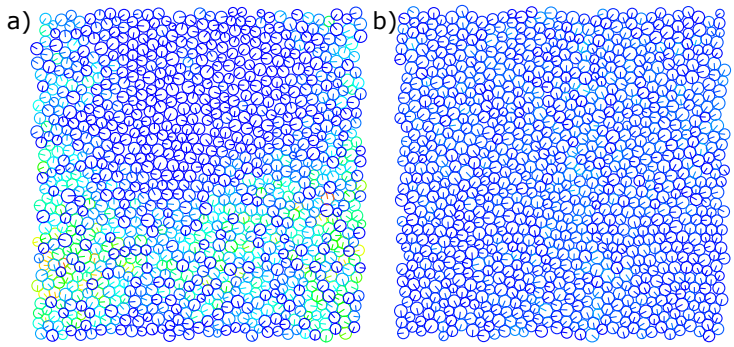

Figure 3.1: Snapshots of a) an unjammed system ($\rho = 0.86$, $\lambda_s = 0.30$, and $\lambda_n = 0.50$) and b) a jammed system ($\rho = 0.90$, $\lambda_s = 0.10$, and $\lambda_n = 0.30$). The orientation of the particles is shown by the lines originating from the centres. The colour of the perimeter indicates the amount of overlap with other particles (blue for no overlap, green/yellow for medium overlap, and red for large overlap). Unlike jammed systems, unjammed systems have large density fluctuations.

move collectively, but lacks any rearrangements and the motion is just a translation of the centre of mass. In an infinite system, or a system with periodic boundary conditions, this global translation is meaningless and such a system should still be characterized as jammed. We therefore look at rearrangements or the displacement of the particles with respect to a reference point that moves with the system. We take as this reference point the average position of all particles after thermalisation. To identify rearrangements in the system we calculate the mean squared displacement (MSD) of all particles with respect to this average position. Note that this diffusion coefficient is not a coefficient in the traditional sense of passive particles undergoing a diffusion process. In this case, the diffusion is a consequence of the activity of the particles.

In a jammed system, particles will not be able to travel more than a distance $\bar{a}$ because they are obstructed by their neighbours. This effect is known as caging and is visible in the mean squared displacement as a plateau. Particles in unjammed systems do not have this restriction, and we can assign a diffusion coefficient, D, to the linear behaviour of the MSD after the particle has escaped its cage (see figure 3.2a). We always fit a constant function and a linear function. If the best fit (using a χ-squared method) is a constant, we consider the system to be jammed (see figure 3.2b). On the other hand, if the best fit is a linear function, we consider the system to be unjammed. In some borderline cases however, the linear function would be the best fit, but the MSD would never exceed $\bar{a}^2$. Particles in such systems did not travel a distance larger than their own radius and therefore particles will not have rearranged. Hence, we also consider our system to be jammed if the fitted diffusion constant does not allow for displacements larger than $\bar{a}$ during our measurement of the MSD.

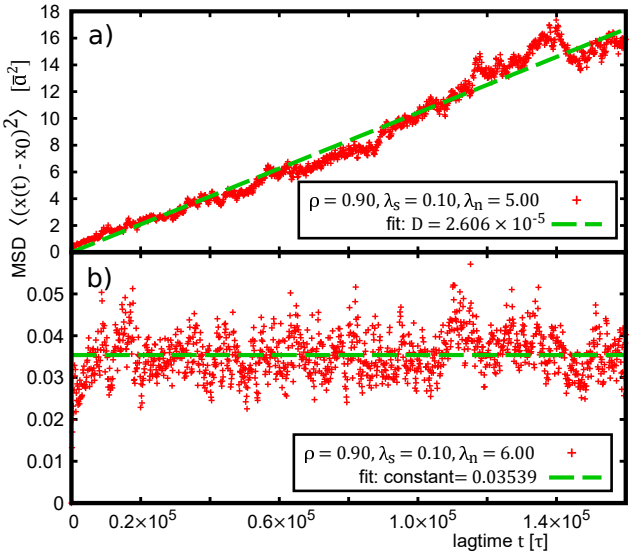

Figure 3.2: Typical mean squared displacement (MSD) graphs of a) an unjammed and b) jammed system. The top panel has parameters $\rho = 0.90$, $\lambda_s = 0.10$, and $\lambda_n' = 5.00$. We fit the diffusion coefficient D with $\mathrm{MSD}(t) = 4Dt$. The bottom panel b) shows an MSD graph for a jammed system at $\rho = 0.90$, $\lambda_s = 0.10$, and $\lambda_n' = 6.00$. We always fit a linear and constant function. The fits with the smallest chi-squared residuals are shown in both cases.

3.2. Phase diagram of jamming

Conventional jamming phase diagrams have density, temperature and load on their axes, following Liu and Nagel. [2]. At zero temperature and without external forces, granular systems will be jammed beyond the famous point J, defined in section 1.1.2. Although temperature and particle activity initially seem very similar, their nature is completely different. Active particles consume energy to move, so energy is not conserved on the particle level. Systems at a density higher than ϕ_J can unjam due to thermal motion or by applying external forces. Our system is driven internally by the particles themselves. The magnitude of this self-propulsion force as well as its direction with respect to neighbouring particles can unjam systems beyond the jamming density.

In figure 3.3 we show the preliminary results from our simulations without noise rescaling. Figure 3.3a is a heatmap of the diffusion coefficient at $\rho = 0.90$ and in figure 3.3b we zoom in around the an expected minimum. We set the diffusion coefficient for jammed systems to 10^{-8}, such that they are represented by a red colour in the heatmap. The gradient is a linear interpolation of $\log(D)$ between the simulations (black dots) and merely serves as a guide to the eye as the noise parameter λ_n does not scale with the value of λ_s. We find unjammed systems even at densities far exceeding the jamming density as long as the particles exert a sufficiently large self-propulsion force. Interestingly, a system can go from jammed, to unjammed and back to jammed along the noise axis. Since this noise is only on the orientation of the particles, and not on its translation, more noise does not

automatically mean that the system is more likely to unjam. In fact, particles lose their orientational persistence when there is too much noise. They cannot push aside their neighbours and therefore will always be trapped between the same set of particles. On the other hand, too little noise causes particles to move in the same direction as their neighbours. We still consider this system jammed for the same reason we call congested traffic a traffic jam. There is a global translation, but locally the cars cannot overtake, i.e. their cage travels with them. The low-noise jammed system is a different phase from the high-noise jammed phase. The two jammed phases are separated by the order-disorder phase transition, which we discuss in section 3.4. Because of the existence of an unjammed phase between two jammed phases, we expect an optimal noise where particles require a minimal self-propulsion force to unjam. The nature of our optimal noise is different than the optima reported by Reichardt and Chepizhko [3, 4]. In both references they find maximized motility of a cluster by optimizing the run-and-tumble frequency or angular noise respectively. Our optimal noise maximizes the motility of particles within clusters.

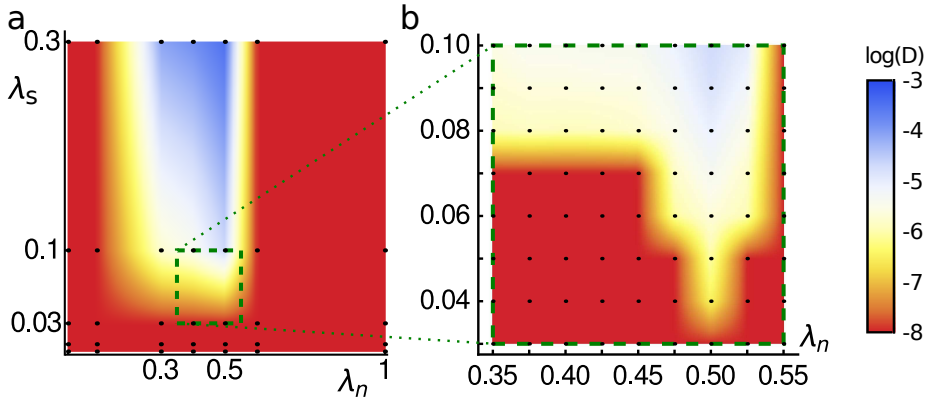

Figure 3.3: Both plots show the value of the diffusion coefficient as a function of λ_s and the unscaled noise λ_n. The preliminary results show that even at densities far exceeding ($\rho = 0.90$) the jamming density for passive particles, systems can still unjam. a) The transition from jammed (red area), to unjammed (blue area), back to a jammed system with λ_n at constant λ_s implies an optimal noise for unjamming. The colour indicates the value of the log of the diffusion coefficient. b) We zoom in on the green rectangle of a) and find evidence for an optimal noise for the system to unjam at minimal self-propulsion strength. See also 3.4 for similar plots with correct noise scaling.

To verify that the features described above are not a consequence of the unscaled noise parameter λ_n, I include here the results of Daniel McCusker, who ran simulations using a fixed Δt and a larger system size to decrease the finite size effects. His results are shown in figure 3.4. The colour of the dots corresponds to the value of a diffusion coefficient determined from MSD analysis. Blue dots represent unjammed systems and for red dots, the simulated systems are (marginally) jammed. The line indicates a constant diffusion coefficient that separates the jammed from the unjammed systems. Hence the surface can be thought of as an indication of how

much activity the particles need to unjam the system.

Especially figure 3.4a and b share quantitatively similar features to figure 3.3a. To find a more precise estimate of the optimal noise, Daniel ran additional simulations near the order-disorder transition. The result of these can be found in figure 3.4d, 3.4e, and 3.4f for $\rho = 0.88$, $\rho = 0.92$, $\rho = 1.00$ respectively. Determining the exact location of the minimum is difficult with the current number of simulations, given the noisiness of the MSD, however they strongly suggest enhanced motility near $\lambda_n = 0.465$ (or $\lambda_n' = 1.47$).

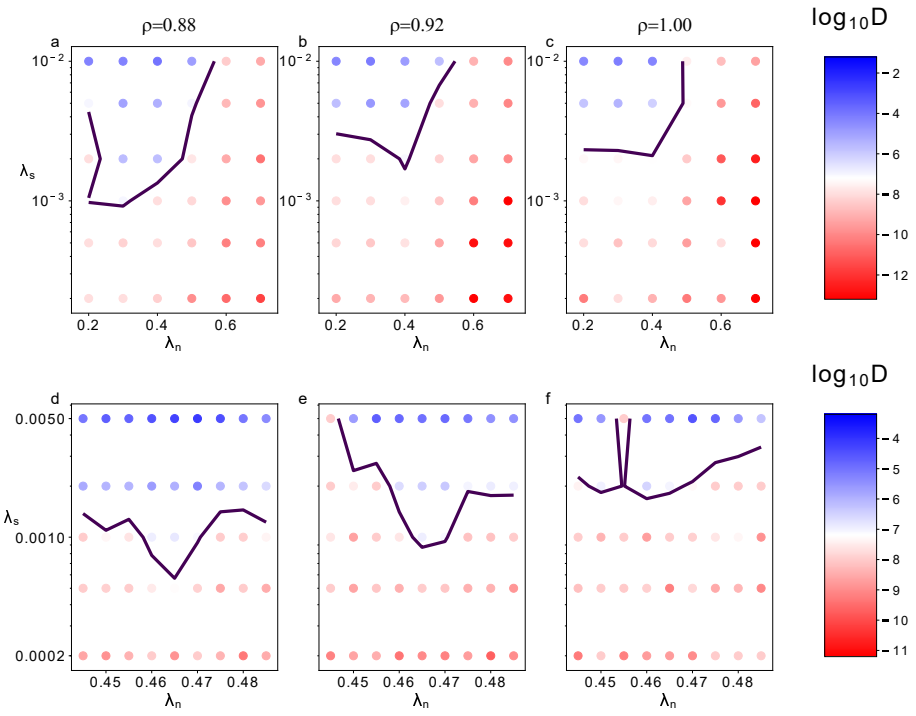

Figure 3.4: The value of the diffusion coefficient, D, from mean-squared displacement analysis for different values of λ_s and λ_n at constant Δt for a) $\rho = 0.88$, b) $\rho = 0.92$, and c) $\rho = 1.00$. The colour of each dot corresponds to the value of $\log(D)$. Blue represents unjammed systems and red represents jammed systems. The line drawn at constant $D = 5 \times 10^{-7}$ is a result of a linear interpolation and can be interpreted as a rough indication for the self-propulsion strength needed to unjam a system at a given noise. Figures d), e) and f) are results from simulations ran near the order-disorder transition near $\lambda_n \approx 0.47$ (or $\lambda_n' \approx 1.49$) (see figure 3.5c and d). The simulations strongly suggest enhanced motility near $\lambda_n = 0.465$ (or $\lambda_n' = 1.47$).

3.3. The contact number

Studies on jamming often measure the contact number, z. The contact number is the number of particles that the average particle touches. At very low densities, particles will not be forced to touch each other and the contact number will be

$z \approx 0$. With increasing density, the contacts will start to inhibit the motion of a particle. We can derive the average number of contacts for each particle that will cause the system as a whole to be jammed with a simple argument. Suppose we have a system of N particles in d dimensions that is exactly at the jamming density. There are Nd unknowns in our system, i.e. we would need to specify Nd variables to fully characterize this system. In this jammed system, particles are not able to move. That means that the number of equations constraining this system equals the number of unknowns. If on average, each particle has z contacts, then the total number of contacts will be $Nz/2$. For frictionless spherical particles, each contact yields one independent (force) equation. Hence, equating the number of unknowns to the number of equations gives $Nd = Nz/2$. Therefore, particles in such systems will, on average, have $z = z_{\text{iso}} = 2d$ contacts. This condition is called isostacity. Systems that exactly satisfy the isostatic condition are called marginally jammed. If one were to break only a single contact, this system would unjam. In jammed systems, the contact number will exceed two times the number of dimensions.

In all our simulations we found a contact number higher than $z = 4.5$. However, we did see rearrangements for some sets of parameters. The activity of the particles themselves allow for a larger contact number before they jam. Furthermore, the self-propulsion force makes these particles anisotropic, changing the number of equations and unknowns. Our simple argument to determine z_{iso} no longer applies. However, in the limit of no self-propulsion force, we would find that $z_{\text{iso}} = 4$. Therefore, we expect the isostatic condition to be dependent on the self-propulsion force. This behaviour, where the isostatic contact number changes with a parameter, reminds of the behaviour reported by Donev et al. [5], who showed that z_{iso} increases with ellipticity. As a consequence, there is no single value of the contact number that can clearly distinguish between jammed and unjammed states. The systems we classified as unjammed generally did have a lower contact number, however there was no one-on-one correspondence. In conclusion, we found the contact number not to be a useful metric to distinguish between jammed and unjammed systems.

3.4. Critical behaviour and giant number fluctuations

Figure 3.5 shows the relation between the unscaled noise parameter λ_n and the Vicsek order parameter defined in equation 3.5. We observe that the order parameter is not dependend on the self-propulsion strength of the particles, and therefore we have taken the average over multiple values of λ_s. On a linear scale (figure 3.5a), the order vanishes above a critical noise. This behaviour is reminiscent of a second order phase transition in equilibrium systems. Although phase transitions are historically equilibrium phenomena, it is widely expected that phase transitions also occur in out-of-equilibrium systems. For example, Flenner et al. [6] recently showed that the glass transition in systems of active, but non-aligning particles has a lot of similarities with the glass transition in thermal systems. And for the Vicsek model, Chaté et al. [7] showed that the transition is a first order transition. Using the preliminary result, we fit a powerlaw of the form $\phi \sim (\lambda_c - \lambda_n)^\nu$ to the data in figure 3.5. The dashed line corresponds to a fit with $\lambda_c = 0.534 \pm 0.003$ and $\nu = 0.40 \pm 0.01$. In figure 3.5b we plot the same data on a $\log - \log$-scale. The critical

point and exponent we find for finite sized particles are consistent with the work by Czirok et al. [9] on point-like particles.

We also include the results of Daniels simulations in figures 3.5c and d. He simulated with more particles ($N = 5 \times 10^4$), and as a consequence, finds slightly different values for the critical point and critical exponent. In the next paragraph we will explain why the number of particles affects the location of the critical point.

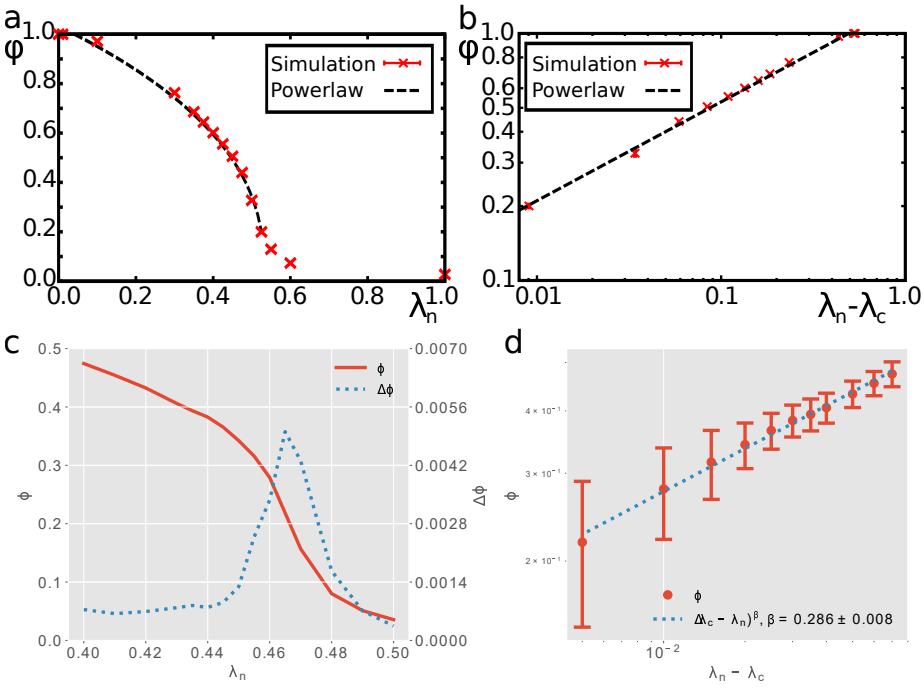

Figure 3.5: Dependence of the Vicsek order parameter ϕ on orientational noise λ_n for $N = 16,384$ particles at $\rho = 0.90$ and averaged over all simulated values of λ_s. The data in a) suggests a critical point near $\lambda_n = 0.5$. Consequently, we fitted a powerlaw (dashed line): $\phi \sim (\lambda_c - \lambda_n)^\nu$, with $\lambda_c = 0.534 \pm 0.003$ and $\nu = 0.40 \pm 0.01$. In figure b) we plot ϕ versus $\lambda_c - \lambda_n$ on a log-log scale and find that the data indeed falls on a straight line. c) and d) are similar plots to a) and b) with the difference that these are the result of simulations with five times more particles. With more particles, the transition occurs at $\lambda_c \approx 0.47$ with a critical exponent $\nu = 0.286 \pm 0.008$. The infinite order of the order-disorder transition likely causes the difference between the top and bottom plots.

We have been comparing our results on the order parameter and its critical behaviour to Vicsek et al. [10] and Cziròk et al. [9]. There is however another model that, at a first glance, shows very similar behaviour. The rotational analogue of the Ising model, the xy-model, also has an order-disorder transition. In that model, spins are arranged on a fixed lattice, and are allowed to rotate in the plane. Just as in the Ising model, there is an energy penalty for misaligning. Temperature causes imperfect alignment between neighbours, and beyond a critical temperature the lattice

changes from ordered to disordered. This transition is called the Kosterlitz-Thouless transition. There are however fundamental differences between the point-like Vicsek model and the xy-model. In the Vicsek model, the particles are moving, whereas in the xy-model they are stuck to their lattice site. This difference has some important implications. In particular, the xy-model, being a thermal equilibrium system, has to abide the Mermin-Wagner theorem. This theorem states that continuous symmetries cannot be broken by finite temperature fluctuations in a 2D system with short-range interactions. Hence, the theorem implies that long-range fluctuations require very little energy. Therefore, in the xy-model, there can be no true long-range order and the phase transition that we observe is said to be of infinite order. In contrast, the Vicsek model does have a state of true long-range order. The Vicsek model is not an equilibrium system and therefore it is not bound by the Mermin-Wagner theorem. Toner and Tu [11, 12] showed using a field theory of the Vicsek model that density fluctuations allow for a fast transfer of information that ultimately leads to long-range order. The colour gradients in figure 3.1a show that we indeed have density fluctuations. To see whether fast information transfer could be possible in our model, we quantify the density fluctuations. We use a method similar to that of Chaté et al. [13], who measured the number density on various scales over time. We calculate the density (or packing fraction) in concentric circles of increasing size around each particle. For each particle we then get a density in a circle of radius r. We find the average density $\langle A \rangle$, by taking the average over all N circles of the same size. We also compare the deviation from this average for each of the N circles to calculate $\Delta A_{\text{rms}} = \sqrt{\langle \Delta A^2 \rangle}$. Obviously, since our simulated system has a finite size, we can only identify fluctuations on the scale of up to $\langle A \rangle = 500\bar{a}^2$ or $r \approx 12.65\bar{a}$ for the radius of the circle. Beyond that size, the finite size effects of our system become important.

In figure 3.6, we plot the relation between $\langle A \rangle$ and ΔA_{rms} for three simulations; unjammed (blue cross), jammed disordered (red asterisk) and jammed ordered (black plus). We also fit a powerlaw, $\langle A \rangle \sim \Delta A_{\text{rms}}^{\alpha}$ for $\langle A \rangle < 500\bar{a}^2$. In the jammed state, interparticle repulsion forces are dominant, resulting in a homogeneous distribution of particles and we don't expect large density fluctuations. Indeed, regardless of the state (ordered or disordered), we find a slope of around $\alpha \approx 1/2$, caused by the randomness of the packing. In the unjammed state for $\lambda_n' = 5.00$, we measure a significantly higher value of α.

The unjammed systems generally have a higher value of α. Unfortunately, this value changes gradually between the jammed and unjammed state, so we cannot use it as a distinguishing measure for jamming (see figure 3.7). Furthermore, the spread is too large to make accurate predictions whether the system is in a jammed state or not.

Our system is a mix of the Vicsek model and the xy-model. In the unjammed state, the particles move, rearrange, and cause density fluctuations. In contrast, in the jammed state, there are no rearrangements and no density fluctuations and therefore at best, only quasi long-range order. We expect the transition between systems that can achieve true long-range order and systems that cannot, to be the jamming transition. Identifying true long-range order may require an enormous

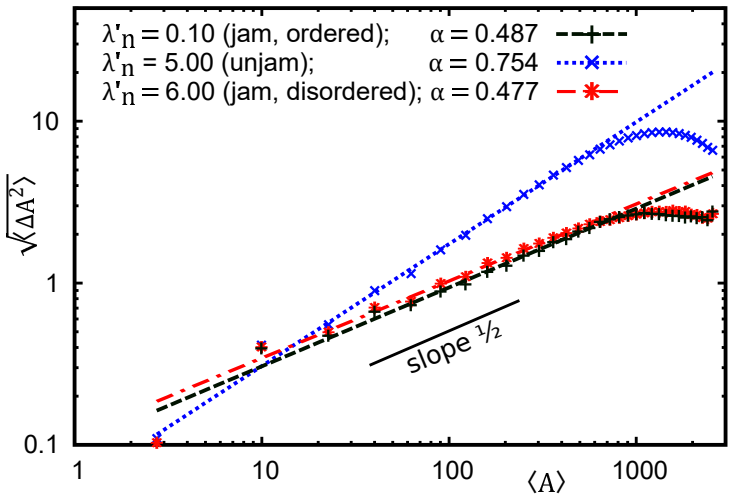

Figure 3.6: We measure the density fluctuations by plotting the the deviation from the mean area versus the mean area at different length scales. Simulations are at $\rho = 0.90$ and $\lambda_s = 0.1$. For the noise parameter we have $\lambda'_n = 0.10$ (black plus, dashed line) for the jammed, ordered state, and $\lambda'_n = 5.00$ (blue cross, dotted line) for the unjammed state, and $\lambda'_n = 6.00$ (red asterisk, dot-dashed line) for the jammed, disordered state. Unjammed states have larger density fluctuations.

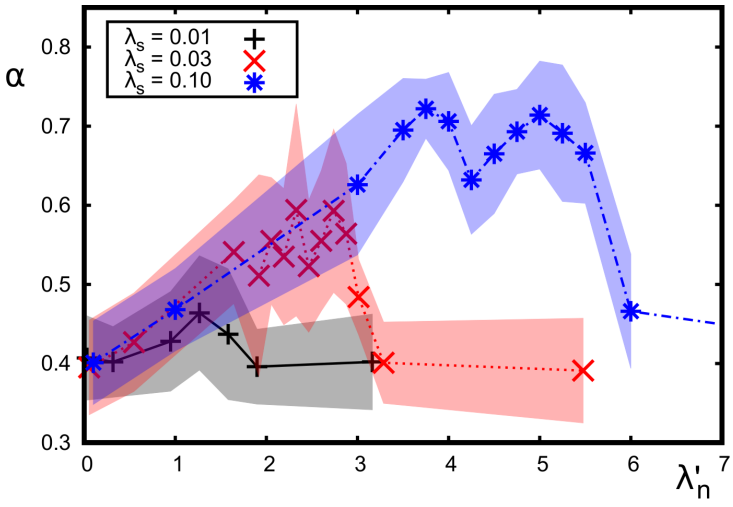

Figure 3.7: The value of exponent α as a function of the noise parameter λ'_n for self-propulsion speeds $\lambda_s = 0.01$ (black plus), $\lambda_s = 0.03$ (red cross), and $\lambda_s = 0.10$ (blue square). The shaded areas in corresponding colours indicate the standard deviation among 10 runs with the same parameters.

number of particles [7]. Therefore we consider our MSD analysis to be the most accurate way to identify jamming.

4. Conclusion

We simulated self-propelled particles at densities exceeding the classical jamming density and find that systems require a combination of alignment and orientational noise to unjam. Too little noise causes all particles to align, and particles will be stuck between their neighbours like in a traffic jam. Too much noise causes the particles to change direction so quickly that they lack the ability to push aside their neighbours. Once again, the particles become trapped in a cage formed by their neighbours. The optimal competition between alignment and noise occurs around $\lambda'_{n,\mathrm{opt}} \approx 1.5$. With a minimal self-propulsion force, the particles are able to create local differences in density. Consequently, rearrangements can occur in the low density regions, ultimately responsible for long-time mixing.

We measure the competition between alignment and noise with the Vicsek order parameter. The transition between the ordered state ($\phi \neq 0$) and the disordered state ($\phi = 0$) could be similar to the order-disorder transition in the Vicsek model. The giant density fluctuations we observe point towards this conclusion. However, we would need to do simulations with many more particles to prove it. Our system could be too small and therefore, the slowed down dynamics due to jamming may inhibit the motion of the particles and make the enhanced information transfer needed for true long-range order impossible.

Acknowledgements

Special thanks go out to Daniel McCusker for continuing the work on this model and for providing me with the results of his simulations. His improvements to the simulations fortify the conclusions based on my early results.

References

[1] D. Vågberg, P. Olsson, and S. Teitel, *Critical scaling of bagnold rheology at the jamming transition of frictionless two-dimensional disks,* Phys. Rev. E **93**, 052902 (2016).

[2] A. J. Liu and S. R. Nagel, *Nonlinear dynamics: Jamming is not just cool any more,* Nature **396**, 21 (1998).

[3] C. Reichhardt and C. J. O. Reichhardt, *Active matter transport and jamming on disordered landscapes,* Phys. Rev. E **90**, 012701 (2014).

[4] O. Chepizhko, E. G. Altmann, and F. Peruani, *Optimal noise maximizes collective motion in heterogeneous media,* Phys. Rev. Lett. **110**, 238101 (2013).

[5] A. Donev, R. Connelly, F. H. Stillinger, and S. Torquato, *Underconstrained jammed packings of nonspherical hard particles: Ellipses and ellipsoids,* Phys. Rev. E **75**, 051304 (2007).

[6] E. Flenner, G. Szamel, and L. Berthier, *The nonequilibrium glassy dynamics of self-propelled particles,* Soft Matter **12**, 7136 (2016).

[7] H. Chaté, F. Ginelli, G. Grégoire, and F. Raynaud, *Collective motion of self-propelled particles interacting without cohesion,* Phys. Rev. E **77**, 046113 (2008).

[8] G. Baglietto, E. V. Albano, and J. Candia, *Criticality and the onset of ordering in the standard vicsek model,* Interface Focus **2**, 708 (2012), http://rsfs.royalsocietypublishing.org/content/2/6/708.full.pdf .

[9] A. Czirók, H. E. Stanley, and T. Vicsek, *Spontaneously ordered motion of self-propelled particles,* J. Phys. A Math. Gen. **30**, 1375 (1997).

[10] T. Vicsek, A. Czirók, E. Ben-Jacob, I. Cohen, and O. Shochet, *Novel type of phase transition in a system of self-driven particles,* Phys. Rev. Lett. **75**, 1226 (1995).

[11] J. Toner and Y. Tu, *Long-range order in a two-dimensional dynamical* XY *model: How birds fly together,* Phys. Rev. Lett. **75**, 4326 (1995).

[12] J. Toner and Y. Tu, *Flocks, herds, and schools: A quantitative theory of flocking,* Phys. Rev. E **58**, 4828 (1998).

[13] H. Chaté, F. Ginelli, and R. Montagne, *Simple model for active nematics: Quasi-long-range order and giant fluctuations,* Phys. Rev. Lett. **96**, 180602 (2006).

4

Collective dynamics and motility of soft elliptical particles

A system which has spherical symmetry, and whose state is changing because of chemical reactions and diffusion ... cannot result in an organism such as a horse, which is not spherically symmetrical.

Alan Turing

Swarming behaviour is abundant in nature. Over many different length scales, in for example herds, flocking birds and swimming bacteria, roughly identical individuals interact locally to achieve group behaviour. The similarities between these examples suggests the existence of a general underlying principle. We propose here a local interaction model for self-propelling, elliptical particles that results in collective motion. Any particle interacts with its neighbours only, experiences noise on its orientation and pushes inwards if it is in the outer layer of the group. Initially, alignment between particles is the result of steric repulsion. We observe two types of group behaviour. The first type is a migrating group, where particles in the bulk are aligned over large length scales, but do not rearrange. The second type has very little net motion. The elliptical particles form smaller regions of aligned and anti-aligned particles, effectively cancelling the net motion of the group. Finally, we compare the group behaviour of elliptical particles to circular ones and investigate the importance of polar alignment. We conclude that polar alignment is a requirement for large-scale collective dynamics, like collective migration and rotation.

This chapter has been published as R. van Drongelen and T. Idema, *Collective dynamics and motility of soft elliptical particles*. In: Knoop, V. L. and Daamen, W. (Eds.) Traffic and Granular Flow '15, 605-612, Springer, 2016.

1. Introduction

Many organisms do not just live by themselves. They live in groups. Such groups consist of hundreds to hundreds of thousands of roughly identical individuals. Examples range over many length scales: herds of mammals, flocks of birds [1] and schools of fish [2, 3], insects [4], and amoebae [5, 6] and bacteria [7]. In all cases, the collective behaviour of the group is the result of interactions between individuals that are close together. Especially on the smallest scale, clusters can reach packing fractions approaching unity. As a general rule, individuals have little knowledge about the dynamics of the group. Still, the behaviour of the group as a whole is obviously important to every individual in it. Therefore, we want to understand how rules between neighbouring individuals govern the group behaviour.

Swarming dynamics are a highly non-linear result of specific local interactions, as can be seen by simulating group dynamics based on simple rules for individuals. For example, the well-known Vicsek model describes a flock of birds as a collection of self-propelled point particles with fixed speed, an interaction that aligns an individual's direction of flight to the velocity of its neighbours, and orientational noise [8, 9]. To prevent the swarm from falling apart, Vicsek et al. originally used unrealistic periodic boundary conditions. Variations of the Vicsek model add a long-range attraction potential or confine the particles by a fixed boundary [10, 11]. Recently, we showed that a system can provide its own boundary by imposing a local outsiders-want-in rule [12] (see also chapter 2 of this thesis). Particles on the boundary will turn towards the group and push inwards, until they are part of the bulk again. In that chapter we focussed on circular particles. Here we extend our results by investigating the effect of anisotropy on the local alignment, and ultimately, the group dynamics.

We model collective dynamics of elliptical particles in viscous environments. In the model, particles repel each other if they overlap, propel themselves along their major axis, experience noise on this direction and push themselves inwards if they are on the outside. All of these are local interactions. We find that the resulting clusters are either collectively aligned without internal dynamics, or dynamic with only local alignment and no net motion. These results are in contrast with the results in chapter 2 on circular particles with polar alignment, which do exhibit global collective dynamics. We also carry out two types of control simulations to investigate if polar alignment, or the geometry of the particles, is responsible for collectively dynamic systems. Our results show that clusters perform collective migration and rotation once we add a polar alignment rule, whereas clusters of circular particles with a nematic alignment will always break up. Indeed, for birds and fish, polar alignment is a clearly visible feature. Cells of the social amoebae *Dictyostelium discoideum* align their velocities and the resulting cluster exhibits collective migration, as well as rotation [13]. The *Myxococcus xanthus* bacteria align through steric interactions, and use velocity reversals to achieve collective migration [14, 15]. In contrast, large groups of whirligig beetles, that align in an apolar way, exhibit no net motion.

2. Model

We consider N identical, self-propelling ellipses with aspect ratio $\gamma = 2:1$ and minor axis σ_0. We denote the position of the centre of ellipse i by $\vec{r}_i$ and its orientation by ψ_i, such that ψ_i is the angle between the major axis and the positive $\hat{\vec{x}}$-axis. Particles propel themselves along their major axis. They are subjected to a viscous drag. We consider the overdamped limit where particles have negligible inertia. Since they mostly move along the direction of self-propulsion, we can approximate our equations of motion from the expressions for the linear and angular drag on disks, reported in Landau and Lifshitz [16] and section 1.1.3. The drag force and torque on particle i are given by

$$\vec{F}_i = \frac{16}{3}\eta\sigma_0\vec{v}_i \equiv \zeta\vec{v}_i \qquad \text{and} \qquad T_i = \pi\eta_R\gamma\sigma_0^2\omega_i \equiv \mu\omega_i. \tag{4.1}$$

In these definitions for ζ and μ, η and η_R are the translational and rotational viscosities, and $\vec{v}_i$ and ω_i are the linear and angular velocity of particle i.

Overlapping particles experience a soft, harmonic, repulsive force, which we model by a modified Gay-Berne potential. The potential, in accordance with the work of Zeravcic et al. [17] on the jamming of soft ellipsoidal particles, is given by

$$V(r_{ij}, \sigma_{ij}) = \begin{cases} \frac{1}{2}k\left(\sigma_{ij} - r_{ij}\right)^2 & \text{for } r_{ij} \le \sigma_{ij} \\ 0 & \text{for } r_{ij} > \sigma_{ij} \end{cases}, \tag{4.2}$$

where k is the spring constant, and $r_{ij} = |\vec{r}_j - \vec{r}_i|$ is the distance between the centres of ellipse i and j. The range parameter σ_{ij} indicates how much two particles overlap. This parameter depends on the relative position of particle i to j, $\vec{r}_{ij}$, and their respective orientations ψ_i and ψ_j. The range parameter is defined by

$$\sigma_{ij} = \sigma_0\left[1 - \frac{\chi}{2}\left(\frac{(\hat{\vec{r}}_{ij}\cdot\hat{\vec{u}}_i + \hat{\vec{r}}_{ij}\cdot\hat{\vec{u}}_j)^2}{1+\chi\hat{\vec{u}}_i\cdot\hat{\vec{u}}_j} + \frac{(\hat{\vec{r}}_{ij}\cdot\hat{\vec{u}}_i - \hat{\vec{r}}_{ij}\cdot\hat{\vec{u}}_j)^2}{1-\chi\hat{\vec{u}}_i\cdot\hat{\vec{u}}_j}\right)\right]^{-1/2}. \tag{4.3}$$

The vector $\hat{\vec{u}}_i = \cos(\psi_i)\hat{\vec{x}} + \sin(\psi_i)\hat{\vec{y}}$ corresponds to the major axis of ellipse i and $\hat{\vec{r}}_{ij}$ is the unit vector pointing from i to j. The dimensionless parameter $\chi = \frac{\gamma^2-1}{\gamma^2+1}$ depends on the aspect ratio γ of the particles. In general, the corresponding force is not along $\hat{\vec{r}}_{ij}$ (see figure 4.1a). Consequently, there is also a torque that leads to local alignment. The force and torque on particle i are the total derivatives of the potential:

$$\vec{F}_i = -\frac{\mathrm{d}}{\mathrm{d}r_{ij}}V(r_{ij},\sigma_{ij})\hat{\vec{r}}_{ij} \qquad \text{and} \qquad T_i = -\frac{\mathrm{d}}{\mathrm{d}\psi_i}V(r_{ij},\sigma_{ij}). \tag{4.4}$$

Following Vicsek et al. [8], we model self-propelled particles with a constant self-propulsion force and noise on the direction. These interactions are described by

$$\vec{F}_i = F_{\text{self}}\hat{\vec{u}}_i \qquad \text{and} \qquad T_i = T_{\text{noise}}\xi_i, \tag{4.5}$$

with F_{self} and T_{noise} the strength of self-propulsion and noise, respectively, and ξ_i is a random number drawn from the set $\{-1, 1\}$ at each time step. Finally, we use

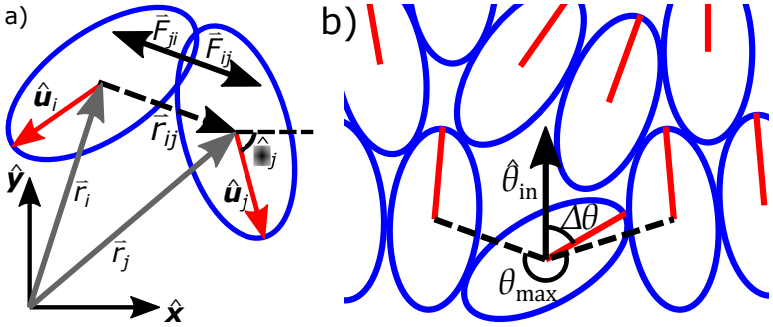

Figure 4.1: a) The repulsive force between particles i and j causes torques on both particles. b) Explanation of the outsiders-want-in-rule. The particle at the bottom identifies itself as a boundary particle by measuring the maximum angular separation between any pair of consecutive neighbours. If this angle exceeds the critical value θ_c, the particle turns inwards and exerts an additional force to squeeze in.

a local boundary term to prevent the system of particles from falling apart. This eliminates the necessity of a geometrical confinement or attraction between particles on either short or long range. To find out if a particle is on the boundary, it measures the largest angle between consecutive neighbours, $\theta_{\text{max},i}$ (see also figure 4.1b). If this angle is larger than the critical value θ_c, this particle will exert an extra force and torque to return to the cluster. The additional force and torque are

$$\vec{F}_i = (\theta_{\text{max},i} - \theta_c)\, F_{\text{in}} \hat{\vec{u}}_i, \qquad \text{and} \qquad T_i = T_{\text{in}} \Delta\theta_i, \tag{4.6}$$

respectively. Again, the strength of these interactions are F_{in} for the force and T_{in} for the torque. The torque is proportional to $\Delta\theta_i$, the angle between the orientation $\hat{\vec{\psi}}_i$ and the inward direction defined by the exterior bisector of angle $\theta_{\text{max},i}$.

We make our variables dimensionless for the purpose of our computer simulation. We fix the length scale by imposing $\sigma_0 = 1$. The characteristic time scale for repulsion is given by $\tau = \zeta/k$. We set the time scale and force scale with $\tau = k = 1$ and denote the duration of one simulation step by Δt. Every other interaction X in our model also has a characteristic time scale τ_X. The strength of the other interactions X will be denoted by $\lambda_X = \tau/\tau_X$. Hence we have i) for the noise, $\lambda_n = \zeta T_{\text{noise}}^2 \Delta t/(2k\mu^2)$, ii) for the additional inwards force, $\lambda_F = 2F_{\text{in}}/(k\sigma_0)$, iii) for the additional inwards torque, $\lambda_T = \zeta T_{\text{in}}/(k\mu)$, and iv) for the self-propulsion $\lambda_s = 2F_{\text{self}}/(k\sigma_0)$. Furthermore we fixed $\mu = 1$, $\theta_c = 0.9\pi$, $\lambda_F = 0.16$ and $\lambda_T = 0.1$.

The model described above consists of finite self-propelled particles with repulsive overlapping interactions. We apply a local boundary term, where particles on the boundary of the cluster push inwards, to keep the cluster together. Both the finite size and the local boundary rule are different from those of the Vicsek model. Finally, in contrast with the Vicsek model, any alignment in the system is the result of steric interactions between the anisotropic particles, instead of being hard-coded into the model. Consequently, ours is the simplest possible model for generating collective behaviour without confinement and long-range interactions.

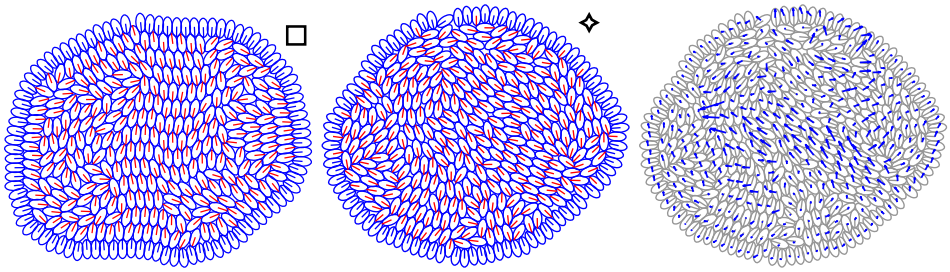

Figure 4.2: Typical snapshots of a) jammed and b) random configurations. In c) we overlaid the velocity field of the random configuration shown in b).

3. Results and discussion

The ellipses are self-propelling agents, which adds properties of polar particles, besides the nemetic properties due to the potential, which is periodic in the angles ψ_i and ψ_j with a period of π instead of 2π. Therefore, we use the order parameter $\phi = \frac{1}{N}\left|\sum_i \hat{\vec{u}}_i\right|$, identical to the Vicsek order parameter, to classify the different types of behaviour that we observe.

3.1. Steady state behaviour of elliptical particles

We investigated the effect of self-propulsion strength and orientational noise on the behaviour of the cluster. We found two distinct types of behaviour, which we will label 'jammed' and 'random'. In the jammed state, particles do not rearrange (see figure 4.2a). The order parameter ϕ is constant in time for periods longer than 5% of the total simulation length and the trajectory of the average position of all particles consists of straight lines or arcs of constant curvature. In the random state the particles swim in small streams contained inside a ring constituted of inward facing boundary particles (see figure 4.2b and c). Particles enter the boundary where the streams hit the boundary. Once they are classified as boundary particles, they turn around and remain part of the boundary until they find a spot where they can enter the bulk again. We observe no global alignment and the value of the order parameter is very low. In short, this state has a mixing dynamics with alignment on short length scales. As a result, the centre of mass of the entire cluster exhibits no net motion.

Not surprisingly, the jammed state occurs when the orientational noise on the particles is low (see figure 4.3a). Introducing increasingly more noise at low or intermediate self-propulsion speeds gradually leads to the random state. For these states to be stable, the self-propulsion speed cannot be too high. A high self-propulsion speed always leads to break-ups into multiple small clusters.

3.2. Motility of clusters of circular versus elliptical particles

In chapter 2, we found that clusters of circular particles with a polar alignment rule exhibit four main types of behaviour: clusters that break up (type 1), jammed clusters with strong alignment (type 2), dynamical clusters where particles rotate

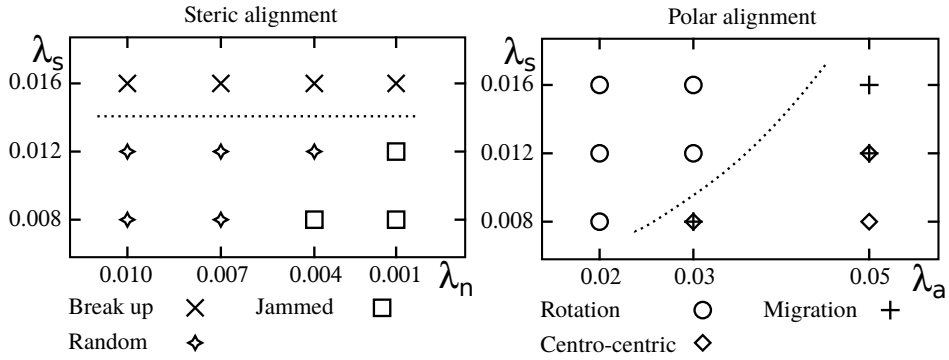

Figure 4.3: State diagrams of a) elliptical particles that align through steric repulsion and b) elliptical particles with the polar alignment rule introduced in Sect. 3.3. On the vertical axis we increase the self-propulsion speed of the particles, and on the horizontal axis we increase the effective alignment between them. We drew dashed lines between states that are topologically different. The symbols are shown in figure 4.2 for steric alignment and figure 4.5 for polar alignment, with their phenotypes.

collectively around a common centre (type 3), and dynamical clusters that migrate collectively (type 4). For the last type, the local alignment results in a global preference for the orientation of the particles. This direction corresponds to the direction of movement of the cluster, which performs a random walk over time.

3.3. Effects of polar alignment and shape on collective dynamics

In contrast to polar circular particles, that display dynamic, collective behaviour of rotating and migrating clusters, we find that clusters of elliptical particles do not achieve global, collective behaviour. This drastic change can only be caused by two factors. First, the geometry of the particles changes the way the particles can arrange in a cluster. Second, we also disposed of the polar alignment rule. After all, the Gay-Berne potential aligns our particles as well, eliminating the need to put alignment in the system as a separate rule. However, this potential also anti-aligns the particles. To determine which effect is responsible for collective behaviour, we tested two different scenarios. In the first, we replaced the steric alignment interaction with a polar alignment rule. Consider for example orientations of i and j that differ by an angle ψ_{ij}, such that $\hat{\vec{u}}_i \cdot \hat{\vec{u}}_j = \cos(\psi_{ij})$, then the torque on particle i is $T_i = T_{\text{align}}\psi_{ij}$. The amplitude of this interaction is T_{align} and we set the strength of the alignment interaction with $\lambda_a = \zeta T_{\text{align}}/(k\mu)$. The second scenario we tested has a nematic alignment, similar to the torque which resulted from the modified Gay-Berne potential, but now for circular particles. For ellipses, the torque depends in a very non-trivial way on the positions of both particles and their orientations. It is impossible to generalize the steric alignment to a nematic alignment for circles. Instead, we choose an alignment torque analogous to the polar alignment rule, but with two stable states, aligned and anti-aligned. In figure 4.4, we plot the torque exerted on particle j as a function of its orientation ψ_j. The nematic alignment torque is a good approximation to the steric alignment torque for elliptical particles

when particle j is located exactly to the side of particle i. In both cases we fixed $\lambda_n = 0.003$, $\lambda_F = 0.06$, and $\lambda_T = 0.3$ in simulations.

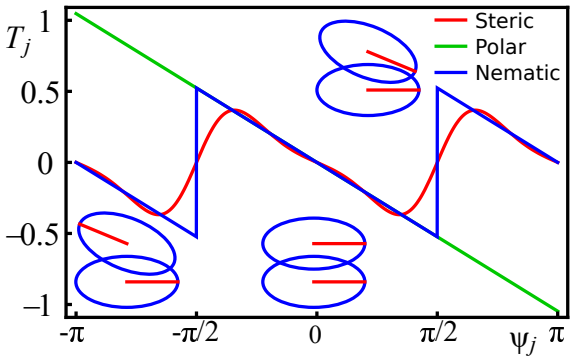

Figure 4.4: The torque exerted on particle j as a function of its orientation for different alignment rules. The steric alignment torque when particle j is located directly above i with orientation $\psi_i = 0$, is shown in red. The torques resulting from the polar alignment rule and the nematic alignment rule are in green and blue respectively.

The results of the first scenario are shown in figure 4.3b and 4.5. We retrieve many of the observed types of behaviour we saw for circles when we reinstate the polar alignment. We find a collective migration state (see figure 4.5b) and a collective rotation state (see figure 4.5c). For collective migration, the location of the orientational defect dictates the movement. When the defect is near the centre of the cluster, the movement will be very slow. In figure 4.5a, we see that the order parameter for this case is $\phi \approx 0$. We call this specific type of behaviour centro-centric. This state is different from a jammed state because we still observe rearrangements and small variations in the order parameter. For higher speeds the defect moves to the edge. At the highest self-propulsion speed we simulated, a small rotation centre forms in the place of the defect. The collective movement is still in the direction of this rotation centre and is ultimately responsible for a random walk of the cluster. In all cases, the order parameter is significantly lower ($\phi \lessapprox 0.3$) than it was for circles ($\phi > 0.3$). Consequently, the absolute speed of the cluster is lower as well.

In agreement with clusters of circular particles, clusters of elliptical particles will rotate for low values of the alignment parameter (see figure 4.3b and figure 4.5c). There is a clear difference between rotating and migrating clusters phenotypically. The distinction between centro-centric and actual migration is not as clear. Rather than a sharp boundary between the two types of behaviour, we observe a gradual change, where the order parameter monotonically increases with the alignment and the self-propulsion parameter, λ_a and λ_s, respectively. Compared to steric alignment, the cluster can still break up, but only for large λ_s (not shown in the state diagram). Similarly, the polar alignment system will jam only for large λ_a.

Surprisingly, the nematic alignment rule applied to circular particles (scenario 2) made the steady state behaviour unstable. In all cases, the cluster broke up into multiple clusters. There are two reasons why circular particles with nematic alignment are different from elliptical particles with a steric nematic alignment. First, steric alignment still allows for alignment mismatches. For very little overlap, the exerted torque will also be small. The anisotropic nature of the particles will create overlap with other particles until all torques are balanced. The result will look like figure 4.2a and b, where we observe mismatches that are stable. Circular

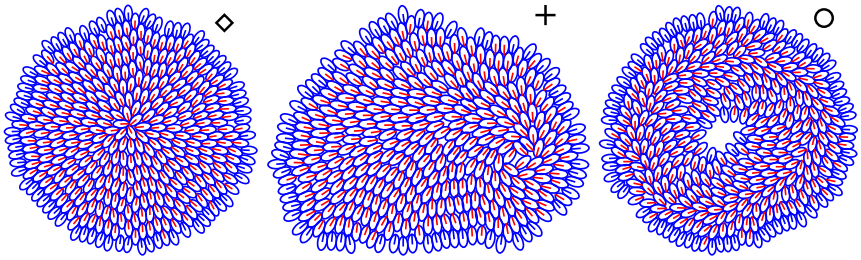

Figure 4.5: Typical snapshots of the simulation for ellipses with polar alignment. We observe a) alignment towards the centre, b) collective migration, and c) rotation.

particles do not create overlap when they rotate, and will therefore always align. Second, the nematic alignment also makes particles turn towards the boundary. If there are more particles pushing out towards the boundary than boundary particles pushing in, the boundary will be pushed out. This will cause the cluster to break up.

4. Conclusion

Anisotropic particles do not automatically swarm with an outsiders-want-in rule. Without polar alignment clusters will break up easily. In addition, for low self-propulsion speeds the particles may be jammed into a configuration with a long correlation length for alignment, or they only align locally such that the net movement of the cluster effectively averages out. Clusters collectively migrate or rotate when particles align their self-propulsion direction. The elongated shape of the particles decreases the value of the order parameter compared to migrating clusters of circular particles. Consequently, clusters of elliptical particles don't move quite as fast as their circular counterparts. Our model suggests that locally interacting organisms in viscous environments, i.e. unicellular organisms and cells, need to communicate their orientation to collectively move.

References

[1] M. Ballerini, N. Cabibbo, R. Candelier, A. Cavagna, E. Cisbani, I. Giardina, V. Lecomte, A. Orlandi, G. Parisi, A. Procaccini, *et al.*, *Interaction ruling animal collective behavior depends on topological rather than metric distance: Evidence from a field study,* Proc. Natl. Acad. Sci. **105**, 1232 (2008).

[2] D. S. Calovi, U. Lopez, S. Ngo, C. Sire, H. Chaté, and G. Theraulaz, *Swarming, schooling, milling: phase diagram of a data-driven fish school model,* New J. Phys. **16**, 015026 (2014).

[3] K. Tunstrøm, Y. Katz, C. C. Ioannou, C. Huepe, M. J. Lutz, and I. D. Couzin, *Collective states, multistability and transitional behavior in schooling fish.* PLoS Comput. Biol. **9**, e1002915 (2013).

[4] M. Collett, E. Despland, S. J. Simpson, and D. C. Krakauer, *Spatial scales of desert locust gregarization,* Proc. Natl. Acad. Sci. **95**, 13052–13055 (1998).

[5] W.-J. Rappel, A. Nicol, A. Sarkissian, H. Levine, and W. F. Loomis, *Self-organized Vortex State in Two-Dimensional Dictyostelium Dynamics,* Phys. Rev. Lett. **83**, 1247 (1999).

[6] B. Vasiev, F. Siegert, and C. J. Weller II, *A Hydrodynamic model for Dictyostelium discoideum Mound Formation,* J. Theor. Biol. **184**, 441 (1997).

[7] A. Czirók, E. Ben-Jacob, I. Cohen, and T. Vicsek, *Formation of complex bacterial colonies via self-generated vortices.* Phys. Rev. E **54**, 1791 (1996).

[8] T. Vicsek, A. Czirók, E. Ben-Jacob, I. Cohen, and O. Shochet, *Novel type of phase transition in a system of self-driven particles,* Phys. Rev. Lett. **75**, 1226 (1995).

[9] T. Vicsek and A. Zafeiris, *Collective motion,* Phys. Rep. **517**, 71 (2012).

[10] A. Czirók and T. Vicsek, *Collective behavior of interacting self-propelled particles,* Physica A **281**, 17 (2000).

[11] S. Henkes, Y. Fily, and M. C. Marchetti, *Active jamming: Self-propelled soft particles at high density,* Phys. Rev. E **84**, 040301 (2011).

[12] R. van Drongelen, A. Pal, C. P. Goodrich, and T. Idema, *Collective dynamics of soft active particles,* Phys. Rev. E **91**, 032706 (2015).

[13] C. J. Weijer, *Dictyostelium morphogenesis.* Curr. Opin. Genetics Dev. **14**, 392 (2004).

[14] S. Thutupalli, M. Sun, F. Bunyak, K. Palaniappan, and J. W. Shaevitz, *Directional reversals enable myxococcus xanthus cells to produce collective one-dimensional streams during fruiting-body formation,* J. R. Soc. Interface **12**, 20150049 (2015).

[15] Y. Wu, A. D. Kaiser, Y. Jiang, and M. S. Alber, *Periodic reversal of direction allows myxobacteria to swarm,* Proceedings of the National Academy of Sciences **106**, 1222 (2009).

[16] L. D. Landau and E. M. Lifshitz, *Fluid Mechanics* (Butterworth-Heinemann, Oxford, 1987).

[17] Z. Zeravcic, N. Xu, A. J. Liu, S. R. Nagel, and W. van Saarloos, *Excitations of ellipsoid packings near jamming,* EPL (Europhysics Letters) **87**, 26001 (2009).

5

On measuring shear stress in aligning, active particle systems

Negative results are just what I want. They're just as valuable to me as positive results. I can never find the thing that does the job best until I find the ones that don't.

Thomas A. Edison

Science is the gathering and structuring of knowledge. We do science to understand elusive processes in the world around us. We come up with hypotheses based on previous knowledge or intuition and test them with experiments and simulations or we prove them theoretically. When someone learns something new from his or her results, that person will typically publish the methods and the results. Unfortunately, quite often the thing we are trying to understand turns out to be more complex than we initially expected, and the methods we used to test the hypotheses may not answer the questions we had. In this case the result is that the thing we are studying does not follow our current scientific way of thinking. This result is a negative result. Negative results are hardly published, and therefore, this knowledge about what does not work, remains the lab.

In this chapter I report my attempts to study jamming in active particle systems by observing the stress response upon applying shear strain. In the end, I concluded that shearing with Lees-Edwards boundary conditions is incompatible with particles that self propel and align their orientation to either the average orientation of their neighbours, or the direction they are pushed in.

1. Introduction

Granular materials have the interesting property that, depending on conditions like density, temperature and load, the material either behaves like a solid or like a liquid [1]. Initially, numerical studies investigating the liquid-solid transition focussed on the density parameter at zero temperature. Olsson and Teitel determined that this new type of phase transition is a second order phase transition at a critical density, referred to as point J [2]. The exact nature of the other transitions (along the temperature axis and load axis) is still a subject of intense debate (see chapter 1). Instead of a temperature or load, we introduce an active component to the particles in our system. The extra energy that particles themselves introduce to the high density packing should shift the jamming density to a higher value. In this study we hope to describe the jamming transition for active particles in similar way to [2–4].

We are interested in the properties of our system of self propelling and aligning particles at high density. In experiments, granular materials are probed with a shear rheometer. There are many types of shear rheometers. To explain the concept, we will consider here a two dimensional linear shear rheometer, consisting of two parallel plates a distance L apart. The object to be sheared is placed in the rheometer such that it makes contact with both plates. We take the bottom plate to be stationary and move the top plate by a distance ΔL. This type of deformation is called shear. We can quantify the amount of deformation by the shear strain γ. For normal strain to linear order, we have

$$\gamma = \frac{\mathrm{d}u_y}{\mathrm{d}x} + \frac{\mathrm{d}u_x}{\mathrm{d}y}, \tag{5.1}$$

where u is applied displacement. Our linear rheometer only deforms the material in one direction. Therefore we have $\gamma = \Delta L/L$. We measure the force that is necessary to deform the material. Since this a force applied on the plate, or equivalently the surface of the material, it is conventional to talk about the stress, instead of the force. We obtain the stress, σ, by dividing the force F by the area on which the force is exerted:

$$\sigma = \frac{F}{A}. \tag{5.2}$$

The stress, depends on the direction of the force relative to the normal of the surface. Hence, the stress is actually a tensor. For now we only consider the shear stress of our linear rheometer. We will be applying a shear strain to our material. The response we will measure in the stress depends on the material. For example, when we place a block of rubber between the shear plates we will find that the further we try to strain this block, the larger the stress response will be. That is, for solid isotropic materials we find a linear relation between stress and strain[1]

$$\sigma = G\gamma \qquad \text{(for solids)}. \tag{5.3}$$

Here G is a material property known as the shear modulus. Note that the rate at which we deform the block of rubber is not important. The stress will be the

[1] Provided the deformations are small enough.

same whether we strain very slowly or very fast, as long as the total strain γ is the same. Another defining property of solids is that the object will return to its original shape when we lift the shear forces on it. This response is in strong contrast with the response of fluids. Suppose we put a viscous fluid, e.g. honey, in the rheometer. If we apply a strain now, the fluid will flow. If we lift the shear forces, the fluid will not flow back. Moreover, we find that it matters how fast we shear. Viscous fluids will resist flow for large deformation rates. For small deformation rates, the fluid will flow relatively easily. Therefore, in liquid we have

$$\sigma = \eta\dot{\gamma} \qquad \text{(for liquids)}, \tag{5.4}$$

where η is the viscosity of the fluid, and $\dot{\gamma}$ is the rate of deformation, or strain rate. By straining granular packings at various strain rates $\dot{\gamma}$, we can distinguish solid-like behaviour from liquid-like behaviour resulting in either a constant stress or linear stress.

2. The model

The model presented here is a modification of the model described in chapter 2. To recall, there are N soft particles that interact through a simple harmonic potential that prevents overlap. The radii of these particles are drawn from a Gaussian distribution with mean $\mu = \bar{a}$ and standard deviation $\sigma = \bar{a}/10$. All particles propel themselves along their direction of orientation. The particles align their own orientation with the average orientation of their neighbours.

2.1. Lees-Edwards boundary conditions

We are interested in the properties of our system of self propelling and aligning particles at high density. To probe these properties we will measure the response of our system to a shear strain, γ. We will use Lees-Edwards boundary conditions, to impose a strain on the system. Lees-Edwards boundary conditions are similar to double periodic boundary conditions. Copies of the simulation box are used as a tilling around the original. However, in Lees-Edwards boundary conditions, the copies below and above the original shift a little bit to the left and right, respectively, each simulation step (see figure 5.1). If we impose a strain rate $\dot{\gamma}$ on a simulation box of dimensions $L \times L$, the top (and bottom) copies and the particles in them have a horizontal velocity $v_x = \dot{\gamma}L$ (and $v_x = -\dot{\gamma}L$). However, shearing also affects the fluid the particles are emerged in. The flow pattern of the fluid between two shear plates is called Couette flow or affine flow. The horizontal velocity increases linearly with vertical position component. The velocity at vertical position y is

$$\vec{v}(y) = v_{\text{aff}}(y)\hat{x} = \dot{\gamma}L(y/L)\hat{x} = \dot{\gamma}y\hat{x}, \tag{5.5}$$

where $v_{\text{aff}}(y)$ is the magnitude of the velocity of the affine flow. The affine flow velocity will enter our equation of motion.

We consider the regime of low Reynolds number, i.e. viscous forces dominate inertial forces. With a contribution from the affine flow velocity, the equations of

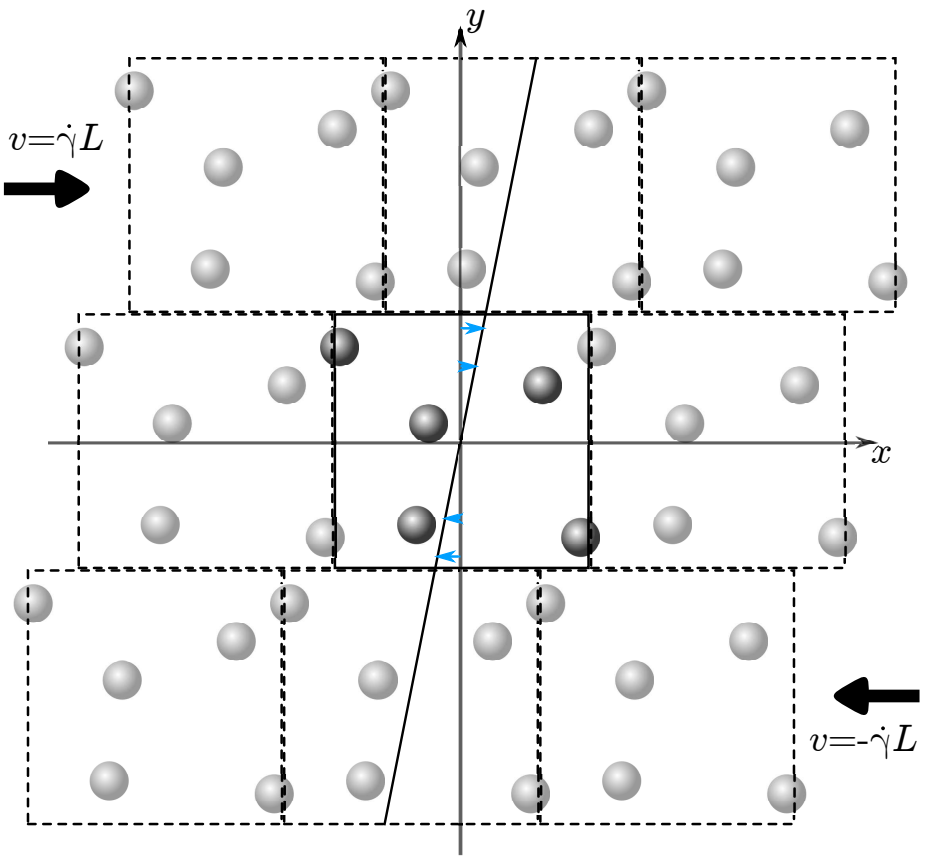

Figure 5.1: Schematic representation of Lees-Edwards boundary condition. Eight copies (dashed) surround the original (solid) simulation box. We simulate shearing by moving the top and bottom copies with a velocity set by the strain rate $\dot{\gamma}$. The shear also causes the fluid to flow. The magnitude of the flow is represented by the blue arrows in the original simulation box.

motion are:

$$\vec{F}_i = \alpha_i \zeta (\vec{v}_i - v_{\text{aff},i}\hat{x}) \tag{5.6}$$

and

$$T_i = \alpha_i^2 \chi \omega_i. \tag{5.7}$$

To recall, $\vec{F}_i$ and T_i are the force and torque on particle i respectively. We conveniently rescaled the translational viscosity (η) and rotational viscosity (η_R) to $\zeta \equiv (32/3)\eta\bar{a}$ and $\chi \equiv 4\pi\eta_R\bar{a}^2$. The factor $\alpha_i = a_i/\bar{a}$ is a dimensionless number that we introduce to make the rescaled viscosities independent of the particles' size. Finally, $\vec{v}_i$ is the linear velocity and ω_i the angular velocity of particle i.

The net forces and torques, which are exerted on each particle, are similar to those in chapter 2. The soft particles repel each other with a force proportional to their linear overlap d, and a spring constant k. Particles propel themselves along their direction of orientation. We can make two choices for the self propulsion strength. Either we take the self propulsion strength to be constant, or we let the self propulsion strength depend on the strain rate. For a constant self propulsion strength we use the same dimensionless parameter, $\lambda_s = F_{\text{self}}/k\bar{a}$, we introduced in chapter 2. The disadvantage of this choice is that we will strain our system with strain rates spanning multiple orders of magnitude. Displacements due to the constant self propulsion force quickly either dominates over, or are dominated by the displacements due to the shear strain. Alternatively we can choose our self propulsion speed relative to the velocity of the copies above and below the original simulation box. Therefore in the second scenario, we set the self propulsion force with a parameter representing the relative velocity: $\beta = F_{\text{self}}/\zeta\dot{\gamma}L$. For $\beta < 1$, displacement by the shear force is dominant, for $\beta > 1$, the displacement by its own self propulsion dominates the displacement of the particle. The downside here is that we effectively strain different systems at different strain rates. Comparing simulations at different strain rates may be difficult.

Besides these forces, torques rotate the particles around their centre. They align their orientation to the average of their neighbours. The torque T that rotates the particle is proportional to the mismatch $\Delta\theta$ between this local director and its own orientation: $T = T_{\text{align}}\Delta\psi$. We found in chapter 2 that we can set the magnitude of this torque with a dimensionless parameter $\lambda_a = \zeta T_{\text{align}}/k\chi$. Particles also experience a bimodal noise on their orientation. We model this by applying a random (positive or negative) torque of magnitude T_{noise} on each particle. We can set the strength of the noise with the parameter $\lambda_n = \zeta T_{\text{noise}}^2\Delta t/2k\chi^2$. The difference with chapter 2 is that the periodic boundary conditions effectively remove the boundary. We can therefore drop the special rules for boundary particles. The Lees-Edwards boundary conditions allow us to study the jamming and unjamming properties of the bulk of the colonies reported in chapter 2.

2.2. The shear stress in discrete systems

In analogy with the work of Tighe et al. [4], we will measure the stress response at various strain rates to distinguish jammed from unjammed systems. Tighe et al. have shown that passive particle systems have a shear stress response more or less independent of the strain rate, whereas in unjammed systems, the shear stress depends linearly on the strain rate. This change in behaviour occurs at a critical density commonly referred to as point J. Rather than a density, people often use the packing fraction ϕ. The packing fraction is simply the ratio between volume occupied by the particles and the available area in the simulation box. The critical packing fraction for circular particles in two dimensions is approximately $\phi \approx 0.843$. The precise value depends on the distribution of particle sizes [5]. In this section we will derive the shear stress reported in among others [4, 6, 7].

Although our equation of motion is very different from theirs, we can calculate the off-diagonal components in the exact same way. We start by noting that in

an over-damped environment, by definition, the resultant force on each particle vanishes. This becomes clear when we rewrite our equation of motion as

$$F_{\text{repulsion},i} + F_{\text{self proulsion},i} - F_{\text{drag},i} = 0. \tag{5.8}$$

The definition of the stress tensor, σ, using Einsteins summation convention, reads

$$F_\alpha = \frac{\partial}{\partial x_\gamma}\sigma_{\alpha\gamma}.$$

When the forces on each particle vanish because of the over-damped environment, the equation above reduces to

$$0 = \frac{\partial}{\partial x_\gamma}\sigma_{\alpha\gamma}. \tag{5.9}$$

We can solve equation 5.9 for the stress tensor, σ, using a small trick. First, we multiply both sides by the β-component of a position vector x, whose physical meaning will become apparent later. The resulting formula holds for every volume element $\mathrm{d}V$. Therefore, we can write

$$\int_V x_\beta \frac{\partial}{\partial x_\gamma}\sigma_{\alpha\gamma}\,\mathrm{d}V = 0. \tag{5.10}$$

Next, we use integration by parts to obtain

$$\int_V \frac{\partial}{\partial x_\gamma}(x_\beta\sigma_{\alpha\gamma}) - \delta_{\beta\gamma}\sigma_{\alpha\gamma}\,\mathrm{d}V = 0. \tag{5.11}$$

The final term defines the average stress per unit volume $\bar{\sigma}_{\alpha\beta} = \frac{1}{V}\int_V \sigma_{\alpha\beta}\,\mathrm{d}V$. After rearranging we find

$$\begin{aligned}
\bar{\sigma}_{\alpha\beta} &= \frac{1}{V}\int_V \sigma_{\alpha\beta}\,\mathrm{d}V = \frac{1}{V}\int_V \frac{\partial}{\partial x_\gamma}(x_\beta\sigma_{\alpha\gamma})\,\mathrm{d}V \\
\bar{\sigma}_{\alpha\beta} &= \frac{1}{V}\oint_{\partial V} x_\beta\sigma_{\alpha\gamma}\hat{n}_\gamma\,\mathrm{d}S \\
\bar{\sigma}_{\alpha\beta} &= \frac{1}{V}\oint_{\partial V} x_\beta\mathcal{F}_\alpha\,\mathrm{d}S.
\end{aligned} \tag{5.12}$$

In the first step we applied Gauss's theorem to rewrite the volume integral to an integral over the surface ∂V of V. The unit vector $\hat{n}$ is perpendicular to the surface element $\mathrm{d}S$. The inner product of the stress tensor and this unit vector is the force, $\mathcal{F}$, on the surface element. The interpretation of this force, and the position vector x is that the force is exerted on the boundary ∂V, a distance x from the centre of the system. Rather than calculating the forces across the boundary of our system, we partition our system into disjunct areas. The total stress is simply the sum of the stresses in all these partitions.

$$\sigma_{xy} = \frac{1}{N}\sum_i^N \bar{\sigma}_{xy,i}. \tag{5.13}$$

Since we have N particles in our volume V, we create N partitions. This could be done for example by a Voronoi tessellation, but the exact tiling does not matter as long as the individual tiles do not overlap and leave no gaps. The only force acting on the boundary of the cell in our system is the repulsive force. Therefore, the repulsive force between particles is the only force contributing to the stress. Body forces, which pull on the centre of the cell, cannot generate stress directly, however they can generate stress indirectly via the repulsive force. For example, when two overlapping particles feel different body forces, they change the amount of overlap, leading to a different repulsive force. Both the self propulsion and the drag force are examples of such a body force.

Now we have all the tools to calculate the stress in our simulations. We replace the integral in equation 5.12 by a sum over all the neighbours j of i. We denote the set of neighbours of particle i by $\mathcal{N}_i$. The total stress then becomes

$$\begin{aligned}\sigma_{xy} &= \frac{1}{V}\sum_{i}^{N}\sum_{j\in\mathcal{N}_i} x_{ij,y} f^{\mathrm{el}}_{ij,x} \\ \sigma_{xy} &= \frac{1}{V}\sum_{\langle ij\rangle} r_{ij,y} f^{\mathrm{el}}_{ij,x},\end{aligned} \tag{5.14}$$

where the final summation runs over all neighbour pairs $\langle ij\rangle$ that have a non-zero overlap. Notice that the double summation in the first line counts every contribution double. The y-component of the distance to the edge of the cell, r_y, lies exactly half way the distance between the centres of cells i and j, so $r_{ij,y} = 2x_{ij,y}$, which compensates for the factor 2 we introduced by changing the summation. Finally, $f^{\mathrm{el}}_{ij,x}$ is the x-component of the elastic force (per unit volume) the particles exert on each other. In Appendix A we show that torques do not contribute to the stress tensor.

3. Results

First, we consider the scenario where particles use a self propulsion speed that is proportional to the strain rate. In chapter 2, we see dynamic colonies at very high density. For those colonies we did not set the density as a simulation parameter, nor is it clear how we can define a packing fraction for those clusters. However, simulation snapshots strongly suggest that the density corresponds to a packing fraction well above point J. Therefore, in this chapter, we do simulations at packing fractions $\phi = 0.90$, $\phi = 0.95$, $\phi = 1.00$, and $\phi = 1.05$. We choose values for λ_a and λ_n identical to the values we used in chapter 2, that is, $\lambda_a \in \{0.10, 0.14, 0.20, 0.30, 0.45, 0.67, 1.00\}$, and $\lambda_n = 0.03$. Simulations run for a total of 2×10^8 steps until the total strain reaches $\gamma = 20$. We apply a strain rate over several orders of magnitude: $\dot\gamma \in \{3\times10^{-6}, 1\times10^{-5}, 3\times10^{-5}, 1\times10^{-4}, 3\times10^{-4}, 1\times10^{-3}, 3\times10^{-3}, 1\times10^{-2}\}$.

In figure 5.2 we plot the simulation data for several values of the relative velocity β, the alignment parameter λ_a, and strain rate γ. We notice immediately that most of our data points do not fall on a straight line. Initially, increasing the strain rate

always leads to a higher stress response. However, we find in most cases that the stress decreases at higher strain rates. This effect is more pronounced for particles for which the mutual alignment is weak. We also see that when particles move faster relative to the strain rate, the stress starts decreasing at lower strain rates. At the same time, the errorbars for the stress increase. The errorbars indicate the standard deviation from five independent runs.

In contrast to Tighe et al. [4], none of our data sets form a straight line on a log-log scale in the stress versus strain rate plots. Therefore, the stress strain rate relation does not follow a power law. For most datasets, the stress decreases beyond some value of $\dot{\gamma}$. However, for relatively low self propulsion speed ($\beta = 0.5$) and strong alignment ($\lambda_a = 0.67$) in panel **a)**, the stress strictly increases. For this dataset, the curve is actually convex on a log-log scale, hence it is not a power law either. A second difference with Tighe et al. is that even though we vary the strain rate over almost four orders of magnitude, the measured stress differs by a factor of just three at best.

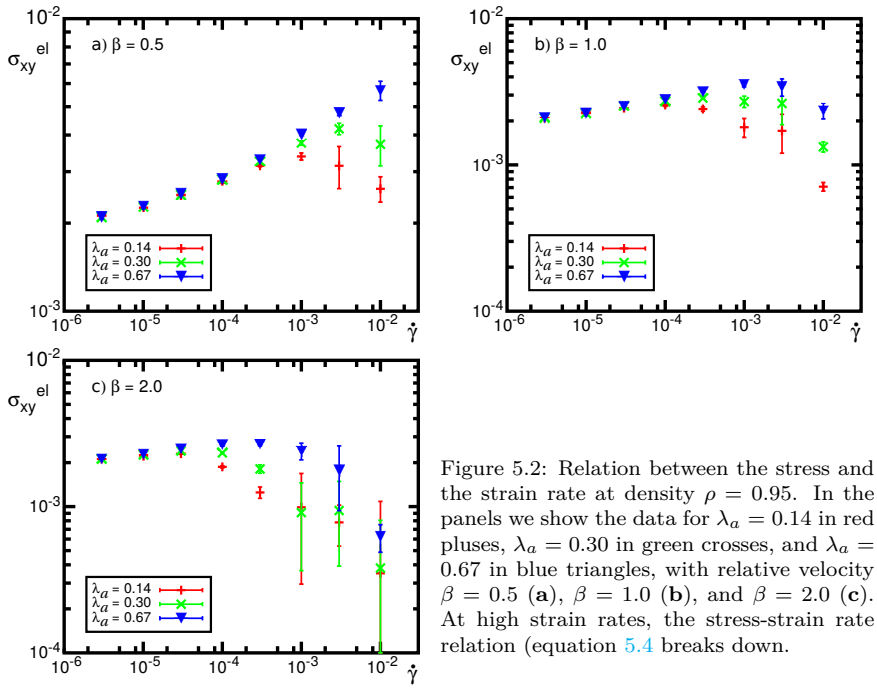

Figure 5.2: Relation between the stress and the strain rate at density $\rho = 0.95$. In the panels we show the data for $\lambda_a = 0.14$ in red pluses, $\lambda_a = 0.30$ in green crosses, and $\lambda_a = 0.67$ in blue triangles, with relative velocity $\beta = 0.5$ (**a**), $\beta = 1.0$ (**b**), and $\beta = 2.0$ (**c**). At high strain rates, the stress-strain rate relation (equation 5.4 breaks down.

To elucidate why the stress decreases at high strain rates, we show snapshots of the simulation in figure 5.3. In figure 5.3a all particles are more or less aligned with an orientation towards the right (indicated by the direction of the radius). The velocity field of the fluid which the particles are immersed in follows a Couette flow, dragging the particles with it. The Couette flow, superimposed with the particles own velocity', is indicated by the red triangular arrows (rescaled by the strain rate). A larger velocity corresponds to a larger triangle. The particles at the bottom have

higher velocity, because they are swimming in the same direction as the strain, whereas for particles at the top the Couette flow and the particle's own velocity point in opposite directions. After some time, the imposed strain causes sudden rearrangements, with large instantaneous velocities and streamlines (see figure 5.3b). In figure 5.3c, we show a snapshot of a simulation with a high strain rate. As a result of our implementation of self propulsion, the self propulsion force of the particles is also much larger. This allows colliding particles to overlap more locally. Consequently, we start seeing density gradients and even voids in the system. The stress response for these systems decreases and becomes noisier with higher strain rates (figure 5.2). The increased noise is presumably caused by particles colliding at random times in near head-on collisions, hence creating a significant overlap. We indeed observe that the power law stress response breaks down at lower strain rates for particles with little alignment ($\lambda_a = 0.14$) than for strong alignment ($\lambda_a = 0.67$). The biggest obstacle however is that a self propulsion velocity proportional to the strain rate cannot be described by a power law.

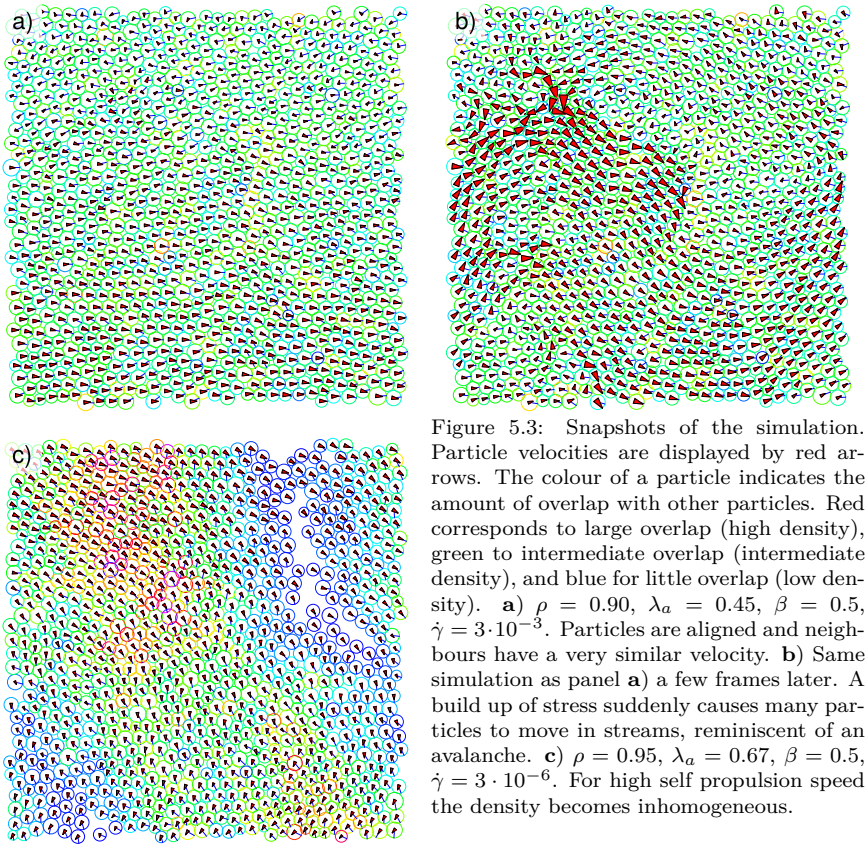

Figure 5.3: Snapshots of the simulation. Particle velocities are displayed by red arrows. The colour of a particle indicates the amount of overlap with other particles. Red corresponds to large overlap (high density), green to intermediate overlap (intermediate density), and blue for little overlap (low density). **a**) $\rho = 0.90$, $\lambda_a = 0.45$, $\beta = 0.5$, $\dot{\gamma} = 3{\cdot}10^{-3}$. Particles are aligned and neighbours have a very similar velocity. **b**) Same simulation as panel **a**) a few frames later. A build up of stress suddenly causes many particles to move in streams, reminiscent of an avalanche. **c**) $\rho = 0.95$, $\lambda_a = 0.67$, $\beta = 0.5$, $\dot{\gamma} = 3 \cdot 10^{-6}$. For high self propulsion speed the density becomes inhomogeneous.

We hypothesized that we did not find a power law for the stress versus strain rate, because we were technically shearing different systems at different strain rates.

Therefore we tried modelling the self propulsion force as a constant rather than a force proportional to the strain rate. As always, we set the self propulsion force, F_{self}, with a dimensionless parameter $\lambda_s = F_{\text{self}}/k\bar{a}$. Note that for very small self propulsion forces, the particle's motion will be dominated by shear forces. In that regime, the orientation of the particles does not matter as it only sets the direction of self propulsion. Hence, when shear forces dominate self propulsion forces, our system becomes equivalent to the system in Tighe et al. [4]. Therefore, we have to choose the self propulsion force to be comparable to the shear force at the largest strain rate we impose ($\dot{\gamma} = 0.01$). We choose $0.01 < \lambda_s < 0.1$, because the effects of shear and self propulsion are comparable.

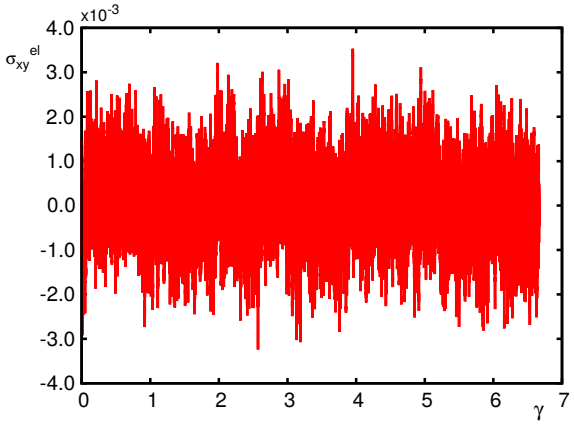

Figure 5.4: The xy-component of the total elastic stress in the system as a function of the applied strain. The noise on the elastic stress can be several orders of magnitudes larger than its average value for certain parameters. This simulation had a density of $\rho = 0.90$ and ran for a total of 2×10^7 steps reaching a total strain of $\gamma = 6.67$. Other parameters were $\lambda_s = 0.08$, $\lambda_a = 0.45$, $\lambda_n = 0.03$ and $\dot{\gamma} = 10^{-5}$.

At low strain rates, the motion of the particle is dominated by self propulsion. Unfortunately, the stress response becomes extremely noisy. In figure 5.4 we show the value of the xy-component of the stress tensor as a function of the strain γ. The standard deviation in the stress is an order of magnitude larger than the mean value. We conclude that the indirect effect of the large self propulsion force dominates the xy-component. As we argued before, a large self propulsion force, combined with particles that are not aligned perfectly, causes a lot of random overlap between particles. Therefore, the stress response of self propelling particles is inherently noisy.

4. Conclusion

In conclusion, we tried to quantify the solid-liquid transition in active materials by calculating the stress response upon shearing. The combination of a self propulsion force and an orientational noise makes the stress inherently noisy. The only way we found to reduce the noise was by decreasing the self propulsion force or by eliminating the orientational noise. However, those systems are equivalent to passive particle systems. We cannot determine the material properties like the shear modulus and the jamming transition with this method. Instead we choose to quantify jamming by a direct measure of the rearrangements in the system (see chapter 3).

Acknowledgements

A big thank you to Brian Tighe for showing me how to calculate the stress in systems with Lees-Edwards boundary conditions. I also want to thank Dion Koeze for fruitful discussions on calculating the contributions to the stress tensor.

References

[1] A. J. Liu and S. R. Nagel, *Nonlinear dynamics: Jamming is not just cool any more,* Nature **396**, 21 (1998).

[2] P. Olsson and S. Teitel, *Critical scaling of shear viscosity at the jamming transition,* Phys. Rev. Lett. **99**, 178001 (2007).

[3] C. S. O'Hern, S. A. Langer, A. J. Liu, and S. R. Nagel, *Random packings of frictionless particles,* Phys. Rev. Lett. **88**, 075507 (2002).

[4] B. P. Tighe, E. Woldhuis, J. J. C. Remmers, W. van Saarloos, and M. van Hecke, *Model for the scaling of stresses and fluctuations in flows near jamming,* Phys. Rev. Lett **105**, 088303 (2010).

[5] D. Vågberg, P. Olsson, and S. Teitel, *Critical scaling of bagnold rheology at the jamming transition of frictionless two-dimensional disks,* Phys. Rev. E **93**, 052902 (2016).

[6] K. W. Desmond, P. J. Young, D. Chen, and E. R. Weeks, *Experimental study of forces between quasi-two-dimensional emulsion droplets near jamming,* Soft Matter **9**, 3424 (2013).

[7] M. van Hecke, *Jamming of soft particles: geometry, mechanics, scaling and isostaticity,* J. Phys. Condens. Matter **22**, 033101 (2009).

A. Stress generation by torques

To quantify jamming, we determine the of diagonal components of the stress tensor. In two dimensions, the stress tensor can be represented by a 2×2 matrix. Its elements can in principle be independent. For a certain choice of basis, we can decompose the matrix to identify four contributions. These components are

$$\begin{pmatrix} 1 & 0 \\ 0 & 1 \end{pmatrix} : \text{representing the hydrostatic pressure on the object,}$$

$$\begin{pmatrix} 1 & 0 \\ 0 & -1 \end{pmatrix} : \text{representing a force dipole on the object}[2],$$

$$\begin{pmatrix} 0 & 1 \\ 1 & 0 \end{pmatrix} : \text{representing a force dipole on the object}[2],$$

$$\begin{pmatrix} 0 & 1 \\ -1 & 0 \end{pmatrix} : \text{representing torques on the object.}$$

In figure 5.5 we illustrate how such forces act on a square.

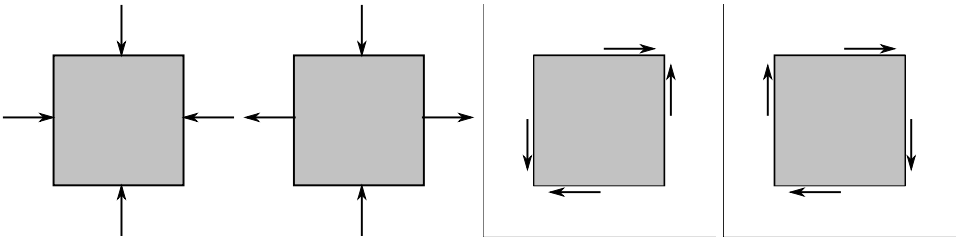

Figure 5.5: Illustration of the forces applied to the sides of an object. From left to right, the contributions to the stress tensor due to these forces are, the hydrostatic pressure, a force dipole, a pure shear, and a torque.

In the main text, we have only looked at what stresses are generated by shear forces and how we can measure them. From this decomposition we see that torques in the system can contribute to the off-diagonal components of the stress tensor as well. However, in this appendix we prove that the torques in our system do not have a direct contribution.

When there is no torque acting on the system, the stress tensor satisfies

$$\sigma_{\alpha\beta} = \sigma_{\beta\alpha}. \tag{5.15}$$

Therefore, in equilibrium statistical physics an isolated system always has a symmetrical stress tensor. After all, a system that has an asymmetric stress tensor would spontaneously rotate. Systems out of equilibrium will however, in general have an asymmetric stress tensor. The torque is the difference between the off-diagonal terms of the stress tensor.

$$T_{\alpha\beta} = \sigma_{\alpha\beta} - \sigma_{\beta\alpha} \tag{5.16}$$

[2]Both matrices are special cases of a representation of a pure shear, but act on a different axis. Hence, these two components are dependent on the choice of coordinate system.

The torque $T_{\alpha\beta}$ denotes the torque in the $\alpha\beta$ plane. It is conventional to label the torque by the direction of its axis rather than the plane the object rotates in. So according to convention, we should write

$$T_\gamma = \frac{1}{2}\epsilon_{\alpha\beta\gamma}T_{\alpha\beta} = \frac{1}{2}\epsilon_{\alpha\beta\gamma}(\sigma_{\alpha\beta} - \sigma_{\beta\alpha}), \tag{5.17}$$

where $\epsilon_{\alpha\beta\gamma}$ is known as the Levi-Civita tensor. The contribution to the stress tensor by torques are antisymmetric. Therefore we can write

$$T_\gamma = \epsilon_{\alpha\beta\gamma}\sigma^T_{\alpha\beta}. \tag{5.18}$$

The superscript T for this contribution to the stress to indicates that this contribution is the result of a torque, hence antisymmetric. When we solve this for σ_{xy}, we obtain

$$\sigma^T_{xy} = \frac{1}{2}T_z. \tag{5.19}$$

We have three torques present in our system: (i) particles align with their surroundings, (ii) orientational noise that destroys the alignment and (iii) a drag torque, which makes rotational movement over-damped as well. The alignment can be thought of as an interaction between particles, where neighbours exert torques on each other (even though they turn themselves). The other two torques are purely individual. All of these torques point in the z direction, so the stress due to the torque is given by

$$\sigma^T_{xy} = \frac{1}{2}\sum_i \sum_{j\in\mathcal{N}_i} T_{ij,\text{align}} + T_{i,\text{noise}} - T_{i,\text{drag}} \tag{5.20}$$

Notice that the argument of the sum over all particles i is identical to our equation of motion $\sum_{j\in\mathcal{N}_i} T_{ij,\text{align}} + T_{i,\text{noise}} - T_{i,\text{drag}} = 0$. We conclude that torques do not contribute to the total stress tensor. Their components do contribute, but they are simply cancelled by the rotational drag. For the sake of completeness, the contributions of the alignment and the noise to the stress tensor are given by

$$\sigma^{\text{align}}_{xy} = \frac{1}{2}\sum_i \frac{1}{|\mathcal{N}_i|}\sum_{j\in\mathcal{N}_i} \frac{\xi\lambda_{\text{align}}}{\tau}\theta_{ij}$$

and

$$\sigma^{\text{noise}}_{xy} = \frac{1}{2}\sum_i w_i\xi\sqrt{\frac{2\lambda_{\text{noise}}}{\Delta t\tau}}.$$

where w_i is randomly chosen from $\{1, -1\}$. This stress will therefore also be very small.

Finally, we should also look carefully at what shearing does to the individual particles. Shearing not only causes the particles to move, but also exerts a torque on the particles. More precisely, the flow of the viscous fluid satisfies a Couette flow

($v_{\text{aff}}(y) = \frac{y}{L}L\dot{\gamma} = y\dot{\gamma}$ for $-\frac{1}{2}L \leq y < \frac{1}{2}L$). Therefore, finite sized particles will feel different flows at opposite sides of the particle. In the lab frame, the particle moves at a speed equivalent to the flow speed at its centre of mass position, y_{CM}. In the frame moving with the centre of mass of the particle, one side of the particle will feel a drag force

$$\begin{aligned} F_{\text{drag}} &= \zeta(v_i - v_{\text{aff}}(y_{CM} + R)) \\ &\approx \zeta(v_{\text{aff}}(y_{CM}) - v_{\text{aff}}(y_{CM} + R)) \\ &= \zeta\dot{\gamma}(y_{CM} - y_{CM} - R) \\ &= -\zeta\dot{\gamma}R \end{aligned}$$

and at the other side

$$\begin{aligned} F_{\text{drag}} &= \zeta(v_i - v_{\text{aff}}(y_{CM} - R)) \\ &= \zeta\dot{\gamma}R \end{aligned}$$

These forces point in opposite directions at opposite sides of the particle. Hence the particle will feel a torque $\tau = 2(R \times F) = 2\zeta\dot{\gamma}R^2$. We can find the period of one revolution due to this torque by equating it to our rotational equation of motion $\tau = \xi\dot{\theta}$. The torque is constant in time, so solving this differential equation is rather trivial. The period is given by

$$\tau_{\text{drag}} = 2\pi\frac{\xi}{2\zeta\dot{\gamma}R^2} = \frac{\pi\xi}{\zeta\dot{\gamma}} \tag{5.21}$$

In our simulations, we set $\xi = \zeta = 1$, and we have used strain rates in the range $3 \times 10^{-6} \leq \dot{\gamma} \leq 10^{-2}$. The smallest time scale of this torque ($\tau_{\text{drag}} \sim 10^2$) is 4 orders of magnitude longer that the time scale of the noise. We can conclude that this torque does not play any relevant role in our dynamics.

6

Mechanics of epithelial tissue formation

A key process in the life of any multicellular organism is its development from a single egg into a full grown adult. The first step in this process often consists of forming a tissue layer out of randomly placed cells on the surface of the egg. We present a model for generating such a tissue, and find that the resulting cellular pattern corresponds to the Voronoi tessellation of the nuclei of the cells. Experimentally, we obtain the same result in both fruit flies and flour beetles, with a distribution of cell shapes that is matched by that of the model, without any adjustable parameters. Finally, we show that this pattern is broken when the cells do not all have the same growth rate.

This chapter by Ruben van Drongelen, Tania Vazquez Faci, Teun A. P. M. Huijben, Maurijn van der Zee, and Timon Idema is submitted as "Mechanics of epithelial tissue formation", and is available on https://arxiv.org/abs/1705.06205

1. Introduction

Multicellular organisms start life as a single fertilised cell. From this modest beginning, they undergo a developmental process that leads to the formation of complex tissues and organs with a wide range of different functions. Although it has long been appreciated that these various components of an organism have very different mechanical properties, the role of mechanical interactions in the developmental process has only become the focus of detailed studies relatively recently. One of the earliest milestones in this field is the seminal work by Discher et al. [1] and Engler et al. [2], who showed that identical stem cells, when placed on substrates of different stiffness, differentiate into cells of tissues with the corresponding stiffness. Cells in living multicellular organisms, however, do not exist on a substrate in isolation; instead, they are part of a tissue that consists of both cells and extracellular material and together form a mechanical system [3]. Moreover, cells react strongly to both direct mechanical interactions with their neighbours [4–7] and indirect interactions via deformations of a shared substrate [8–10]. Finally, the interior organisation of the cell, in particular the position of the nucleus, is also mechanically coupled to its outside environment [11]. To understand how epithelial tissues develop, we thus need a mechanical model coupling the inside to the outside of the cell.

As a model epithelial tissue, we study the first tissue developed in insect embryos, the epithelial blastoderm. This tissue forms as a single layer on top of the yolk. The nuclei of the fertilised egg first divide a couple of times in the egg's interior, then migrate to the surface where they continue to divide, eventually creating a confluent proto-tissue (see figure 6.1a). This proto-tissue is turned into a proper tissue through invagination of the egg's outer (plasma) membrane, which separates the nuclei into cells (cellularisation) [12–18]. Already during the syncytial stage (i.e., before cellularisation), each nucleus is embedded in a full cellular apparatus, including organelles and a cytoskeleton. We present a model for the formation of the epithelial blastoderm. We also study this tissue formation directly in two model organisms: the fruit fly *Drosophila melanogaster* and the flour beetle *Tribolium castaneum*. We find that the touching boundaries of the (proto)cells correspond closely to a Voronoi tessellation of their nuclei, an effect that becomes more pronounced after cellularisation (see figure 6.1b for an explanation of a Voronoi tessellation). Although Voronoi tessellations have occasionally been used to describe cellular patterns in epithelial tissues [19–24], to the best of our knowledge, the fact that the nuclei are located at the centers of the corresponding Voronoi cells has not been shown previously. Tessellations have also been used as a basis for mechanical modeling of cellular tissues, especially in vertex models where forces act on the vertices of a lattice [21, 25–31]. In contrast, our model faithfully reproduces the Voronoi tessellation, and matches the experimental data quantitatively on a number of geometric and topological measures, without any adjustable parameters. We conclude that the mechanical interactions between the (proto)cells in early embryonic epithelial tissues are directly responsible for the observed geometrical cellular patterns of those tissues.

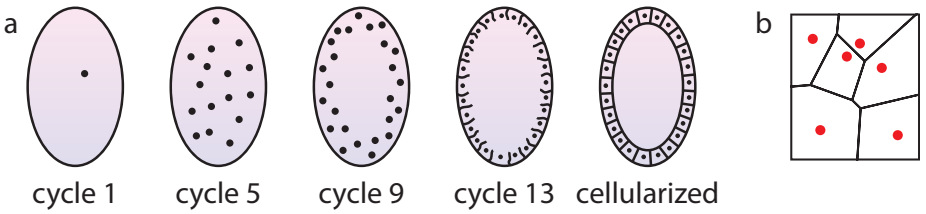

Figure 6.1: a) Several stages in the development of insect embryos. After a couple of nuclear division cycles, the nuclei migrate to the periphery. After a couple more divisions, cells are formed by enclosing a membrane around each nucleus. b) Example of a Voronoi tessellation. Each seed in red generates a cell where all points in that cell are closest to its seed.

2. Model

We model the cells in two dimensions, treating them as purely mechanical objects. Our cells consist of a nucleus, a radial and stiff microtubule network, and a more flexible actin cortex at the cell perimeter [32]. We model the nucleus as a single large bead with radius R_n, and the cortex as a collection of M small beads with radius R_c that surround the nucleus (figure 6.2a). The cortical beads initially form a circle around the nuclei. We connect each bead to its two neighbours by a spring with spring constant k_c and rest length $u_c = 2R_c$ to mimic the forces in the actin cortex. Cortical beads that are not connected through these springs interact via the repulsive part of the same potential. Microtubules are modelled as springs that connect the nuclear bead to individual beads in the membrane. To do so, we select at random a fraction $f = 1/6$ of the cortex beads and connect them to the nuclear bead with a spring of spring constant k_{MT} and rest length $u_{MT} = 2R_n$.

We initiate our system by placing N non-overlapping, circular cells at random positions in the plane. To let the cells grow, we allow the rest length of the microtubules and actin filaments to increase linearly over time. Because cells cannot interpenetrate, they exert forces on each other when they touch. These forces counteract the growth of the microtubules, which halts at a given stall force. A microtubule stops extending when the membrane bead it is connected to comes within 99% of the minimal equilibrium distance to a bead of another protocell. In this event we also lock the relative position of the beads. When half of the microtubules have stopped growing, the growth of the actin filaments also stops.

To let the cells divide, we first double the number of beads in the membrane and the number of microtubules connecting them to the nucleus. We then split the nucleus into two daughter nuclei of half the size. Of the cortical beads connected to a microtubule, we select the two beads forming the shortest axis across the cell. We then use this axis to divide the microtubules over the two nuclei (figure 6.2b). To help the nuclei separate, an extra spring is positioned between the nuclei, mimicking the interpolar microtubules. The rest length of the interpolar spring is gradually increased from zero to the radius of the nucleus, while the rest length of the other microtubules is reduced with a factor $\sqrt{2}$, so that the total area of the cell remains the same. Once this process is completed, the two axis beads are contracted using

a new spring, and when brought together, duplicated and re-connected to complete the division of the cells.

The dynamics of the cytoskeleton and the nuclei are over-damped because the inertia of these small cell components is negligible compared to their viscous drag. Therefore, our equation of motion follows from equating the net force to the drag force, as given by Stokes' law:

$$\mathbf{F}_{i,\mathrm{net}} = 6\pi\eta R_i \mathbf{v}_i, \tag{6.1}$$

where $\mathbf{F}_{i,\mathrm{net}}$ is the total (net) force on object i, which can be either a nuclear or a cortical bead. The viscosity is denoted by η, R_i is the radius of object i, and $\mathbf{v}_i$ is its velocity.

In our simulations, we scale our measure of length by setting $R_\mathrm{c} = 1$. For the repulsion between two cortical beads we can define a characteristic time $\tau \equiv 6\pi\eta/k_\mathrm{c}$. We non-dimensionalise the units of time and force by setting $\tau = k_\mathrm{c} = 1$.

We introduce a quality number Q to quantify the match between the Voronoi tessellation of the nuclei and the actual cells. To do so, we compare the actual area, A_r, of the cells to the area of their corresponding Voronoi cells, A_V. We define Q as:

$$Q = \frac{1}{N}\sum_{i=1}^{N}\left(\frac{A_{\mathrm{r},i} - A_{\mathrm{V},i}}{A_{\mathrm{r},i}}\right)^2, \tag{6.2}$$

where N is the total number of cells. When the Voronoi tessellation has a perfect match with the actual cells the value of Q is 0. For comparison, the Q number for a random close packing of identical discs is 0.05.

3. Experimental system

This work was done in collaboration with Tania Vazquez-Faci. I want to thank her for doing the experiments and analysis of the experimental data.

To be able to concurrently observe the nuclei and the actin cortex of *D. melanogaster* and *T. castaneum*, we required lines in which both parts are fluorescently labelled. For *D. melanogaster*, she used His2A-RFP/sGMCA flies (Bloomington Drosophila Stock Centre number 59023) that ubiquitously express Histone2A fused to Red Fluorescent Protein (RFP) and the Actin-binding domain of Moesin fused to Green Fluorescent Protein (GFP) [33]. For *T. castaneum*, she created a line that ubiquitously expresses LifeAct [34] fused to EGFP [35], thus labeling actin. She further crossed this line to an available nuclear-GFP line [36]. We called the crossed line LAN-GFP.

4. Results

First, we observe what happens when we let our model cells grow without division, using random initial placement and double periodic boundary conditions. Because the cortical beads experience drag, the ones that are not connected to a growing microtubule lag behind those that are. When growing cells touch and connect, the forces from the growing microtubules also feed back on the nuclear bead, which

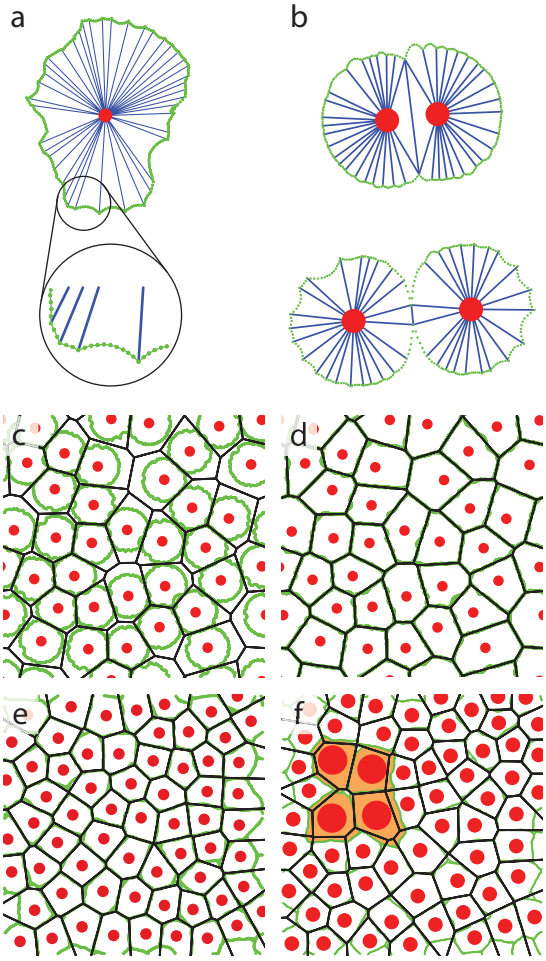

Figure 6.2: Mechanical cell model and simulation results. (a) Cells consist of a sphere representing the nucleus (red), connected via microtubules modelled as stiff springs (blue) to the actin cortex, which is modelled as a number of beads connected by weaker springs (green). (b) Cell division. (c) Growing cells at 70% coverage. Where cell boundaries touch, they coincide with the Voronoi boundaries of their nuclei. (d) Growing cells at 100% coverage (no division). (e) Growing and dividing cells at 98% coverage after two divisions. (f) Growing and dividing cells at 98% coverage after two divisions, for the case in which one initial cell (with four daughters, indicated in orange) has a growth rate that is 2.5× larger than that of the others.

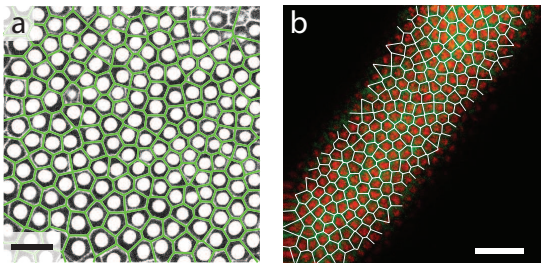

Figure 6.3: Epithelial blastoderm after cellularisation of (a) *Tribolium* and (b) *Drosophila* embryos. Overlaid in both images is the Voronoi tessellation of the centroids of the nuclei. Scale bars are 25 μm.

shifts position. figure 6.2c shows a snapshot of a simulation in which the cells have reached about 70% coverage of the plane. Where neighbouring cells touch, their boundaries coincide with the Voronoi tessellation of the nuclei. The Q number for this case is fairly high ($Q = 0.22$), representing the fact that there are still big gaps between the cells. When we let the cells grow further, they eventually reach 100% coverage, and their geometrical pattern matches the Voronoi tessellation of their nuclei almost perfectly ($Q = 2.1 \cdot 10^{-3}$, figure 6.2d). If we let the cells divide during the developmental process, the final picture is much the same, with again an almost perfect match to the Voronoi tessellation ($Q = 3 \cdot 10^{-3}$, figure 6.2e). However, if we give one of the initial cells a larger growth rate (inherited by its daughters), we find that this pattern is broken (figure 6.2f). The faster-growing cells cover a larger fraction of the available area than their corresponding Voronoi cells, whereas their slower-growing neighbours are left with a compressed shape.

In both insect systems we studied, the picture is very similar to the simulation results. (Proto)cells appear on the surface at random positions, and grow to confluency after two (*Tribolium*) or three (*Drosophila*) divisions. When the cells cover 100% of the available area, their boundaries also closely match the Voronoi tessellation of their nuclei, as shown in figure 6.3.

To quantify the match between the experimental and the numerical results, we determine the value of two geometrical and one topological property of the cells after cellularisation. First, we measure the variance of the area per Voronoi cell, which we find to be very low in both embryos and in the simulations (Table 6.1), indicating that all cells grow to roughly the same size. Second, we measure the reduced area (or circularity) A^* per Voronoi cell, defined as $A^* = 4\pi A/P^2$, where A is the area and P the perimeter of the cell [37]. With this definition, circles have a reduced area of 1, and hexagons have reduced area of $\pi/2\sqrt{3} \approx 0.91$. We find that the average reduced area of the Voronoi cells in both our experimental systems and in our simulations is again a close match with a value of about 0.83 (Table 6.1).

In addition to the two geometrical measures given above, we also consider a topological measure: the relative occurrence of cells with a given number of vertices. For a perfectly regular pattern (a honeycomb lattice), all cells are hexagons, and thus all cells have six vertices. Deviations from this pattern occur in the form of cells with five and seven vertices (with the total number of vertices of all cells being conserved), or even four or eight vertices. Not surprisingly, hexagonal cells are most abundant in our Voronoi tessellations. However, we also find large numbers of

	Experiments	
	T. castaneum	*D. melanogaster*
Variance of the area	0.02 ± 0.02	0.05 ± 0.005
Reduced area A^*	0.85 ± 0.02	0.83 ± 0.02
Q number	0.0009	0.02

	Simulations		
	no division	with division	unequal growth
Variance of the area	0.02 ± 0.005	0.01 ± 0.002	0.037 ± 0.004
Reduced area A^*	0.83 ± 0.01	0.83 ± 0.01	0.83 ± 0.01
Q number	0.002	0.003	0.017

Table 6.1: Values of the two geometrical measures and quality number of the Voronoi tessellations of our experimental and simulated systems. The variance of the area is very small in the first four cases, indicating that in each case, all resulting cells have roughly the same size. In the case where a single cell grows 2.5 times faster than the others (last column), we immediately get a significant increase in this variance. The reduced area (area divided by the perimeter squared normalised such that a circle has a value of 1) is very similar in all cases. Notably, the reduced area is significantly less than that of a regular hexagon (0.91), consistent with the topological observation that only about half of the cells in our system have six vertices.

pentagons and heptagons, which each account for about 25% of the cells (figure 6.4). Again, the two experimental systems and the simulation all agree quantitatively.

5. Discussion

Our simulations consistently predict that the growing or growing-and-dividing cells will create a spatial pattern that closely matches the Voronoi tessellation of their nuclei. We observe the same pattern in the first epithelial tissue in our two experimental systems. Moreover, the distribution of cell shapes that we find in the experiments is reproduced exactly by the simulations, without any adjustable parameters. Earlier models, which start from a Voronoi tessellation, require a large number of adjustment steps to reach this distribution [21, 24–26, 29, 31]. Our model instead provides a mechanism for constructing the Voronoi tessellation directly.

In both experimental systems and in the simulations, we measure a reduced area A^* of the cells of about 0.83, just below the order-disorder phase transition reported by Hočevar and Ziherl at $A^* = 0.865$ [37]. For higher values, epithelial tissues consist almost exclusively of hexagons and are ordered. For values of A^* below the critical value, the tissues are disordered and contain considerable fractions of polygons which are not hexagons, as we observe in our systems. Recent work by Bi et al. [38, 39] showed that at almost the same value of the reduced area ($A^* = 0.866$), tissues exhibit a rigidity transition. These authors modelled an active tissue using self-propelled Voronoi cells and found that below the reported critical value, the tissues behave fluid-like, whereas for higher values they are solid-like. The tissues in our insect embryos have a reduced area A^* between 0.83 and 0.85, which classifies them as (just) liquid-like. This observation is consistent with the stage of development we observe. After cellularisation, the embryos undergo a massive shape change, known

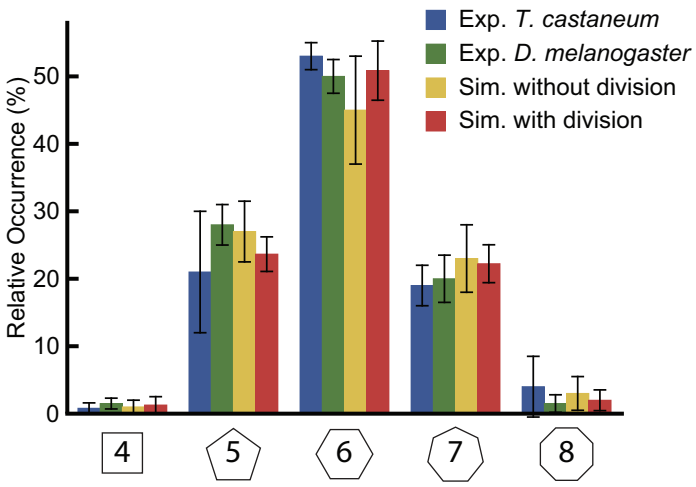

Figure 6.4: Relative occurrence of cells with a given number of vertices in the Voronoi tessellation after cellularisation for our experimental observations on *T. castaneum* (blue) and *D. melanogaster* (green) and our simulations without (yellow) and with (red) division. Note that where a perfect honeycomb lattice would consist exclusively of hexagons, only about half of our cells have six vertices, in both experiments and in the simulations.

as gastrulation, in which the mesoderm is formed. Another round of divisions before cellularisation would probably push the system over the critical point into a jammed state, which would make gastrulation much more difficult. On the other hand, the cells must be confluent to form a fairly stable tissue. Our observation that the system exists just on the liquid side of the jamming transition may therefore well correspond to a necessary step in development. This 'development up to jamming' might also underlie the different number of nuclear divisions before cellularisation in different insects [12, 18].

As our simulations show, despite the fact that the cells are placed on the surface randomly, they all reach the same final size (as illustrated by the low variance in the area). We again observe the same effect in the experiments. However, if some cells grow faster than others, our model shows that the regular pattern is broken. The faster-growing cells end up being larger than the others, and they moreover break the Voronoi tessellation, as their actual boundaries lie well outside their Voronoi cell. These results indicate that the Voronoi patterns observed in many epithelial tissues are due to the mechanical interactions between the proliferating cells that build the tissue, and that those cells must all grow at the same rate.

6. Conclusion

We modelled the development of a confluent epithelial tissue from identical cells that are initially distributed randomly. We observe that the resulting configuration of the cells in the tissue closely matches the Voronoi tessellation of their nuclei. We experimentally find the same behaviour for the newly formed cells of the epithelial

blastoderm in both *D. melanogaster* and *T. castaneum*. We find in both simulations and experiment that in the specific tessellation the cells form, they all have roughly the same area, and the distribution of cell shapes is identical for experiment and simulations. Moreover, the arrangement of the cells is such that the resulting tissue is just on the liquid side of the jamming transition. We can understand the formation of this pattern from mechanical interactions between the cells. Growing cells eventually come into contact with their neighbours, resulting in mechanical feedback that causes them to stop growing towards that neighbour. These contacts moreover translate back to a mechanical force on the nuclei of the cells, which causes them to re-position and eventually form the observed Voronoi tessellation. Thus, mechanical interactions largely determine cell arrangement and shape in epithelial tissues.

Acknowledgements

I want to thank Tania for doing the experimental part of this study, as well as for the many constructive discussions we had on writing parts of this chapter. Finally, I would like to thank Teun. He did a brilliant job of extending the model to include divisions and show that this model is amazingly robust to fluctuations.

References

[1] D. E. Discher, P. Janmey, and Y.-L. Wang, *Tissue cells feel and respond to the stiffness of their substrate,* Science **310**, 1139 (2005), http://science.sciencemag.org/content/310/5751/1139.full .

[2] A. J. Engler, S. Sen, H. L. Sweeney, and D. E. Discher, *Matrix elasticity directs stem cell lineage specification,* Cell **126**, 677 (2006).

[3] K. E. Kasza, A. C. Rowat, J. Liu, T. E. Angelini, C. P. Brangwynne, G. H. Koenderink, and D. A. Weitz, *The cell as a material,* Curr. Opin. Cell Biol. **19**, 101 (2007), cell structure and dynamics.

[4] V. Vogel and M. Sheetz, *Local force and geometry sensing regulate cell functions,* Nat. Rev. Mol. Cell Biol. **7**, 265 (2006).

[5] U. S. Schwarz and S. A. Safran, *Physics of adherent cells,* Rev. Mod. Phys. **85**, 1327 (2013).

[6] T. Idema, J. O. Dubuis, L. Kang, M. L. Manning, P. C. Nelson, T. C. Lubensky, and A. J. Liu, *The syncytial drosophila embryo as a mechanically excitable medium,* PLoS One **8**, e77216 (2013).

[7] J. H. Shawky and L. A. Davidson, *Tissue mechanics and adhesion during embryo development,* Dev. Biol. **401**, 152 (2015).

[8] X. Tang, P. Bajaj, R. Bashir, and T. A. Saif, *How far cardiac cells can see each other mechanically,* Soft Matter **7**, 6151 (2011).

[9] S. Majkut, T. Idema, J. Swift, C. Krieger, A. Liu, and D. E. Discher, *Heart-specific stiffening in early embryos parallels matrix and myosin expression to optimize beating,* Curr. Biol. **23**, 2434 (2013).

[10] I. Nitsan, S. Drori, Y. E. Lewis, S. Cohen, and S. Tzlil, *Mechanical communication in cardiac cell synchronized beating,* Nat. Phys. **12**, 472 (2016).

[11] A. Zemel, *Active mechanical coupling between the nucleus, cytoskeleton and the extracellular matrix, and the implications for perinuclear actomyosin organization,* Soft matter **11**, 2353 (2015).

[12] D. T. Anderson, *The development of holometabolous insects,* in *Dev. Syst. Insects*, edited by S. J. Counce and C. H. Waddington (Academic Press, London, 1972) pp. 1531–1545.

[13] V. E. Foe and B. M. Alberts, *Studies of nuclear and cytoplasmic behaviour during the five mitotic cycles that precede gastrulation in Drosophila embryogenesis.* J. Cell Sci. **61**, 31 (1983).

[14] K. Handel, C. G. Grünfelder, S. Roth, and K. Sander, *Tribolium embryogenesis: a SEM study of cell shapes and movements from blastoderm to serosal closure.* Dev. Genes Evol. **210**, 167 (2000).

[15] A. Mazumdar and M. Mazumdar, *How one becomes many: blastoderm cellularization in drosophila melanogaster,* Bioessays **24**, 1012 (2002).

[16] T. Lecuit, *Junctions and vesicular trafficking during Drosophila cellularization,* J. Cell Sci. **117**, 3427 (2004).

[17] T. J. C. Harris, J. K. Sawyer, and M. Peifer, *How the cytoskeleton helps build the embryonic body plan: models of morphogenesis from drosophila,* Curr. Top. Dev. Biol. **89**, 55 (2009).

[18] M. van der Zee, M. A. Benton, T. Vazquez-Faci, G. E. M. Lamers, C. G. C. Jacobs, and C. Rabouille, *Innexin7a forms junctions that stabilize the basal membrane during cellularization of the blastoderm in tribolium castaneum,* Development **142**, 2173 (2015).

[19] H. Honda, *Description of cellular patterns by dirichlet domains: The two-dimensional case,* Journal of Theoretical Biology **72**, 523 (1978).

[20] D. Sulsky, S. Childress, and J. K. Percus, *A model of cell sorting,* J. Theor. Biol. **106**, 275 (1984).

[21] M. Weliky and G. Oster, *The mechanical basis of cell rearrangement. i. epithelial morphogenesis during fundulus epiboly,* Development **109**, 373 (1990).

[22] V. Sharma, M. Crne, J. O. Park, and M. Srinivasarao, *Structural origin of circularly polarized iridescence in jeweled beetles,* Science **325**, 449 (2009).

[23] M. Bock, A. K. Tyagi, J.-U. Kreft, and W. Alt, *Generalized voronoi tessellation as a model of two-dimensional cell tissue dynamics,* Bull. Math. Biol. **72**, 1696 (2010).

[24] D. Sanchez-Gutierrez, M. Tozluoglu, J. D. Barry, A. Pascual, Y. Mao, and L. M. Escudero, *Fundamental physical cellular constraints drive self-organization of tissues,* EMBO J. **35**, 77 (2016).

[25] R. Farhadifar, J.-C. Röper, B. Aigouy, S. Eaton, and F. Jülicher, *The influence of cell mechanics, cell-cell interactions, and proliferation on epithelial packing,* Curr. Biol. **17**, 2095 (2007).

[26] D. B. Staple, R. Farhadifar, J. C. Röper, B. Aigouy, S. Eaton, and F. Jülicher, *Mechanics and remodelling of cell packings in epithelia,* Eur. Phys. J. E **33**, 117 (2010).

[27] A. G. Fletcher, M. Osterfield, R. E. Baker, and S. Y. Shvartsman, *Vertex models of epithelial morphogenesis,* Biophys. J. **106**, 2291 (2014).

[28] S. Okuda, Y. Inoue, and T. Adachi, *Three-dimensional vertex model for simulating multicellular morphogenesis,* Biophys. Physicobiol. **12**, 13 (2015).

[29] D. L. Barton, S. Henkes, C. J. Weijer, and R. Sknepnek, *Active vertex model for cell-resolution description of epithelial tissue mechanics,* PLOS Computational Biology **13**, 1 (2017).

[30] S. Alt, P. Ganguly, and G. Salbreux, *Vertex models: from cell mechanics to tissue morphogenesis,* Philos. Trans. R. Soc. B Biol. Sci. **372**, 20150520 (2017).

[31] S.-Z. Lin, B. Li, and X.-Q. Feng, *A dynamic cellular vertex model of growing epithelial tissues,* Acta Mech. Sin. **33**, 250 (2017).

[32] F. Gittes, B. Mickey, J. Nettleton, and J. Howard, *Flexural rigidity of microtubules and actin filaments measured from thermal fluctuations in shape,* J. Cell Biol. **120**, 923 (1993).

[33] D. P. Kiehart, C. G. Galbraith, K. A. Edwards, W. L. Rickoll, and R. A. Montague, *Multiple forces contribute to cell sheet morphogenesis for dorsal closure in Drosophila,* J. Cell Biol. **149**, 471 (2000).

[34] J. Riedl, A. H. Crevenna, K. Kessenbrock, J. H. Yu, D. Neukirchen, M. Bista, F. Bradke, D. Jenne, T. A. Holak, Z. Werb, M. Sixt, and R. Wedlich-Soldner, *Lifeact: a versatile marker to visualize F-actin.* Nat. Methods **5**, 605 (2008), arXiv:arXiv:1011.1669v3 .

[35] M. A. Benton, M. Akam, and A. Pavlopoulos, *Cell and tissue dynamics during Tribolium embryogenesis revealed by versatile fluorescence labeling approaches.* Development **140**, 3210 (2013).

[36] A. F. Sarrazin, A. D. Peel, and M. Averof, *A segmentation clock with two-segment periodicity in insects,* Science **336**, 338 (2012).

[37] A. Hočevar and P. Ziherl, *Degenerate polygonal tilings in simple animal tissues,* Phys. Rev. E **80**, 011904 (2009).

[38] D. Bi, J. H. Lopez, J. M. Schwarz, and M. L. Manning, *A density-independent rigidity transition in biological tissues,* Nat. Phys. **11**, 1074 (2015).

[39] D. Bi, X. Yang, M. C. Marchetti, and M. L. Manning, *Motility-driven glass and jamming transitions in biological tissues,* Phys. Rev. X **6**, 021011 (2016).

Acknowledgements

In these last pages I want to express my gratitude to all the people who helped me get to the point where I can defend my thesis. Finishing a PhD can be quite a rough journey. I have heard stories from students in other departments, and I have seen the horrifying numbers in the news about PhD students that suffer from depressions. It is because of all the people in the following section that I did not experience my four years in the BionanoScience department like that.

Timon, I remember very well the first time I stepped into your office in the old TNW building. I made a slight miscalculation and only realized that morning I did not have anything appropriate to wear to the interview. Fortunately you saw right through that and I was welcome to start as your first student. In the beginning the group was just the two of us, but eventually the group grew to a size where we didn't even fit in the room where we held our group meetings. But even as the group grew, you always had time to help me with my struggles. I recall a couple of occasions where I was completely stuck, or demotivated by not getting the results I was looking for. But somehow you always managed to inspire me, and after our discussions I would return to my office full of confidence and fully motivated. Thank you for always being there for me.

I want to thank the whole theory group. Aafke and Afshin, we have shared an office together for over three years. This whole dissertation would not have been possible without all the discussions we had over these years. Aafke, I hope you're having a great time in the States, and I wish you all the best with your postdoc. And Afshin, thank you for joining me on kebab-Thursday and best of luck in Pouyan's group and finshing up the thesis. Thank you Tania for collaborating with me on my final project. And Misha, I liked how you randomly turned up in the office. I am still not sure if you were the neighbour or part of our office ;). Martin, thanks for all your scientific and non-scientific feedback, joining me for kebab, and sharing games. I want to thank all the students who have worked in our group. In particular Yuan, Peterke, Teun and Daniel; I was happy to (partially) supervise your projects. Special thanks go to Brian Tighe's group and especially Dion Koeze who have helped me a lot in understanding the physics of deforming near the jamming point.

Not long after I started I learned about the BN/QN football team, Real RKC. Playing football with all of you in the maandagavond competitie is the best start of the week one can have. Thanks to Felix and Bas for being captains prior to me. You both were excellent defenders. Thank you Fokko for taking over the captain role when I left. Daniel, you were almost always late to the match so you had to start out as the goalkeeper, but even when you were in time you voluntarily started on that position. As a goalie you were the best, and as a field-player you were everywhere, chasing every ball until you dropped from exhaustion. Fast and technical midfielder: Victor, our best striker: Mo, the smart and offensively minded

flank player: Pauline, solid flank defender: Orkide, and top-notch defender who never loses his calm: Maarten. Also, Sebastian, Calin, David, Maarten, Afshin, Magnus, Mohammed, Vincent, Bas, Kasper, Andrew, Soufian, and Luca, it was a pleasure playing football with you.

It has been a privilege to have worked in the BN-department. Thanks everyone! For all the science, and for all the fun and memorable moments. The Veldhoven conferences, the Christmas pot luck parties, the excursions to the beach, the skiing trip at Courchevel, the many games of fussball and much more.

Papa en mama, bedankt dat jullie altijd voor me zorgen en dat jullie mij altijd gesteund hebben. Ook voor wijze les om altijd te blijven leren en nieuwsgierig te zijn. Erwin, ten eerste wil ik je bedanken voor je bijdrage aan het visualiseren van de simulaties. Maar juist ook bedankt voor alles wat niet met het onderzoek te maken heeft. Samen met Jonathan, Michiel en Sander; bedankt voor alle ontspanning in de weekenden en de vakanties die mij ontstresst hebben. Anna, voor al je steun, in het bijzonder op de dagen waarop ik vreselijke cursussen moest volgen. Vaya, bedankt voor het warme ontvangst in Curacao toen ik probeerde mijn proefschrift probeerde te schrijven. En als laatste: bedankt Mystic Delft voor alle avonturen die ik met jullie heb meegemaakt onderwijl het schrijven van dit proefschrift. Articuno ik kies jou!

Samenvatting

De natuur is een wondere wereld. Altijd als ik bedenk dat al het leven op aarde ontstaan is door evolutie, sta ik versteld van de complexiteit en flexibiliteit van de organismen nu. Het lijkt alsof de natuur overal een oplossing voor verzint. Een bekend voorbeeld is de evolutie van de peper-en-zoutvlinder. Deze vlinder had oorspronkelijk voornamelijk de lichte kleur, maar dankzij de industriële revolutie vinden we nu vooral de variant van de vlinder met een donkere kleur. Het lijkt alsof de natuur zich hier actief aanpast, maar op de achtergrond is dit een voorbeeld van hoe evolutie de donkere vlinders betere overlevingskansen geeft. De evolutie van de vlinder is op deze manier nog te bevatten, maar er zijn ook talloze voorbeelden van enorme complexe systemen waarbij het niet voor te stellen is hoe via evolutie deze oplossing tot stand gekomen kan zijn. Deze systemen vereisen vele componenten die allemaal van elkaar afhankelijk zijn. Het weghalen van een enkele willekeurige component binnen zo'n netwerk zorgt ervoor dat het hele systeem niet meer werkt. Toch stuurt de natuur niet zelf op deze oplossing aan, en zijn natuurkundige principes verantwoordelijk voor het ontstaan van al het leven. Hoe dit gebeurd is, is een van de grote vragen binnen de discipline waar biologie en natuurkunde samen komen. Om te kunnen begrijpen hoe complexe systemen ontstaan zijn, is het eerst

belangrijk om te begrijpen hoe de systemen werken. In dit proefschrift behandel ik biologische systemen die bestaan uit vele eenheden. De eenheden binnen zo'n systeem hebben vaak dezelfde rol; er is geen leider die aangeeft wat een ander moet doen. Het bekendste voorbeeld hiervan zijn zwermen vogels die golvende patronen in de lucht laten zien. Iedere vogel doet zijn eigen ding, maar het resultaat is wat we noemen: collectief gedrag. Het gedrag van de groep is niet direct af te leiden uit het gedrag van het individu, maar het gevolg van de beweging van, en wisselwerkingen tussen individuen binnen de groep. Collectief gedrag vinden we ook terug op hele kleine schaal in kolonies van bacteriën of amoebes en zelfs in weefsels zien we collectief gedrag van cellen. Omdat het collectief gedrag in deze systemen veel op elkaar lijkt, zelfs als de individuen duizenden keren kleiner zijn, verwachten we dat in die systemen dezelfde principes gelden. De centrale vraag in dit proefschrift is daarom: *Welke principes liggen ten grondslag aan het collectief gedrag in biologische systemen?*

Om collectief gedrag te bestuderen, hebben we een model opgesteld. Dit model bestaat een set regels waar ieder individu aan voldoet. Een voorbeeld van zo'n regel is dat twee individuen niet op dezelfde plek kunnen zijn, en als ze te dicht bij elkaar komen, dat ze elkaar dan afstoten. Met een computer rekenen we deze regels door en vervolgens passen we de gevolgen van die regels voor ieder individu toe. Door de computer deze regels continu in zeer kleine tijd stapjes te laten uitrekenen, kunnen

we de beweging van ieder individu, en van de groep volgen. Wij zijn niet de eersten die zo'n model hebben opgesteld om collectief gedrag te onderzoeken, maar wat ons model wel uniek maakt, is dat de regels alleen van toepassing zijn op individuen die dicht bij elkaar staan. Bovendien hebben we geen externe factoren die ons systeem bij elkaar houden. In plaats daarvan beschrijven we in hoofdstuk 2 een regel die er voor zorgt dat de individuen aan de rand altijd naar binnen sturen. De simulaties tonen aan dat zelfs wanneer individuen alleen met hun directe buren communiceren, collectief gedrag optreedt.

Naast mooie filmpjes van verschillende soorten collectief gedrag, leverden de simulaties ook een hoop data op. Een van de eigenschappen waar we naar gekeken hebben, is het vermogen van het collectief om de omgeving te verkennen. Door samen te komen in een groep is het collectief, en dus het individu in het collectief tot 1000 keer sneller in het verkennen van de omgeving ten opzichte van een enkeling.

In hoofdstuk 2 komen we tot de conclusie dat collectief gedrag met relatief simpele regels tot stand kan komen, en dat een groep zijn gedrag drastisch kan veranderen met slechts een kleine verandering in het gedrag van iedere individu. aanzienlijke voordelen met zich mee kan brengen. Er is echter ook een risico aan het vormen van groepen. Een voorbeeld waar je dit tegenkomt is de snelweg. Als er teveel auto's op de weg komen stropt het verkeer juist. Dit fenomeen wordt in het Engels een traffic jam' genoemd. Het woord jamming' is ook een begrip in de natuurkunde, waar het ongeveer hetzelfde betekent. Jamming is van toepassing op systemen die vaak uit vele kleine korrels bestaan. Een systeem van kleine deeltjes kan eigenschappen van vloeistoffen hebben, bijvoorbeeld het zand dat stroomt in een zandloper, een lawine, zout dat uit een zoutvaatje stroomt, of stromend verkeer. Onder andere omstandigheden kan het zijn dat er juist geen stroming is. Denk bijvoorbeeld weer aan het zoutvaatje waarin het zout blijft zitten als je het zonder te schudden op de kop houdt. Zonder stroming laat het systeem zich beter karakteriseren als een vaste stof. De fase waarin geen stroming meer is noemen we, net als in het verkeer, jammed.

Er zit dus wel een risico aan het samen komen in een grote groep. Indien er te veel individuen in een te kleine groep samen worden gedrukt, wordt de groep, net als in de file, minder dynamisch. In natuurkundige systemen is het bekend dat onder andere de dichtheid een erg belangrijke factor is die bepaalt of er jamming optreedt of niet. Maar in biologische systemen is hier nog weinig over bekend. In hoofdstuk 3 laten we zien dat zelfs met een dichtheid die hoger is dan de dichtheid waarop natuurkundige systemen jammen, biologische systemen nog steeds kunnen stromen. We gaan ook dieper in op de vraag welke factoren belangrijk zijn om te voorkomen dat biologische systemen jammen. Een van de factoren die voor ons model naar voren kwam, is dat een perfecte samenwerking niet altijd het gunstigst is. Bijvoorbeeld: als iedereen in de groep in precies dezelfde richting loopt met precies dezelfde snelheid, dan zal je altijd dezelfde individuen als buren hebben. In de dynamische systemen die we in de natuur zien wisselen de buren juist vaak. De efficiëntste manier om dit in ons model voor elkaar te krijgen is door te stellen dat individuen wel ongeveer dezelfde richting in bewegen als hun buren, maar niet in

precies dezelfde richting. Hierdoor duwen de individuen tegen elkaar aan en zijn ze in staat elkaar aan de kant te duwen en van positie te veranderen.

Tot aan hoofdstuk 4 hebben we de individuen benaderd als cirkels. De voornaamste redenen daarvoor zijn dat een cirkel een van de meest algemene vormen is en dat berekeningen in ons model makkelijker zijn dan voor andere vormen. In hoofdstuk 4 gaan we een stap verder en kijken we naar individuen die ellipsvormig zijn. Voor bacteriën bijvoorbeeld, zijn ellipsen een betere benadering van de vorm dan een cirkel. Ellipsen botsen op een andere manier met elkaar dan cirkels. Als twee cirkels botsen gaan ze na de botsing ieder de tegenovergestelde kant op. Denk bijvoorbeeld aan twee biljartballen die met elkaar botsen. Ellipsen zullen in het algemeen ook draaien door een botsing. Zulke botsingen zorgen er dus voor dat ellipsen dezelfde richting op gaan staan. In het model voor cirkelvormige individuen in hoofdstuk 2 hadden we een regel nodig voor collectief gedrag die stelde dat alle individuen dezelfde richting in moesten bewegen. Dan rijst natuurlijk de vraag: zorgen botsingen tussen ellipsvormige individuen ervoor dat individuen ze zich naar elkaar richten, en kan dit collectief gedrag opleveren?

In hoofdstuk 5 beschrijven we een poging om systemen van bewegende individuen op een zelfde manier te karakteriseren als natuurkundige systemen die bestaan uit kleine deeltjes. Door op verschillende manieren krachten uit te oefenen op het systeem kunnen we een aantal eigenschappen meten. Deze eigenschappen kwantificeren onder welke omstandigheden het systeem zich gedraagt als vloeistof of als vaste stof. Een iets lagere dichtheid of een hogere temperatuur kan ervoor zorgen dat de deeltjes kunnen stromen, terwijl er daarvoor geen spontane stroming mogelijk was. Hoewel de technieken die daarvoor ontwikkeld zijn voor natuurkundige systemen succesvol zijn, werken deze niet voor ons model van een biologisch systeem. We laten verschillende methodes zien om toch deze eigenschappen te meten. Uiteindelijk is de conclusie dat intrinsieke verschillen tussen natuurkundige en biologische systemen het onmogelijk maken om biologische systemen op dezelfde manier te karakteriseren.

Het laatste hoofdstuk, hoofdstuk 6, staat enigszins los van de voorgaande hoofdstukken. Hier doen we onderzoek naar de ontwikkeling van insecteneitjes; in het bijzonder de eitjes van fruitvliegjes en rode kevers. De ontwikkeling van deze eitjes is een interessant proces, waarbij cellen op de buitenkant van de eitjes groeien en delen. Uit experimenten is gebleken dat deze cellen na een aantal celdelingen volgens een wiskundig patroon over het ei verdeeld zijn. Het patroon suggereert dat de cellen zich over het eitje verdelen door tegen elkaar aanduwen. We modelleren deze duwkracht met dezelfde formule als de duwkracht tussen individuen zoals beschreven in hoofdstuk 2. Onze theorie is dat het patroon dat de cellen maken wordt veroorzaakt door een simpele duwkracht tussen cellen. Deze theorie hebben we getest door simulaties te doen en deze te vergelijken met de resultaten van experimenten die door Tanya in onze groep zijn uitgevoerd. Al onze resultaten wijzen inderdaad uit dat simpele wisselwerkingen zoals duw- en trekkrachten tussen cellen de drijfveer zijn achter de ontwikkeling van insectenembryo's.

Curriculum Vitæ

Ruben van Drongelen

20-01-1989 Born in Vlissingen, Nederland.

2001–2007 Secondary school: Scheldemond College, Vlissingen

2007–2008 Propaedeutics Mathematics, *Leiden University*

2007–2010 B. Sc. Physics, *Leiden University*
Thesis: On measuring the sizes of massive galaxies at high redshift
Supervisor: Prof. dr. T. H. Oosterkamp

2007–2010 B. Sc. Astronomy, *Leiden University*
Thesis: On measuring the sizes of massive galaxies at high redshift
Supervisor: Supervisor: Prof. dr. M. Franx

2010–2012 M. Sc. Theoretical Physics, *Leiden University*
Thesis: The formation of Dark Matter Halos in the Excursion Set
Supervisor: dr. K. E. Schalm

2013 PhD in theoretical biophysics at the Department of Bionanoscience, *Delft University of Technology*
Thesis: Collective dynamics and jamming in biological systems
Promotor: Prof. dr. A. M. Dogterom
Co-promotor: dr. T. Idema

List of Publications

4. **R. van Drongelen**, T. Vazquez-Faci, T. Huijben, M. van der Zee, and T. Idema, Mechanics of epithelial tissue formation, J. Theor. Biol. **454**, 182-189 (2018).

3. **R. van Drongelen** and T. Idema, Dynamics beyond the jamming density - The unjamming of self-propelled particles, arXiv:1611.09125 (2016).

2. **R. van Drongelen** and T. Idema, Collective dynamics and motility of soft elliptical particles, Traffic and Granular Flow '15. Springer, Cham (2016).

1. **R. van Drongelen**, A. Pal, C. P. Goodrich, and T. Idema Collective dynamics of soft active particles, Phys. Rev. E **91**, 032706 (2015).